EPFL

A tunable femtosecond fiber laser source for multiphoton emission microscopy

Pierre-Marc Jean Marie DANSETTE

■ École
polytechnique
fédérale
de Lausanne

2021

A mon amour Zivile,
A mes parents Jean-Marc et Marie-Martine
A ma sœur Carole
A tous mes amis et toute ma famille

Acknowledgements

Foremost, I am very grateful for the opportunity I had to take part in this European training network "the future of biomedical imaging" and to have done my PhD in both one of the leading manufacturers of ultrashort lasers, Ekspla and the Laboratory for Fundamental Biophotonics at EPFL. I feel like getting to experience both the academic and industrial point of view has deeply enhanced my experience. The many meetings of the training network allowed me to share my research, and to follow the progress of other participants. It was also a very friendly and motivating group, which I was always looking forward to meeting with, and I wish to extend my thanks to all my co-researchers, Benjamin Efunbajo, Rastko Pajkovic, Tahir Jamal, Jeremiahs Püls, Zak Ali, Antonia Longo, Parastoo Afshari, Fabian Placzek, Björn Ole-Meyer, Mikael Erkkilä, Roger Fonellà Navarro, Marco Lai, Maksim Eremchev and Igor Nahalka. It was a pleasure working with you all, and I hope we will all keep in contact in the future! I wish you all good luck for your own PhD defenses, though from what I have seen you should not need it. My deepest thanks also obviously go to the organizers of this training network, Peter Andersen, Dominik Marti and Wolfgang Drexler, who all did a fantastic job organizing this training network. More formally, I need to acknowledge the funding this project received from the European union. This project has received funding from the European Union's Horizon 2020 research and innovation program under the Marie Skłodowska-Curie grant No 721766.

Further, I wish to acknowledge all my colleagues at EKSPLA, in particular those I worked with the most regularly, Audrius Zaukevicius, Laurynas Veselis (who now works for Integrated Fiber Optics), Karolis Madeikis, Karolis Viskontas and Raimundas Burokas and without forgetting my supervisors, Andrejus Michailovas, Nerijus Rusteika (also working for Integrated Fiber Optics now) and Rokas Danilevičius, who gave me great advice and guidance. You all made me feel very welcome at Ekspla and more generally in Lithuania. Ekspla is a fantastic company with a great working environment and it has been my honor to do my PhD there, in the beautiful city of Vilnius.

While most of my time was spent in Lithuania, I also had the opportunity to spend some time at EPFL. In particular I worked closely with Maksim Eremchev, who also came for a while at Ekspla, and David Roesel. I consider them both good friends and tremendously enjoyed cooperating with them. Again, the whole team

at the laboratory for fundamental biophotonics made me feel very welcome. Obviously, all my thanks to my thesis supervisor Prof. Sylvie Roke for her management of this project on the EPFL side.

Finally, all my love and my gratitude for my family who was there with me for even more than the last four years of this PhD. My wife Živilė, who married me during this time, and for who I cannot find the words to express all my love here. She accompanied me and encouraged me for this whole time, and I hope for much, much more to come. She is the best wife a man could dream off, and I do not deserve her, but I will keep her anyway! My parents and my sister Carole, obviously, who are always with me. Mom, Dad, thanks for everything and all my love. To you all I dedicate this thesis.

Vilnius, December 28th 2020

Pierre-Marc Dansette

Abstract

Multi-photon microscopy is a developing imaging modality that provides markerless specificity for many organic molecules or structures and good penetration depth in tissues. Already, it has helped deepen our knowledge of lipid water interface, allowed to detect the microtubular structure of neurons or even image electric potential differences. Medically, second harmonic and two photon excitation fluorescence imaging can be used to detect cancerous tissues. Recently, it was shown that wide field multiphoton microscopy can lead to less photodamage than confocal microscopy and be more suitable for imaging dynamic processes. These advances have been made possible by the development of ultrashort laser sources. Multiphoton signal is highly sensitive to the intensity of the illumination, and ultrashort laser pulses can reach extremely high peak power (MW or GW), while the average power, and thus thermal damage, remain low (a few W). Ideally, the laser source for a multiphoton microscope should be as short as possible to better take advantage of this effect. Conversely, the ideal light source is also tunable in wavelength, so that different fluorescence excitation spectra can be probed and to improve penetration in tissues. Wide field multiphoton microscopy requires lower repetition rates than confocal microscopy (up to a few MHz compared to a few hundred MHz or more), but also higher pulse energy. The initial objective of this project was the creation of such a light source based on optical parametric amplification using a femtosecond fiber laser source. The desired output was pulses shorter than 50fs with tunability from 700 to 1000nm. In this thesis, we assembled such a light source and tested it on a two-photon microscope.

First, we implemented a new simulation tool for second order processes in bulk crystal. Second order processes include parametric amplification as well as second harmonic generation, which is also required before the parametric amplification itself. The simulation tool we designed provides great flexibility to test the effect of relevant parameters (geometry, thermal conditions and pulse properties). This tool became the basis of all further work.

Then, we analyzed the effect of two different parameters on the second harmonic generation process. We showed that chirping of the laser pulses prior to second harmonic generation can have a large impact when we attempt to maximize the conversion efficiency. This effect needs to be accounted for when designing a second harmonic generation setup. In further related research, we showed how a novel transverse parameter, a temperature gradient in the crystal, can be used to compensate for the pulse chirp, and even take advantage of it to either compress the second harmonic pulses or increase their bandwidth.

Finally, we designed a parametric amplifier adapted to our laser source. Each part of the parametric amplification setup was tested and optimized. The setup was then integrated to a wide field two-photon microscope. Using this parametric amplification light source, we imaged several samples by two-photon microscopy. Comparing this to images realized with the pre-existing light source showed the expected throughput increase.

Keywords: Multiphoton microscopy, second harmonic, two photon excitation fluorescence, optical parametric amplification, nonlinear crystals, femtosecond lasers.

Résumé

Les microscopies multi-photon sont une technologie qui s'est récemment développée et qui permet d'imager avec spécificité un certain nombre de molécules et de structures biologiques. Cette technologie a déjà conduit à des avancées dans le domaine des interfaces lipide-eau, permis d'imager la structure des microtubules dans les neurones et même des différences de potentiel électrique. Médicalement, des images combinant la microscopie par seconde harmonique et la microcopie par excitation à deux photons peuvent révéler la présence de cellules cancéreuses dans des biopsies. Récemment, la microscopie multi-photon à large champ d'illumination s'est avérée bénéfique en termes de photo-dommage, et elle est aussi mieux adaptée à l'observation de phénomènes dynamiques. Ces résultats ont été rendus possibles par les avancées en matière de sources laser à durées ultra courtes. Le signal d'un microscope multi-photon est très sensible à l'intensité de l'illumination, et des lasers femto-seconde peuvent fournir des pics de puissance très élevés (MW ou GW) tout en maintenant une puissance moyenne faible (de quelques W), et évitent donc de bruler les échantillons. La source laser idéale pour un microscope multi-photon devrait avoir des impulsions aussi courtes que possible pour profiter au mieux de cet effet. En même temps, le laser devrait être modulable en longueur d'onde pour pouvoir exciter différents fluorophores efficacement, et optimiser la pénétration dans les tissus. En configuration grand champ, le taux de répétition des impulsions lasers peut être nettement moindre qu'en géométrie confocale (passant de quelques centaines de MHz à quelques MHz maximum), mais l'énergie par impulsion est aussi plus importante. L'objectif initial de ce projet était la création d'une telle source laser par amplification paramétrique optique, le but étant de produire des impulsions de moins de 50fs avec une longueur d'onde centrale pouvant varier de 700 à 1000nm. Au cours de cette thèse, nous avons assemblé et testé cette source laser.

Initialement, nous avons implémenté un nouvel outil de simulation des processus d'interaction à deux photons dans les cristaux non linéaires. Ces processus incluent l'amplification paramétrique et la génération de seconde harmonique, qui est souvent une étape préalable lors de la fabrication d'un système tel que le nôtre. L'outil de simulation que nous avons créé nous laisse une grande flexibilité pour explorer l'effet des différents paramètres impliqués dans ces interactions

(géométrie, température, propriétés de la source laser), et a servi de base pour tous les résultats présentés subséquemment.

Ensuite, nous avons exploré de manière plus approfondie l'effet de deux paramètres sur la génération de seconde harmonique. Premièrement, nous avons démontré que si la source laser présentait un « chirp », même faible, avant la génération de seconde harmonique, cela peut avoir un effet très large sur le procédé quand nous essayons de maximiser l'efficacité de la conversion. Cet effet doit être pris en compte pour concevoir des systèmes de génération de seconde harmonique efficaces. Deuxièmement, nous avons poursuivi cette ligne de recherche en introduisant un nouveau paramètre d'optimisation, un gradient de température dans le cristal. Lors de la génération de seconde harmonique avec une source ayant un « chirp », ce gradient de température peut partiellement compenser les effets négatifs, et nous permet aussi soit de compresser la seconde harmonique, soit d'élargir son spectre.

Finalement, nous avons conçu et assemblé un système d'amplification paramétrique. Chaque étape du procédé a été testée et optimisée. Le système a ensuite été intégré à un microscope à deux photons avec un large champ d'illumination. Avec cette nouvelle source nous avons imagé différents échantillons et comparé le signal capturé par la caméra à celui obtenu avec la source laser précédente. L'amélioration du signal prédite par la théorie a bien été observée.

Mots-clefs : microscopie multi-photon, seconde harmonique, excitation fluorescente à deux photons, amplification paramétrique optique, cristaux non-linéaires, lasers femto-secondes.

Table of Contents

List of figures

Chapter 1:

Chapter 2:

Chapter 3:

Chapter 5:

List of tables

Chapter 1:
Introduction

1.1 MULTIPHOTON MICROSCOPY

1.1.1   Principle of nonlinear microscopy

Multi-Photon Excitation Microscopy (MPEM) is an imaging mode that became available with the advent of ultrashort laser sources, with the first nonlinear microscope reported in 1975 [1] (with a 200ns pulse duration Nd:YAG Laser). MPEM images are produced by nonlinear interaction of light within a medium. Because nonlinear phenomena require high intensity, ultrashort lasers which provide high peak power but low average power are required, and the field developed when mode-locked lasers became available [2]. It has led to advances in biology, chemistry, nanoelectronics and physics. MPEM often relies on second order interactions, on which this work concentrates, though third harmonic imaging is also common [3], [4]. Two categories of nonlinear phenomena can be exploited in two photon microscopy: first, the nonlinear frequency conversion processes, in which 3 different frequencies ν_1, ν_2 and ν_3 interact so that the energy is conserved:

$$\nu_3 = \nu_1 + \nu_2 \tag{1.1}$$

Such interactions are governed by the second order susceptibility tensor $\chi^{(2)}(\nu_3, \nu_1, \nu_2)$. It is possible to demonstrate that because of symmetry, the tensor elements of $\chi^{(2)}$ are zeros when the medium is isotropic [5]. Unless there is a break in central symmetry, $\chi^{(2)}$ processes cannot take place. When two different laser wavelengths are available, this can be used to perform sum frequency microscopy (SFG) [6]–[8] (with incoming (ν_1, ν_2) and collecting ν_3), but most common case is second harmonic generation, which is a degenerate situation in which $\nu_1 = \nu_2$. The mechanisms of SFG and SHG will be described further in section 1.3.

The second type of two photon interaction used to perform microscopy is two photon excitation fluorescence (TPEF). TPEF relies on two photon absorption of the incoming laser, which excites the fluorophore (figure 1-1). The electronic energy level of the fluorophore is then relaxed to a lower, but still excited energy level via vibrational processes. Only then a new photon is emitted.

Unlike SHG or SFG, there is a non-optical process involved and the energy of the emitted photon is less than the energy of the two absorbed photons.
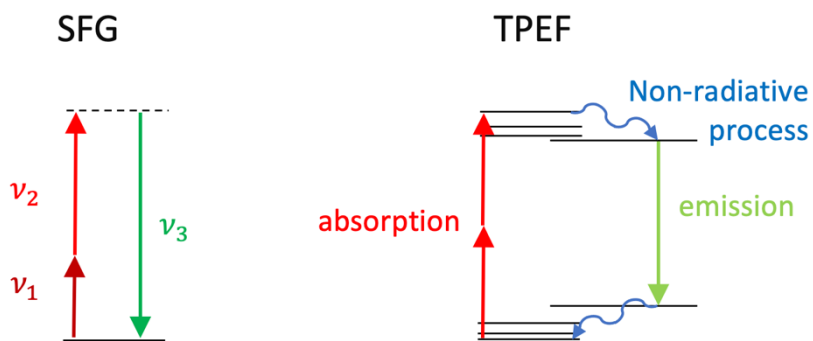
Figure 1-1 Schematic representation of the energy levels for sum frequency generation (left) and two photon excitation microscopy (right).

1.1.2   Second harmonic microscopy

Second order non-linear interactions can occur only in non-centrosymmetric media, so they will be sensitive to interface properties, as the symmetry is broken at the interface between two media, or to non-centrosymmetric molecules and structures. Thus, second harmonic generation (SHG) microscopy is used to observe membranes [9], [10], non-centrosymmetric organic molecules, such as collagen [11], [12], or structures such as microtubules in neurons [13]. The interaction of two photons with an electrostatic field will also result in a second harmonic photon being generated. This can be considered either as a modulation of the $\chi^{(2)}$ modulation by the electric potential or a third order $\chi^{(3)}$ interaction in which one of the frequencies is zero or nearly zero (neglectable compared to optical frequencies). Hence, second harmonic generation can also detect electric potential, for instance in neurons [14], [15].

One of the main advantages of SHG or SFG microscopy is that it is inherently specific to certain molecules. Thus, it doesn't require the use of photo-markers and complex treatment of samples. For instance second harmonic microscopy coupled with two photon autofluorescence is a promising alternative to hematoxylin and eosin (H&E) staining [16] for analysing tumour biopsies. H&E staining is a lengthy process (about 12h), while no particular sample preparation is required for SHG microscopy [17]. The specificity of SHG should be similar to H&E staining.

Convolutional neural networks can be used to classify the images [18], which can be difficult for medical professionals because they are not trained on this imaging modality. While markers are not necessary for many applications of multi-photon microscopy, nanoparticles such as $KNbO_3$ [19] that can serve as markers for SHG microscopy exist. Those can be used to observe some centrosymmetric media, or when the natural second harmonic signal is too weak.

Other than its specificity, SHG microscopy has several advantages when compare with linear microscopy. First, it is often performed with a near infrared (IR) laser source , allowing for deeper penetration in tissue [20]. The maximum resolution is defined by the second harmonic wavelength, not the laser source wavelength, so it is smaller. Second, the SHG process is quadratically dependent on intensity. This means that signal drops dramatically out of the beam focus. Finally, second harmonic generation is a coherent and instantaneous process, unlike fluorescence.

1.1.3   Two photon fluorescence microscopy

Two photon fluorescence is based on incoherent absorption of two photons, unlike SHG and SFG which are coherent processes. The relaxation of the fluorescent molecule to the ground state is in part realized by producing a photon at the fluorescent wavelength, the rest of the energy being dissipated through non radiative processes (figure 1-1). Two photon fluorescence is often used in conjunction with SHG imaging [17], [21]. The absorption of both photons needs to take place nearly simultaneously (around 0,1 fs [22]). Like SHG, two photon absorption quadratically depends on the intensity. Therefore, the signal out of focus also drops very fast leading to better lateral and axial resolution. The excitation wavelength of many fluorophores is in the UV or in the blue range [23], so multi-photon fluorescence can increase penetration depth and reduce photodamage. The two photon and one photon excitation spectra are not necessarily the same [22]. Another consideration is the non-radiative processes that accompany fluorescence and multi-photon fluorescence. This portion of the energy is transferred to the medium and can cause photobleaching. Because two-photon absorption is localised around the focus, photobleaching is reduced, though some higher order photobleaching mechanisms can also take place due to the high intensity [24].

Two-photon fluorescence gives access to some of the same imaging modalities as (linear) fluorescence microscopy. This includes fluorescence lifetime imaging microscopy [25]–[27] and stimulated emission depletion microscopy [28]–[30] which allows superresolution microscopy. Some naturally present molecules such as reduced nicotinamide adenine dinucleotide (NADH), which plays an important role for biochemical reactions in cells, exhibit fluorescence and can be detected by TPEF [31]. Two photon fluorescence already led to several advances in neurobiology for instance [32], [33]

1.1.4   Confocal or wide-field multiphoton microscopy

The idea of confocal microscopy was invented as early as 1957 [34] by Marvin Minsky, before the advent of the laser. In a modern confocal microscope, a laser beam is tightly focused on the sample by the objective of the microscope. Then the light coming back from the sample (due to scattering or fluorescence, in our case the second harmonic or TPEF signal) is imaged to a pinhole, before reaching a photodetector. The laser focus is scanned across the sample to acquire a full image. By contrast in wide field imaging, the whole sample is illuminated (or at least the section we want to image).

Initially MPEM experiments were conducted using confocal scanning microscopy [9], [11], [13], [14](beam diameter of about 500 nm), but recent works often use wide field illumination [35], [36], with beam diameters around $100 \ \mu m$. In wide field MPEM much lower repetition rates of a few hundred kHz are used, with pulse energies of 100nJ or more, compared to 100 MHz and less than 1 nJ for scanning microscopy. Yet a wide field approach can lead to two to three times higher throughputs [35], [37], while increased thermal diffusivity reduces the thermal damage and photobleaching [38]. It can also be better suited for dynamic studies as there is no need to scan the sample [39], [40]. Interferometric SHG allows to retrieve phase information [40]–[42], hence more information about the orientational organization of molecules. Good in depth resolution can be reached by implementing HiLo methods [37], [43]. The requirement for the source laser in wide field MPEM are of high pulse energies, short pulses and relatively low repetition rates.

1.1.5 Requirements for the laser source

The common limitation to all non-linear microscopy techniques is intensity. In order to observe significant non-linear conversion, high intensities are required. But damage to the sample limits the average intensity. Therefore, very short pulses in the femtosecond or picosecond range are ideally suited for this application. They can reach extremely high peak intensities, while if the pulse repetition rate is low enough, the average power of the laser can be low. The shorter the pulse is the more advantageous this can be. A second requirement for the laser source will be tunability. It is necessary for sum frequency or difference frequency interaction, and also if we want to probe any non-linear interaction at resonance. Biological tissues usually have a long transmission length in the near infrared, so tuning the laser to optimize penetration in the tissues can improve resolution.

1.2 ULTRASHORT LASERS

1.2.1 Early lasers

The first laser, or "light amplification by stimulated emission and radiation" was built in 1960 [44], though the principle of stimulated emission of radiation was proposed by Albert Einstein as early as 1916 [45]. In a laser medium, active ions are pumped to an excited state (using radiative or non-radiative processes). Often the pump is another laser, with the initial laser being a semi-conductor laser diode pumped electrically [46]. A photon at the correct wavelength to bridge the bandgap can cause stimulated emission, via which the ion relaxes to a lower state by emitting a new photon with the same phase, direction and wavelength (figure 1.2, right). The initial photons are provided by spontaneous emission. This means their direction and phase are random.
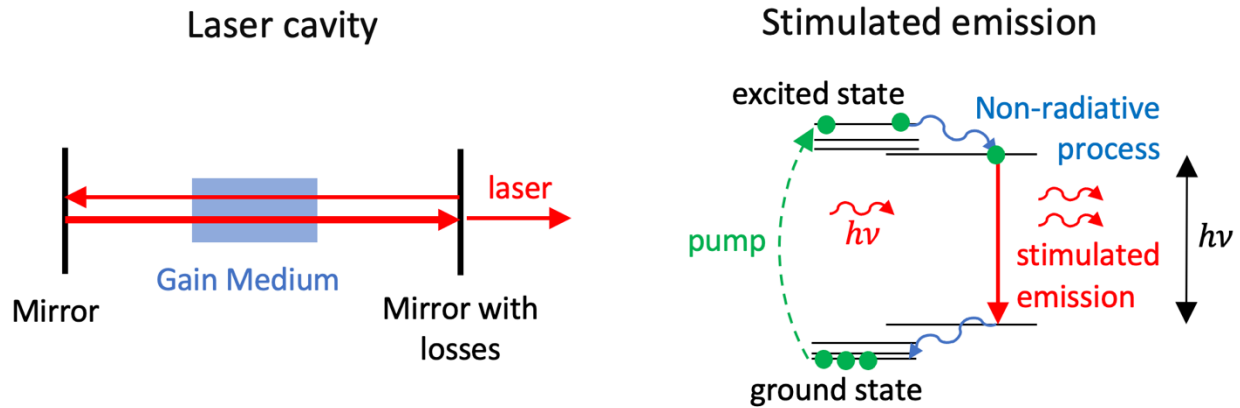
Figure 1-2 Simplified representation of a laser cavity and energy level representation of stimulated emission in the gain medium for a 4 levels laser.

The light is reflected back and forth in the gain medium by two mirrors (or fiber Bragg gratings for a fiber laser), with a portion of the light escaping on one side. This is the laser cavity (or more accurately resonator since it is open on the sides), out of which comes the laser beam. Even though spontaneously emitted photons have a random direction, only those aligned with the cavity will be significantly amplified by passing several times through the medium. For continuous wave operation there needs to be an equilibrium between the losses at the mirrors and the gain [47]. If the losses are higher than the gain, there can be no lasing. In order to produce pulses down to the nanosecond range, the losses of the cavity can be modulated, either passively or actively. This is called Q-switching. Passive Q-switching methods include the use of saturable absorber crystals [48], or self-focusing to modify the geometric configuration and thus the losses [49]. Q-switching can also be active, for instance using an acousto-optic [50] or electro-optic modulator [51].

1.2.2 Mode-locked lasers

Q-switching is insufficient for picosecond or femtosecond laser pulses, for which an additional condition is needed: mode-locking. The theory of mode locking was proposed in 1964 for masers [52], though the principle is the same for lasers. Here the parameters of the cavity are chosen so that an ultrashort pulse can remain constant after a round trip, with a pulse emitted for each round trip. Again, mode locking can be achieved actively using an acousto-optic [53] or electro-optic [54] modulator synchronized with a resonator round trip. Active mode locking can typically achieve picosecond pulses [55], [56]. In that case, a pulse can pass through the modulator just

when the losses are low at each round trip. Such a pulse will be favored because it has fewer losses and so gets amplified more. When the laser is operating in the steady state, the pulse will deplete the excited energy level and so saturate the gain, meaning there is a negative gain for other radiation (due to losses). Two competing effects will determine the pulse duration: A shortening of the pulse because the edges experience slightly higher losses (we can assume a sinusoidal function for the losses), and pulse broadening due to chromatic dispersion and the limited amplification bandwidth. The pulse broadening and shortening effects can be calculated as a function of duration, and the equilibrium of the two will be the pulse duration. This is the Kuizenga-Siegman theorem [57].
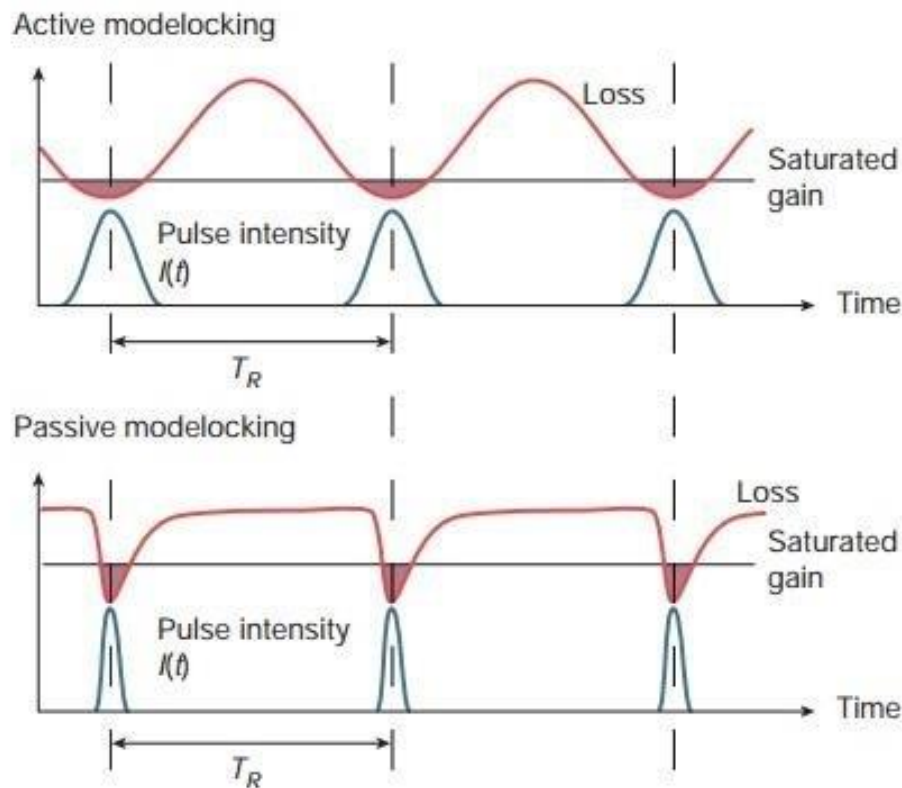
Figure 1-3: Losses (red) and pulse intensity (blue) for active (top) and passive mode locking. τ_R is the repetition rate, corresponding to a round trip through the resonator [58].

Passive mode-locking is typically achieved with saturable absorbers. If we assume a short pulse is already circulating, the losses will be small around the pulse peak because the absorber is saturated.

The leading wing of the pulse is significantly attenuated because it doesn't saturate the absorber. For the tailing wing, if the absorber had time to recover, it is also attenuated. This is the difference between fast saturable absorbers, with a recovery time smaller than the pulse duration and slow saturable absorbers, with a longer recovery time. Passive mode locking can achieve much shorter pulse durations [59], [60] because the loss modulation is much sharper than electronically achievable. It might seem surprising that slow saturable absorbers are suitable for mode locking, as there is a positive gain for the pulse tail (figure 1-3). Noise just after the pulse should thus be amplified, leading to instability. However, because the leading wing suffers losses and the tailing wing is amplified, the pulse gets delayed after each round trip [61]. The noise background is not delayed so it doesn't have much time where it gets amplified.

Here we assumed a pulse was already circulating, but the time it will take for such a pulse to form and thus for the mode-locking to self-start is another important question. Typically, slow saturable absorbers help with self-starting [62], though it can also be achieved with fast saturable absorbers[63].

The repetition rate of a mode locked laser is determined by the resonator length. To reach higher repetition rates, it is possible to have several pulses propagating in the resonator with a delay. This is called harmonic mode locking [64]. On the other end, a lower pulse repetition rate but higher pulse energy might be desirable. In that case, more round trips would allow the pulse to be amplified more before it exits the resonator. This can be done by intruding an optical switch, which will determine when the pulse can exit the resonator, thus controlling the number of passes through the gain medium. This scheme is called a regenerative amplifier [65].

Finally, a last important product of mode-locked lasers is the frequency comb [66]. Due to the properties of the Fourier transform, the spectrum of a periodic pulse train is not continuous but composed of equidistant discrete peaks. The lines inside this frequency comb are separated by the pulse repetition rate, and because mode-locked laser produce ultrashort pulses, the frequency comb is particularly broad. Such a spectrum is particularly useful in spectroscopy [67], [68], and the discovery of the frequency comb was rewarded by a Nobel prize in 2005. For frequency combs, one important property of mode locked lasers is the carrier envelope offset [69]. The carrier

envelope offset is the time between the pulse envelope peak and the closest electric field peak (figure 1-4). Carrier envelope phase needs to be compensated for few cycle pulses [70], [71] or for attosecond pulse generation [72], [73], as the amplitude of the electric field will strongly depend on the carrier envelope offset. Unless the carrier envelope offset is compensated, it typically changes by a fixed value for each round trip through the gain medium. For a frequency comb, where there is not necessarily compensation of the carrier envelope offset, that means that the lines are shifted by a constant frequency, corresponding to the carrier envelope offset change per round trip.
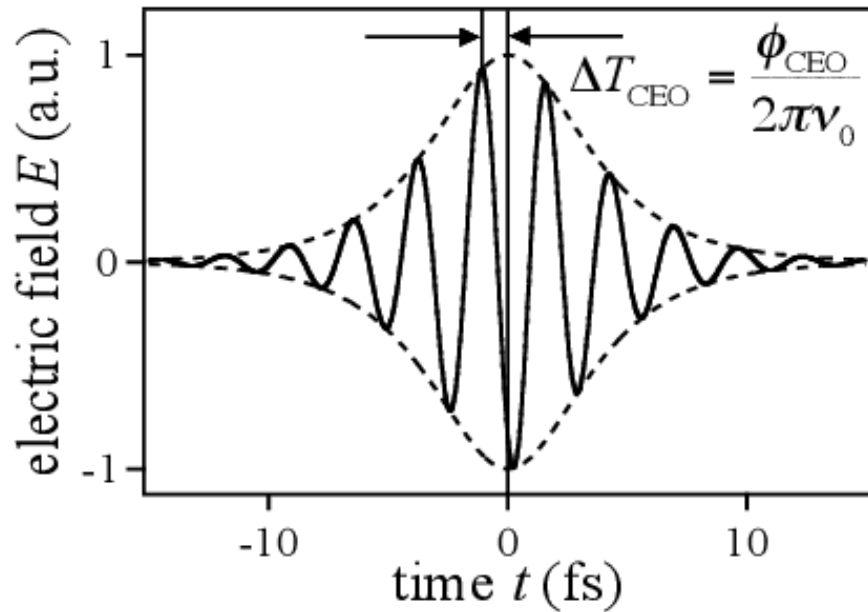
Figure 1-4: Electric field oscillations for a few cycle pulse, with the carrier envelope offset ΔT_{CEO} of the electric field relative to the pulse envelope. ν_0 is the optical frequency of the pulse and ϕ_{CEO} the carrier envelope phase [69].

Because ultrashort pulse can be generated with mode-locking, the high peak intensity in the gain medium can cause detrimental nonlinear effects and damage. This limits the effective peak power of the pulses. The solution to reach higher peak power is chirped pulse amplification.

1.2.3   Chirped pulse amplification

Chirped pulse amplification for optical pulses was proposed in 1985[74] by Donna Strickland and Gérard Mourou and rewarded by a Nobel prize in 2018. The idea is to stretch the pulse by using a

dispersive element (the stretcher, either a grating pair or an optical fiber) before it is amplified. The pulse is then recompressed after amplification, with a large beam diameter so that damage or nonlinear effects cannot occur. Because the pulse duration during amplification is much longer, the peak intensity inside the amplifier remains lower and so the pulse can be amplified much more before detrimental effects start happening. By using chirped pulse amplification it becomes possible to reach TW [75]–[77] or even PW [78], [79] peak powers. The amplification is typically performed by laser (stimulated emission), but the concept also applies to optical parametric amplification, which is discussed in the next section.

1.2.4   Fiber amplifiers

Fiber lasers gained momentum only after the development of the first erbium doped fibres in the late 1980's [80]. Femtosecond fibre lasers [81] are now a good alternative to solid state lasers as they are less sensitive to misalignment and generally cheaper. Erbium (Er) and ytterbium (Yb)[82] based fibre lasers are the most widely commercially available options, with central wavelength respectively around 1.55 and $1.05 \mu m$, though fibre lasers emitting further in the IR are also developed (around $2\ \mu m$ [83] or $3\ \mu m$ [84] for instance). A wider range of wavelength can be obtained by second harmonic generation and parametric amplification.

Fiber amplifiers are practical for chirped pulse amplification as, for a fiber with normal chromatic dispersion, the chirp will be generated by propagating in the fiber. Asymptotically, pulses in a fiber amplifier with chromatic dispersion and Kerr effect will tend towards a parabolic shape [85], [86]. For a sufficient propagation length and a large amplification factor, the peak power and duration of such pulses only depends on pulse energy. The upchirp, meaning the rise in instantaneous frequency, of such pulses is also nearly linear, making compression much easier.

1.2.5   Measuring ultrashort pulses

The characterization of ultrashort laser pulses is a complex problem. Measuring the spectrum is easy, but without knowing the spectral phase, the temporal profile of the pulse remains unknown. If we could measure the spectral phase, the electric field envelope temporal profile, and thus the

pulse instantaneous power, could be retrieved. Knowing the spectrum, the transform limited pulse can be calculated, meaning the pulse temporal profile if there was no spectral phase. This is also the minimum achievable pulse duration for a given spectrum. Photodetectors are not suitable for measuring ultrashort pulses, because rise time is typically in the nanosecond range. Ideally the pulse could be characterized with a second well known shorter pulse (by cross correlation for instance), but one is rarely available

The easiest method to find information on the pulse temporal behavior is autocorrelation [87]. Autocorrelation consists in separating the pulse in two with a semi-transparent mirror, then recombine the two pulses in a second order nonlinear crystal, so that the second harmonic is generated. For a short crystal, with low conversion efficiency, the second harmonic instantaneous power P_{SH} is proportional to the power of each of the two incoming pulses. If one of the pulses is delayed by a known time τ (using a delay stage), the second harmonic pulse energy E_{SH} is given by:

$$E_{SH}(\tau) = \int P_{SH}(t,\tau)dt \propto \int P_0(t)P_0(t+\tau)dt \qquad (1.2)$$

The autocorrelation is the dependence of the second harmonic signal (the second harmonic average power, meaning the pulse energy multiplied by the pulse repetition rate) on the delay τ. For a Gaussian pulse, it is possible to demonstrate that the full width at half maximum (FWHM) of the autocorrelation τ_{AC} is related to the FWHM of the pulse τ_0 by:

$$\tau_{AC} = \sqrt{2}\,\tau_0 \qquad (1.3)$$

This assumption is often used to estimate the pulse duration. However, there is no relationship between the autocorrelation and the pulse duration in the general case. Another property of the autocorrelation is that it is independent of the sign of the time, meaning two pulses that are symmetric in time will have the same autocorrelation. This can be remedied by third order autocorrelation (meaning autocorrelation using third harmonic generation [88], but the optical scheme is more complex and typically this requires higher peak intensity. In the case of a collinear

autocorrelator, there will also be interference in the autocorrelation trace. With interferometric autocorrelation the pulse duration and chirp can be calculated in a more general case [89].

Frequency resolved optical gating (FROG) [90] is a well-recognized method to retrieve the pulse profile and phase. The scheme is the same as for autocorrelation, but instead of simply measuring the second harmonic power, the spectrum of the second harmonic is acquired for each delay. This is enough information to completely reconstruct the electric field envelope.

Alternatively, the pulse can be reconstructed with a dispersion scan (Dscan)[91]. In that case the laser beam goes through a transparent material with variable and controllable thickness, before being frequency doubled in a second order nonlinear crystal. The spectrum of the second harmonic is acquired for a range of material thickness. The dispersive properties of the material are known, and so it is possible to retrieve the pulse profile and phase from the dispersion scan measurement. Typically, convergence of the algorithm is much faster than with FROG, and the optical scheme is simpler as there is no need for beam splitting or delay stages. The effect of material dispersion increases for shorter pulses. Thus, this technique is well adapted for sub 50fs pulses, but for longer pulses the thickness necessary to have a significative effect of dispersion becomes a limiting factor. For such short pulses, a third characterization technique, called spectral phase interferometry for direct electric field reconstruction (SPIDER [92]) is also quite suitable. It relies on combining interferometrically two copies of the incoming pulse separated by a delay with a third stretched (by some dispersive material) copy and acquiring the spectrum. The interferometric modulation of the spectrum can be used to retrieve the spectral phase of the pulse. The advantage is the simplicity of the algorithm, but the optical scheme is more complex than for dispersion scan or FROG, and since the interferometric fringes need to be accurately resolved, the spectral resolution is a limiting factor for narrow bandwidth pulses (ie. for longer pulses).

1.3 SECOND ORDER NONLINEAR CRYSTALS

1.3.1   Tunable laser source

Optical parametrical generation (OPG) is the process of using a strong laser beam, called the pump, to amplify a weak signal using difference frequency generation. This method is used to make a laser tunable in wavelength. Indeed, laser amplifiers typically have a very small tunability range dependent on the material properties. For very high repetition rates (100 MHz) the crystal is enclosed in a cavity, the parametrical gain is higher than optical losses so that oscillations can take place, exactly like an ordinary laser. This is called an optical parametrical oscillator (OPO) [93], [94]. For lower repetition rates (up to a few MHz) there is no cavity, and the system is simply called an optical parametrical amplifier (OPA) [95]. The pump beam in an OPA needs to have a much higher intensity, but the final energy of the signal pulses is also much higher than for OPO. It also has the advantage of not requiring a cavity, which makes it much less costly. In both cases along with the amplified signal a third beam, called idler, is generated so that:

$$\omega_p = \omega_s + \omega_i \tag{1.4}$$

Where ω_p, ω_s and ω_i are the angular frequencies of pump, signal and idler respectively. This relation is the conservation of energy. The idler will be generated along with the amplified signal and can be used for tunability on a second wavelength range. If the wavelength to amplify is shorter than the source laser wavelength, you will need a shorter wavelength for the pump in the OPA. This can be achieved using the second harmonic of the source laser for instance. More complex tunable lasers also exist. It is common to use several stages of parametrical amplification to improve the conversion efficiency [96]–[99]. Furthermore SFG [100] or difference frequency generation (DFG) [101] can be used to reach wider wavelength ranges. OPA is just a specific DFG setup where the signal is weak. The physics of SHG and SFG are the same as for OPA, the only thing changing being which wavelength are present at the front end of the crystal.

Parametrical amplification can be performed on quantum noise, amplifying the small quantum fluctuations at the wavelength selected by the phasematching conditions. While this method is

used to build tunable laser [102], it results in relatively poor stability, and the initial signal is so weak that several stages of amplification are often required. Therefore, supercontinuum generation (SCG) [103] is often preferred as a source of a weak signal to amplify. SCG results when the laser intensity in a medium is sufficient to cause self-focusing and plasma generation. Several effects can then take place (including four waves mixing, Raman scattering and second order nonlinear interactions), resulting in an extremely broad spectrum. Supercontinuum generation will be treated more in depth in chapter 5.

OPA systems are not only a method to make an ultrashort laser source tunable, but also to generate even shorter pulses. The bandwidth of the output of an OPA is not determined by the pump bandwidth, but by the bandwidth of the seed and the crystal properties. Indeed, the output of an OPA is often much shorter than the pumping laser [95], [104]. The principle of chirped pulse amplification also applies to OPA, in which case it is called an optical parametric chirped pulse amplification (OPCPA) [105]–[107], so that higher intensities can be reached. Back conversion of the signal wavelength is often the limiting factor for OPCPA performance [108]. Novel approaches use materials with strong absorption at the idler wavelength to prevent back conversion. This is called quasi-parametric chirped pulse amplification (QPCPA) [109] and allows the use of longer crystals, increases the amplified bandwidth and can reach conversion efficiencies up to 40% [110].

A tunable femtosecond OPA is an ideal source for MPEM. The output signal should have a much shorter duration than the pump, so that nonlinear effects are more efficient (because of the high peak intensity) while photodamage should be limited, because it depends more on the average power (at least for thermal damage) which is low. The photodamage will also depend on the intensity, but not linearly [111].

1.3.2 Phasematching in nonlinear crystals

Second order optical interaction involve 3 different electric fields of respective pulsations ω_1, ω_2 and ω_3 such that:

$$\omega_3 = \omega_1 + \omega_2 \tag{1.5}$$

This is imposed by energy conservation. SHG is a degenerate case where ω_1 and ω_2 are the same. However, there is a second condition imposed by momentum conservation:

$$\Delta k = k_3 - k_2 - k_1 = 0 \tag{1.6}$$

Where k_i is the wave vector of wave i. This equation can be rewritten as:

$$n_3(\omega_3)\omega_3 = n_1(\omega_1)\omega_1 + n_2(\omega_2)\omega_2 \tag{1.7}$$

Where n_i is the refractive index of the material for wave i. This phasematching condition will not be verified in most materials as there is either normal or abnormal dispersion. In practice the conversion remains efficient as long as the product of the phase mismatch Δk by the crystal length L is small. This is why the phasematching condition matters less in multi-photon microscopy samples, where the sources of nonlinear interaction are small. Here the aim is to convert a significant portion of the laser beam (or beams) energy, meaning we usually need relatively long (typically a few mm) crystals.

1.3.2.1 Collinear phasematching in Birefringent materials

One solution is to use birefringent crystals at a well-chosen angle. The general case is that of a biaxial crystal. The optical index for any of the waves will depend on the polarization. They are entirely defined by the index along the three main axis of the crystal X, Y, Z. By convention $n_X < n_Y < n_Z$. The value of the index is given by the intersection of the electric displacement vector $\vec{D}$ with the index ellipsoid (Figure 1-5). The orientation of wave vector $\vec{k}$ is usually chosen in one of the optical planes (XZ plane in Figure 1-5). The intersection of the wave plane with the ellipsoid is an ellipse. The main axis of the ellipse corresponds to the ordinary and extraordinary polarizations, with respective refractive index n_o and n_e. When operating in one of the optical planes, the ordinary index is one of the main indexes of the crystal (here n_Y). The extraordinary index n_e depends on the angle, in this case the spherical coordinate ϕ (angel between $\vec{k}$ and $\vec{Z}$).
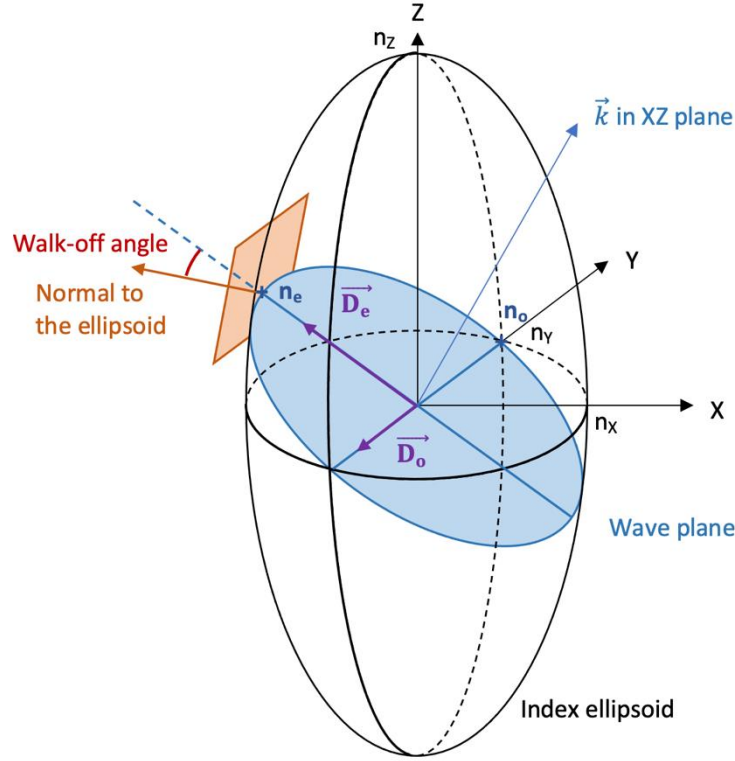
Figure 1-5: Refractive index ellipsoid for a birefringent crystal. The ordinary and extraordinary polarization directions, with the correspond electric displacement vectors $\overrightarrow{D_o}$ and $\overrightarrow{D_e}$ respectively, are shown for a given wave vector $\vec{k}$ in the XZ plane, along with the ordinary and extraordinary indexes (n_o and n_e respectively) and the walk-off angle.

For instance, we can use 3 collinear waves, with the extraordinary polarization for wave 3 and ordinary polarization for waves 1 and 2. The phase matching condition becomes:

$$n_e(\omega_3, \phi)\omega_3 = n_o(\omega_1)\omega_1 + n_o(\omega_2)\omega_2 \tag{1.8}$$

Thanks to the additional degree of freedom ϕ, equation 1.8 can have a solution for a large range of wavelengths. This case is called type 1 phase matching because only one of the 3 waves is in the extraordinary polarization. It is also possible to use type 2 phase matching, where two waves are in extraordinary polarization [95].

This kind of phasematching is called critical phasematching and relies on adjusting the angle of the crystal. However refractive indexes are also temperature dependent and it is possible to use

temperature to satisfy phasematching condition. This is called non-critical phasematching [112], [113]. In that case the $\vec{k}$ vector is aligned with one of the main axes, and so the ordinary and extraordinary polarizations are along the other two axes. The advantage of this method is to avoid walk-off. Figure 1-5 we can observe that for the extraordinary polarization there is an angle between the normal to the ellipsoid and the electric displacement $\overrightarrow{D_e}$. The normal to the ellipsoid is the direction of the electric field. Because of this, the same angle will be found between the wave vector $\vec{k}$ and the Poynting vector. If the crystal length is too long the effect of walk-off can be important.

We have so far discussed how to ensure the phasematching condition for a given set of frequencies (ω₁, ω₂, ω₃). However ultrashort pulses require a significant bandwidth, so ensuring phasematching for the central wavelength is not always enough. Because of energy conservation there is only two independent frequencies. In the case of sum frequency or difference frequency generation, one of the pulses is usually narrowband. For instance, we can assume wave 3 to be quasi monochromatic, which is often the case for parametric amplification schemes. Also, in most cases only two waves are present at the start of the crystal. For a frequency shift $d\omega$ of the first wave, the new set of frequencies becomes (ω₁ + dω, ω₂ - dω, ω₃) and the phase mismatch is:

$$\Delta k(d\omega) = k_3(\omega_3) - k_1(\omega_1 + d\omega) - k_2(\omega_2 - d\omega) \qquad (1.9)$$

With a first order approximation:

$$\Delta k(d\omega) \simeq \Delta k(0) - \frac{dk_1}{d\omega}d\omega + \frac{dk_2}{d\omega}d\omega = \Delta k(0) + \frac{d\omega}{c}\left(n_{g2} - n_{g1}\right) \qquad (1.10)$$

Where n_{g1} and n_{g2} are the group indexes for waves 1 and 2. Similar relationships can be found in case we assume wave 1 or 2 to be quasi monochromatic (typically for SFG schemes) or in the degenerate case of SHG (since wave 1 and 2 are the same there is no need for any additional assumptions). In practice the energy conversion is efficient if Δk L is smaller than π/2 [95], [114], with L the propagation length. This means we will be limited in terms of crystal length if we want conversion over a large bandwidth. We could imagine using both the temperature and the

orientation of the crystal to satisfy the phase matching condition as well as the proper group index relationship. However, except near some specific frequencies, it is not usually possible with practical temperature ranges [115].

1.3.2.2 Non-collinear phasematching

Alternatively, we can seek to cancel the first order term of Δk in dω. For this we need an additional degree of freedom. It can be created by using a non-collinear interaction:
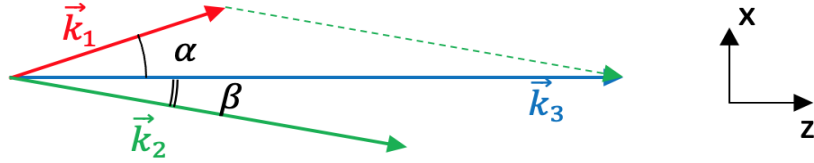
Figure 1-6: Wave vector geometry required for noncollinear phasematching

For a non-collinear geometry, the phase matching condition can be represented graphically (Figure 1-3). We can define a non-collinearity angle α between $\vec{k}_1$ and $\vec{k}_3$. The phasematching equation system will be:

$$\begin{cases} \Delta k_z = k_3 - \cos(\alpha)\,k_1 - \cos(\beta)\,k_2 = 0 \\ \quad \Delta k_x = \sin(\alpha)\,k_1 - \sin(\beta)\,k_2 = 0 \end{cases} \tag{1.11}$$

We can now look at what happens at $(\omega_1 + d\omega, \omega_2 - d\omega, \omega_3)$ in the first order in dω, :

$$\begin{cases} \Delta k_z(d\omega) = k_3 - \cos(\alpha)\left(k_1(\omega_1) + n_{g1}\dfrac{d\omega}{c}\right) - \cos(\beta)\left(k_2(\omega_2) - n_{g2}\dfrac{d\omega}{c}\right) \\ \quad \Delta k_x(d\omega) = \sin(\alpha)\left(k_1(\omega_1) + n_{g1}\dfrac{d\omega}{c}\right) + \sin(\beta)\left(k_2(\omega_2) - n_{g2}\dfrac{d\omega}{c}\right) \end{cases} \tag{1.12}$$

$$\begin{cases} \Delta k_z(d\omega) = \Delta k_z(0) + \dfrac{d\omega}{c}\big(\cos(\beta)\,n_{g2} - \cos(\alpha)\,n_{g1}\big) \\[2mm] \Delta k_x(d\omega) = \Delta k_x(0) + \dfrac{d\omega}{c}\big(\sin(\alpha)\,n_{g1} - \sin(\beta)\,n_{g2}\big) \end{cases} \tag{1.13}$$

We would like to cancel the first order terms described in equation system 1.13 as well as the zero-order term in equation system 1.11. The orientation of the crystal can be changed, as well as the non-collinearity angles. This is only three degree of freedom for 4 equations. However, in a typical DFG setup we input only wave 1 (called the signal for a DFG setup) and 3 (called the pump). This means the angle β is completely free and will naturally maximize energy conversion. The value of β that ensures perfect phase matching is different for any $d\omega$, so β will vary with the wavelength of wave 2 (called the idler). The angular dispersion of the idler will be given by:

$$\sin(\,\beta(d\omega)\,) = \sin(\alpha)\,\frac{k_1(\omega_1 + d\omega)}{k_2(\omega_2 - d\omega)} \tag{1.14}$$

The equations we have to satisfy using the angle α and the orientation of the crystal (or alternatively the temperature of the crystal [116]) are :

$$\begin{cases} k_3 - \cos(\alpha)\,k_1 - \cos\big(\beta(0)\big)\,k_2 = 0 \\[2mm] \cos\big(\beta(0)\big)\,n_{g2} = \cos(\alpha)\,n_{g1} \end{cases} \tag{1.15}$$

Non-collinear phasematching is useful for second order interactions with very broadband pulses, and frequently used for sub-30fs pulse durations [117]–[119]. This advantage comes at the cost of introducing non-collinearity, meaning the effective interaction length in the crystal is limited by the beam diameters. Assembling a non-collinear setup is also more complex. Furthermore, for SFG and DFG one of the beams will be angularly dispersed, making it harder to use.

1.3.2.3 Quasi-Phasematching

We have so far discussed how to satisfy the phasematching condition in a birefringent crystal. However, not all the crystals that have a large nonlinear susceptibility $\chi^{(2)}$ element display

birefringence, for instance gallium arsenide [120] is isotropic and can have a d_{eff} coefficient of 95 pm/V (for comparison beta barium borate, a birefringent crystal often used for type 1 critical phasematching has a nonlinear coefficient of ~2pm/V). Also in some cases the largest element of the $\chi^{(2)}$ is on the diagonal (for instance in lithium niobate the d_{eff} when all waves are polarized in the Z direction is 27pm/V, whereas it is limited to 4.35 pm/V for birefringent phase matching [121]). In those cases, it is preferable to use periodically poled crystals, for which the sign of the relevant $\chi^{(2)}$ element alternates with a period Λ. We choose Λ so that:

$$\Delta k \, \Lambda = \pi + 2m \, \pi$$

Where m is an integer. Because we switch the sign of the effective nonlinear coefficient d_{eff}, the phase is effectively switched by π. Thus, the interaction remains in average effective, albeit with a reduced factor of $\frac{2}{\pi(1+2m)}$. Usually, m=0 to maximize efficiency. Because higher d_{eff} values can be reached using quasi-phasematching, the process can still be more efficient than for birefringent phasematching. Importantly, quasi-phasematching can also be used with slightly non periodic poling of the crystal. The most popular application is chirped quasi-phasematching, where the period is "chirped", meaning Λ varies linearly in the propagation direction. We showed before that non-collinear phase matching in birefringent crystals adds a degree of freedom (the non-collinear angle), and so does chirping the poling period. This can affect the properties of the output and be used for compression in second harmonic generation for instance for instance [122], [123], or allow a larger bandwidth [124]. Chirped quasi-phasematching is particularly suitable for chirped pulse amplification [125], [126]. Sometimes a noncollinear geometry is also used with quasi-phasematching [127] instead of chirping the poling period.

The main inconvenient of quasi-phasematching is the requirement for specifically designed periodically poled crystals, which are often not available "off the shelve". This is especially true for aperiodic poling. Mostly, the periodic poling is achieved by ferro-electric domain engineering [128]–[130], though periodically poled gallium arsenide is produced by epitaxy [131].

1.4 THIS THESIS

In this thesis we develop a new tunable laser source for multiphoton emission microscopy. We study the theory of nonlinear energy conversion in birefringent crystals in order to optimize the laser parameters for this application. In the end, we successfully built an OPA source and integrated it to the microscope. This thesis is structured in the following way:

- Chapter 1 gives a brief overview of two photon microscopy, followed by an overview of ultrashort laser sources required for this application. The last section details the theory of second order nonlinear processes which will be used throughout this thesis.

- Chapter 2 describes the creation of a new simulation tool for second order nonlinear processes in crystal. This simulation tool covers several interacting optical effects in crystals and was thoroughly tested. The simulation tool provides the flexibility needed to model many different setups and is used extensively in the following chapters.

- Chapter 3 looks more specifically into the limitations of high efficiency second harmonic generation. The effect of spectral phase, in particular group delay dispersion, is analyzed with simulations, and confirmed in experiments.

- Chapter 4 looks into a novel parameter to control second harmonic generation in nonlinear crystals. After the negative effect of group delay dispersion was studied in the previous chapter, we now see how combining it with a linear temperature gradient in the propagation direction can improve conversion efficiency and provide control over the bandwidth and pulse duration of the second harmonic.

- Chapter 5 describes the assembling and testing of an optical parametric amplification setup as a source for a two-photon microscope. The design is guided by simulation. The final system compares favorably to an existing femtosecond laser source.

The list of published and submitted publications can be found at the end of this thesis.

Chapter 2: Numerical simulation of second order non-linear processes

Second order nonlinear crystals are often used to produce new wavelength from a source laser. This category of effects covers second harmonic generation, sum frequency generation and difference frequency generation. The output depends on the properties of both the laser source and the medium in which the second order energy conversion takes place. While there are simple equations for theoretical situations such as thin crystals and low depletion of the laser source, those simplifications are rarely valid in practical setups. Here, we seek to develop a simulation tool for second order light interaction in crystals. This simulation tool, called "Wavemixer", accounts for all significant effects that can affect the interaction such as linear propagation and self-phase modulation. The equations governing all relevant optical effects are discussed in this chapter. This tool is meant to let the experimentalist explore different parameters, such as crystal length, orientation, focusing conditions, temperature and many more. With this tool one can simulate all the commonly used setups for optical parametrical amplification, sum frequency generation and second harmonic generation, as well as test the effect of less well-known parameters. Accurate simulation results are important for designing highly efficient setups and provides a way to quickly test novel setups. Those results will be the basis of further work described in the next chapters.

The simulation tool described in this chapter was programmed and tested by Pierre-Marc Dansette, with some advice from Audrius Zaukevičius. Audrius Zaukevičius also provided results from a different simulation tool he created, which were used for comparison and testing.

2.1 INTRODUCTION

The high intensities that can be reached with ultra-short lasers make it possible to observe strong 2nd order non-linear optics phenomena in crystals. Those can be used to generate new wavelengths, with Second Harmonic Generation (SHG)[132]–[136] when a single wavelength is available, or with a second wavelength Difference Frequency Generation (DFG)[95], [137]–[140] and/or Sum frequency Generation (SFG) [141]–[143]. The fundamental equations governing all those second order non-linear optical phenomena are the same[95], [144], and the results will depend on the properties of the crystal. In order for the energy conversion to be efficient, phasematching, or in other words the conservation of momentum, is required. Real phasematching can be obtained by using an appropriate cut of a birefringent crystal [95], or alternatively quasi-phase matching [124], [145], [146] can be selected by carefully engineering periodically polarized non-linear crystals [130], [147]. Thus, simulation of second order non-linear processes is essential to the proper design of a tunable ultrashort laser system. There are existing software solutions to perform such simulations. However, they do not always offer sufficient flexibility [144], [148]. For instance, it is not possible to account for complex temperature profiles inside the crystal, to use real data on the laser pulse or beam as input.

Here, we developed a new simulation tool for second order non-linear optics in crystals. We accounted for all other relevant optical phenomena, such as dispersion, diffraction and cross and self-phase modulation. Several versions of the software were created, from a 1D version which accounts only for temporal effects and assumes plane wave, to a 3D version which can take any beam shape as an input (at the cost of calculation speed). This software will let us select appropriate crystals for our optical scheme, calculate the expected outputs and study the influence of different parameters on SHG or DFG.

2.2 OPTICAL EFFECTS IN NON-LINEAR CRYSTALS

2.2.1   Second order energy conversion

The main effect we are interested in is the nonlinear energy conversion between three waves at central frequencies (ω_1, ω_2, ω_3) such that:

$$\omega_1 + \omega_2 = \omega_3 \tag{2.1}$$

Let us consider the linearly polarized plane waves propagating in the z direction. We can describe the electric fields $\overrightarrow{E_i}$ for wave i by:

$$\overrightarrow{E_i} = Re\left(E_i\, e^{j(\omega_i t - k_i z)}\right)\overrightarrow{e_i} \tag{2.2}$$

Where E_i is the electric field complex envelope and k_i the corresponding wave vector. We can apply the same principle to the nonlinear polarization P_i^{nl} at ω_i :

$$\overrightarrow{P_i^{nl}} = Re\left(P_i^{nl}\, e^{j(\omega_i t - k_p z)}\right)\overrightarrow{e_i} \tag{2.3}$$

Where k_p is the wave vector of the nonlinear polarization. By using the slowly varying amplitude approximation we have the following equation relating E_i and P_i^{nl}:

$$\frac{dE_i}{dz} = -j\frac{\mu_0 c \omega_i}{2 n_i} P_i^{nl} e^{j(k_i - k_p)z} \tag{2.4}$$

Where μ_0 is the vacuum permittivity and n_i the refractive index of the crystal for ω_i (in the appropriate polarization). In the case of a second order interaction the nonlinear polarization P_3^{nl} at ω_3 is given by :

$$P_3^{nl} = \epsilon_0 \left(\overrightarrow{e_3}\chi^{(2)}(\omega_1 + \omega_2, \omega_1, \omega_2) : \overrightarrow{e_1}\,\overrightarrow{e_2}\right)E_1 E_2 \tag{2.5}$$

The wave vector $k_p = k_1 + k_2$. Similar equations can be written for P_1^{nl} and P_2^{nl}. $\chi^{(2)}$ is the second order susceptibility tensor. Because of symmetry rules [5] the tensor element is the same in all three equations. Further we will rather use the effective nonlinear optical coefficient d_{eff} :

$$d_{\text{eff}} = \frac{1}{2}\overrightarrow{e_3}\chi^{(2)}(\omega_3, \omega_1, \omega_2) : \overrightarrow{e_1}\,\overrightarrow{e_2} \tag{2.6}$$

The $\mathbf{d_{eff}}$ tensor elements are known at reference values of (ω_1, ω_2, ω_3) (for visibly transparent crystals it is often measure for SHG at 1064nm [149]–[151]) and the frequency dependence can be accounted by Miller's rule[5]:

$$d_{\text{eff }a,b,c}(\omega_1,\omega_2,\omega_3) = d_{\text{eff }a,b,c}^{ref} \frac{(n_a^2(\omega_1)-1)(n_b^2(\omega_2)-1)(n_c^2(\omega_3)-1)}{\left(n_a^2\left(\omega_1^{ref}\right)-1\right)\left(n_b^2\left(\omega_2^{ref}\right)-1\right)\left(n_c^2\left(\omega_3^{ref}\right)-1\right)} \qquad (2.7)$$

Where a,b,c are the main axis of the crystal, d_{eff}^{ref} the known tensor elements and ($\omega_1^{ref}, \omega_2^{ref}, \omega_3^{ref}$) the frequencies at which they were measured. All together this gives us a system of equations describing the second order interaction between the three electric field envelopes:

$$\begin{cases} \dfrac{dE_1}{dz} = -j\dfrac{\omega_1 d_{\text{eff}}}{n_1(\omega_1)c}E_2^* E_3 e^{-j\,\Delta k\,z} \\[2mm] \dfrac{dE_2}{dz} = -j\dfrac{\omega_2 d_{\text{eff}}}{n_2(\omega_2)c}E_1^* E_3 e^{-j\,\Delta k\,z} \\[2mm] \dfrac{dE_3}{dz} = -j\dfrac{\omega_3 d_{\text{eff}}}{n_3(\omega_3)c}E_1 E_2 e^{j\,\Delta k\,z} \end{cases} \qquad (2.8)$$

Where $\Delta k = k_3 - k_1 - k_2$ is the wave vector mismatch (sometimes also called phase mismatch though not technically accurate). DFG, SFG and SHG are all described by this system of equations. We have now demonstrated the importance of the phase matching condition Δk=0. If the length L of the crystal is such that $\Delta k\,L \gg 2\pi$ there will only be oscillation of the different waves' amplitudes, with no significative transfer of energy. In the case of quasi phase matching (Section 1.3.2.3) the d_{eff} coefficient changes sign periodically, meaning a π phase shift is introduced. This way the phase can remain between 0 and π and the energy transfer is efficient.

The optical intensity I_i is given by [152], [153]:

$$I_i = \frac{1}{2}c\epsilon_0 n_i |E_i|^2 \qquad (2.9)$$

Using this definition, the Manley-Rowe relationships on the variation of intensity of all three waves can be derived from the equation system [95]:

$$\frac{1}{\omega_1}\frac{dI_1}{dz} = \frac{1}{\omega_2}\frac{dI_2}{dz} = -\frac{1}{\omega_3}\frac{dI_3}{dz} \tag{2.10}$$

The different I_i are the intensities of the beam at frequencies ω_i. simply states photon conservation. For instance, in SFG, a photon at ω_1 and another at ω_2 turn into a new photon at ω_3.

Usually the phasematching condition is met, meaning $\Delta k = 0$. In the case when depletion of two of the waves can be neglected the equation system 2.8 can be simplified. For instance, for SFG (or SHG) if we can neglect depletion at ω_1 and ω_2 (meaning E_1 and E_2 are constant), since at the start there is no 3rd wave, E_3 linearly depends on z:

$$E_3(z) = -j\frac{\omega_3 d_{eff}}{n_3 c}E_1 E_2 z \tag{2.11}$$

By multiplying using equation we get the dependency of I_3 in z:

$$I_3(z) = \frac{2\omega_3^2 d_{eff}}{n_1 n_2 n_3 c^3 \epsilon_0}I_1 I_2 z^2 \tag{2.12}$$

The condition to neglect depletion is valid as long as the crystal length L verifies:

$$\frac{2\omega_3 d_{eff}}{n_1 n_2 n_3 c^3 \epsilon_0}I_1^0 I_2^0 L^2 \ll \frac{I_1^0}{\omega_1},\frac{I_2^0}{\omega_2} \tag{2.13}$$

Where I_i^0 is the initial intensity of wave i. Similarly, if we have DFG between wave 1 and 3 where depletion of both can be neglected, the intensity of wave 2 will quadratically increase with the propagation length in the crystal. However, for DFG it is more common to have a parametric

amplification setup were only wave 3 is strong and wave 1 is initially weak[95], [104], [154], [155]. If we can neglect the depletion of wave 3 (but not wave 1). Then from system 2.8 we get:

$$
\begin{cases}
\dfrac{d^2 E_1}{dz^2} = -j\dfrac{\omega_1 d_{\text{eff}}}{n_1 c}\dfrac{dE_2^*}{dz}E_3 e^{-j\,\Delta k\,z} - j\Delta k\dfrac{dE_1}{dz} \\
\qquad \dfrac{dE_2^*}{dz} = j\dfrac{\omega_2 d_{\text{eff}}}{n_2 c}E_1 E_3^* e^{j\,\Delta k\,z}
\end{cases}
\tag{2.14}
$$

So the second order differential on E_1 and E_2 are :

$$
\begin{cases}
\dfrac{d^2 E_1}{dz^2} = \dfrac{2\omega_1\omega_2 d_{\text{eff}}}{n_1 n_2 n_3 c^3 \epsilon_0}I_3\,E_1 - j\Delta k\dfrac{dE_1}{dz} \\
\dfrac{d^2 E_2}{dz^2} = \dfrac{2\omega_1\omega_2 d_{\text{eff}}}{n_1 n_2 n_3 c^3 \epsilon_0}I_3\,E_2 - j\Delta k\dfrac{dE_2}{dz}
\end{cases}
\tag{2.15}
$$

We can define:

$$
\Gamma = \frac{2\omega_1\omega_2 d_{\text{eff}}}{n_1 n_2 n_3 c^3 \epsilon_0}I_3
\tag{2.16}
$$

As long as $\sqrt{2}\,\Gamma > |\Delta k|$ the solution is in sinus hyperbolic and we have:

$$
I_1(z) = I_1^0\left(1 + \frac{\Gamma^2}{\Gamma^2 - \dfrac{\Delta k^2}{2}}\sinh^2\left(z\sqrt{\Gamma^2 - \dfrac{\Delta k^2}{2}}\right)\right)
\tag{2.17}
$$

$$
I_2(z) = I_1^0\frac{\omega_2}{\omega_1}\frac{\Gamma^2}{\Gamma^2 - \dfrac{\Delta k^2}{2}}\sinh^2\left(z\sqrt{\Gamma^2 - \dfrac{\Delta k^2}{2}}\right)
\tag{2.18}
$$

Otherwise, the solutions are sinusoid and the intensities of waves 1 and 2 will simply oscillate. The amplification is maximum when $\Delta k = 0$ and it depends exponentially on both the intensity of

the pump and the crystal length. In the case where $\Delta k = 0$ the condition that the pump depletion is neglectable is verified if:

$$\frac{1}{\omega_1}\sinh^2(\Gamma L) \ll \frac{I_3}{\omega_3} \tag{2.19}$$

Generally, we are interested in maximizing the conversion efficiency and the conditions to neglect depletion (both for SFG and DFG) are not met. There is no analytical solution without such assumptions and equation system 2.8 must be numerically solved. To find an analytical solution, we also neglected the contribution of linear phenomena as well as third order nonlinear effects such as self and cross phase modulation, which is not valid.

2.2.2   Linear optics phenomena

For a real laser beam we cannot use a plane wave approximation. For this section it will be easier to work in partial Fourier space (ω, k_x, k_y, z) where z is the propagation direction and k_x and k_y the components of the wave vector in x and y. The propagation equation will then be:

$$\frac{dE}{dz} = j\sqrt{k(\omega, k_x, k_y)^2 - k_x^2 - k_y^2}\,E \tag{2.20}$$

This is the propagation equation without any approximations. All linear effects are actually contained in this simple equation. For an isotropic crystal there would be no dependence of k on k_x and k_y. We will work in the general case of a Biaxial crystal and x is the direction of walk-off. If we are using ordinary polarization k is given by:

$$k(\omega) = \frac{n_o(\omega)\omega}{c} \tag{2.21}$$

Where n_o is the ordinary polarization index. This is true up to the second order in k_x and k_y. The ordinary polarization is aligned with one of the main axes of the crystal. Because of the symmetry

of the ellipsoid curve this means that there can be no odd order terms in k_x and k_y. It is often preferred to make a Taylor expansion of k on ω. We can write:

$$k(\omega) = k(\omega_0) + \frac{\partial k}{\partial \omega}(\omega - \omega_0) + \frac{1}{2}\frac{\partial^2 k}{\partial \omega^2}(\omega - \omega_0)^2 + \cdots \qquad (2.22)$$

Where ω_0 is the central frequency. This can be rewritten as:

$$k(\omega) = k(\omega_0) + \frac{1}{v_g}d\omega + \frac{D}{2}d\omega^2 + \cdots \qquad (2.23)$$

Where v_g is the group velocity for the ordinary polarization, D the group velocity dispersion in s²/m and dω=ω-ω₀. While this decomposition allows better understanding of the effect of different terms, it is not necessary. For most materials we have access to Sellmeier equations of the refractive index. Equation 2.23 is more convenient for discussing the role of dispersion, but equation 2.21 can be used in simulations because it requires no approximation on ω. The first order term will characterize the speed at which the pulse peak propagates in the crystal, while the second order term will cause the pulse to stretch. The group velocity and the group velocity dispersion can both be calculated easily by derivation of the refractive index from equations 2.21 and 2.22.

The case of the extraordinary polarization is slightly more complex as we have to account for walk-off. Because we are no longer operating along one of the main axes of the crystal, the refractive index will have a non-zero first order term in k_x. As we operate within one of the main planes of the crystal, symmetry will still be verified in the y direction and there can be no odd order terms.

$$k^2(\omega, k_x) = \left(\frac{n_e(\omega)\omega}{c}\right)^2 + A(\omega)k_x \qquad (2.24)$$

Where n_e is the extraordinary refractive index and A the first order term in ω. The zero-order term is the same as for the ordinary polarization, however n_e is not one of the main indexes of the crystal. For instance, let us assume we are operating in the XY main plane of the crystal. In this work the

main axis system of the crystal will be denoted with upper cases and the system relative to the beam propagation (where z is the propagation direction) with lower cases. In order to meet phase matching conditions, we need to operate at a given angle φ_0 in spherical coordinates (with $\theta=90°$ in this case because we are in the XY plane). The ordinary index will simply be the main refractive index in the Z direction n_Z and the extraordinary index will be:

$$n_e^2 = \frac{n_X^2\, n_Y^2}{n_Y^2 \sin^2 \phi_0 + n_X^2 \cos^2 \phi_0} \tag{2.25}$$

We can also calculate the first order term of k in k_x [156]:

$$A(\omega) = -n_e^4 \frac{\omega}{c} \frac{n_X n_Y \sin(2\phi_0)\left(n_X^2 - n_Y^2\right) \sqrt{\dfrac{n_X^2 n_Y^2}{n_e^2}}}{n_X^4 n_Y^4} \tag{2.26}$$

To simplify the equations the dependency of refractive indexes n_X and n_Y are not explicitly shown. Usually the walk-off is simply calculated at the central frequency, however there is no technical reason to neglect the dependency in ω as we usually have access to the Sellmeier equations for n_X, n_Y and n_Z. In practice that means there is also a small amount of angular dispersion of the extraordinary beam. The walk off angle ρ is given by:

$$\tan(\rho) = -A(\omega_0) \tag{2.27}$$

It would technically be possible to calculate the higher order terms in k_x and k_y [156], [157] though the effect should be quite small. Equations 2.20, 2.21 and 2.24 are sufficient to describe linear propagation. If we simply make a second order approximation in $d\omega$, k_x and k_y the linear propagation is given by:

$$\frac{dE}{dz} = -jk_x \tan(\rho)\, E + jd\omega \frac{1}{v_g} E - j\frac{k_x^2}{2k_0} E - j\frac{k_y^2}{2k_0} E + j\frac{D}{2} d\omega^2 E \tag{2.28}$$

We already discussed the terms in k_x, $d\omega$ and $d\omega^2$. The terms in k_x^2 and k_y^2 account for diffraction. Technically we should add a small corrective term to account for the second order components of k in k_x and k_y. We can see that Fourier space is particularly convenient to study linear propagation as this equation has a simple exponential solution in z. Importantly all linear terms only add spectral phase, and the spectrum is not modified by linear propagation. The decomposition of the propagation equation into its different contributor is more convenient than the more compact equation 2.20 for analyzing the role of different effects in the second order process.

The most obvious effect of group velocity will be different delays at different wavelength, meaning that it is not possible to keep the peak of all three pulses superposed after a certain length of crystal. If we consider how long two pulses will remain superposed, the effective crystal length is:

$$L_{eff} = \tau_{FWHM} \frac{c}{|\Delta n_g|}$$
(2.29)

Where τ_{FWHM} is the full width at half maximum duration of the shortest pulse and Δn_g the group index difference between the two wavelengths. In practice the effective length can also depend on the signs of the different group index differences. For instance, in a DFG setup with a strong pump wave (wave 3 in equation system 2.7), if wave 1 is slower than the pump and wave 2 is faster, DFG will generate new photon at the leading edge of wave 1 and the tailing edge of wave 2. This shifts the peak of both pulses, respectively forward and backward, and means the interaction can remain effective long after the pulses should have lost superposition[95]. Conversely, when wave 1 and 2 are both faster (or both slower) than the pump, this shift of the pulse peaks won't be as efficient and L_{eff} is a better approximation of the maximum usable crystal length.

Similarly to group velocity, walk-off means that the beams will loose spatial superposition. In type I phasematching (where only one wave is in the extraordinary polarization) this shift applies to a single wave, while in type II phasematching two beams will walk-off, but always in the same direction. This makes beneficial effects such as we discussed for group velocity unlikely. The effective crystal length to maintain spatial superposition will be:

$$L_{eff} = \frac{d}{\tan(\rho)}$$

(2.30)

Where d is the beam diameter (of the smallest beam if they are not the same).

Diffraction will cause an increase or reduction of the beam diameter. It is usually preferable to place the crystal at the beam waist to maximize the intensity and thus the efficiency of second order processes. As long as the crystal is much shorter than the Rayleigh length, the variations of beam diameter can be neglected. Similarly, the group velocity dispersion (GVD) will result in pulse stretching or compression. It is often preferred to operate with initially compressed pulses [136], [158] meaning that the initial spectral phase is flat (not ω dependent) or as close as possible. This is called a transform limited (TL) pulse. In that case the GVD will cause stretching (with positive or negative chirp depending if we are in normal or abnormal dispersion mode). If we don't want GVD to have a significative effect, we need:

$$L \ll \frac{\tau^2}{D}$$

(2.31)

Where τ is the pulse duration. In some cases, in particular for quasi phase-matching, the initial pulses are strongly chirped [126], [140], [146], [159] in which case the added dispersion from the material can usually be neglected.

We so far discussed temporal and spatial linear effects on the pulse. The effect on phase can also be significative, because they can introduce a phase shift between the three pulses in the 2nd order mixing process, resulting in lower conversion efficiency or even back-conversion.

2.2.3   Cross and self-phase modulation

Cross and self-phase modulation are third order nonlinear interactions. Unlike 4 waves mixing, no phasematching condition is required, thus this interaction will always happen. The third order nonlinear polarization for self-phase modulation is given by:

$$P_{nl}^{(3)} = 3\epsilon_0 \left(\vec{e} \boldsymbol{\chi}^{(3)}(\omega, -\omega, \omega, \omega) : \vec{e}\,\vec{e}\,\vec{e} \right)|E|^2 E \qquad (2.32)$$

Where E is the electric field envelope, $\vec{e}$ the unit vector of the electric field and $\boldsymbol{\chi}^{(3)}$ the third order nonlinear susceptibility. The factor 3 arises from the different permutations that would generate self-phase modulation. Similarly, when two different electric fields E and E' are present the cross-term polarization in ω is given by:

$$P_{nl}^{(3)} = 6\epsilon_0 \left(\vec{e} \boldsymbol{\chi}^{(3)}(\omega, -\omega', \omega', \omega) : \vec{e'}\,\vec{e'}\,\vec{e} \right)|E|^2 E \qquad (2.33)$$

We note the factor 6, double than for self-phase modulation (SPM), because of the additional possible permutations. Even using crystal symmetry to reduce the number of independent tensor elements it is uncommon for all $\boldsymbol{\chi}^{(3)}$ elements to be measured as there can be up to 81 independent elements. For isotropic crystals we have only 2 different values of $\boldsymbol{\chi}^{(3)}$ elements : $\chi_0^{(3)}$ when all polarizations are the same, and $\frac{1}{3}\chi_0^{(3)}$ when 2 waves have an orthogonal polarization to the other two (other tensor elements are zeros [160]). Unfortunately, we cannot use isotropic crystals because the $\boldsymbol{\chi}^{(2)}$ elements are all zeros (due to symmetry rules) and so they cannot be used for 2nd order interactions. However, the approximation of an isotropic crystal is often used because we lack information on the different values of the $\boldsymbol{\chi}^{(3)}$ elements. In that case, we will use a single nonlinear refractive index n_2 with:

$$n_2 = \frac{3}{4}\frac{\chi_0^{(3)}}{n} \qquad (2.34)$$

Therefore the effect of self-phase modulation is given by :

$$\frac{dE}{dz} = -j\frac{n_2\omega}{c}I\,E \qquad (2.35)$$

Where I is the intensity (see equation 2.9). As long as the intensity is low self-phase modulation is neglectable with typical n_2 values of a few $10^{-20}\,\text{m}^2\text{W}^{-1}$. However, with fs pulses the effect can be relevant even with a short crystal. Usually self-phase modulation in a crystal (or optical fibers) is characterized by the B integral [161]:

$$B_{int} = \frac{2\pi}{\lambda} \int_0^L n_2 I_{max}(z) dz \tag{2.36}$$

Where I_{max} is the peak of intensity in the beam plane or the center of the beam (for gaussian beams), L the length of the crystal and λ the central wavelength. If $B_{int} \ll \pi$ the effect can be neglected. Self-phase modulation, also called optical Kerr effect, will cause stretching (if the initial pulse is unchirped or up-chirped) or compression (for down-chirped initial pulses) of the pulse because introduction of a time dependent phase term. Furthermore, the spectrum will also be stretched (or compressed for initially down-chirped pulses) and can exhibit strong oscillations if B_{int} is large (a few π) [162], [163]. This effect is often used in fiber lasers to increase bandwidth [164]. The other well-known effect of self-phase modulation is beam distortion, and in particular self-focusing [165], [166] which can also occur for large value of B_{int}. The variation of the effective refractive index along the beam causes lensing, which can result in extremely tight focusing and damage to the material.

Self-steepening [167], [168] is also a known effect of SPM. The intensity dependence affects not only the effective refractive index, but also the effective group velocity. Usually this means an intensity dependent increase of the effective group index, meaning that the pulse peak is slowed down more than the rest of the pulse, so the tailing edge of the pulse steepens. This effect is particularly important for supercontinuum generation [169], [170], but can usually be neglected in $\chi^{(2)}$ interactions, except for few cycles pulses [171].

Along with SPM, cross-phase modulation will also occur between the different waves. The effect of the intensity I_2 of wave 2 on the electric field envelope E_1 of the first wave is given by:

$$\frac{dE_1}{dz} = -ja\frac{2n_2\omega}{c}I_2\,E_1 \tag{2.37}$$

Where a=1 when both electric fields have the same polarization, and a=1/3 when they have orthogonal polarization. This means that for 2 waves in the ordinary polarization (or in the extraordinary one), the effect of cross phase modulation is twice larger than self-phase modulation, and only 2/3 when the waves considered have different polarization. In a typical second order interaction setup, we have three different wavelengths, and need to consider the 3 terms of self-phase modulation and the 6 terms of cross-phase modulation. In this work we define the following B_{int} for cross phase modulation:

$$B_{int(2\to1)} = a\frac{4\pi}{\lambda_1}\int_0^L n_2\widetilde{I_2}(z)dz \tag{2.38}$$

With $\widetilde{I_2}(z) = I_2(x_0, y_0, t_0, z)$ and x_0, y_0, t_0 so that
$$I_2(x_0, y_0, t_0, z)I_1(x_0, y_0, t_0, z) = \max\left(I_2(x, y, t, z)I_1(x, y, t, z)\right)$$

In other words, we chose to account for the effect of wave 2 on wave 1 where they exhibit the strongest superposition. We made this choice because the effect will be the strongest at the peak of I_2, but if I_1 is small there the overall effect on wave 1 will be small. To our knowledge there is no standard definition of B_{int} for cross-phase modulation. This will give us a definition similar to the standard one for SPM when we have superposed gaussian beams and pulses, but also account for a delay or a spatial shift between the two waves.

Self and cross phase modulation are one of the limiting factors for second order nonlinear setups, because the efficiency is strongly intensity dependent, but they limit how tightly we can focus or how long the $\chi^{(2)}$ medium can be without beam distortion, spectrum oscillation or even self-focusing.

2.3 ALGORITHM

Based on the equations described in the previous section, I programmed an application called "Wavemixer" that can simulate any second order interactions in crystals, provided with the appropriate input data. This allows us to explore novel scheme before actually building them and to choose the best setups prior to experiments.

2.3.1   Dimensions

The "Wavemixer" application currently has 4 different versions called 1D, 2D, 2Dcyl (for 2D cylindrical) and 3D. Those names refer to the number of dimensions used in the simulation. They are used to model second order phenomena with increasing physical accuracy at the cost of processing time.

The simplest case we can simulate is that of 3 plane waves interacting. This means we only have to consider the dependence of the electric fields envelopes on time. The first version of "Wavemixer" is thus called 1D. Technically there could be a "0D" version for monochromatic plane waves, but due to the high intensities required for efficient second order processes, continuous wave lasers are not relevant. In practice there is also no (efficient) plane wave application of $\chi^{(2)}$ crystals, but the simulation should be relatively accurate for nearly flat top super Gaussian beams as long as the beam diameter is relatively large (so that there is no effect of diffraction). In the 1D version the complex electric fields envelopes are stored in arrays corresponding to a time grid with a regular step. The changes are calculated for regular dz steps along the propagation direction, until the total crystal length is reached.

The advantage of the 1D version is the speed of processing. The complexity will depend on the size of the time grid and the number of z steps, which is set as a power of 2 to optimize the processing speed of the Fourier transform operations. With the current version, running with 8GB 1.6GHz RAM it takes 3.5 s to perform a simulation with 16 384 time steps and 100 z steps. The approximation of plane waves is not usually valid so the results of the 1D application are often very inaccurate. In particular the conversion efficiency (For SFG, DFG or SHG) are often

overestimated. This version is still a good first step when we want to find a range of appropriate parameters for setup (such as crystal length, peak intensity,…). The estimates it produces on B_{int} should be relatively accurate. In the case of parametric amplification, we can observe whether there will be a significant depletion of the pump pulse or even back-conversion of energy from the signal to the pump. Temporal effects will be simulated so we can check the impact of group velocities, GVD as well as the initial pulse durations and chirp. Some setups use strongly chirped pulses, with pulse durations up to a few hundred ps but transform limited duration (the duration if the pulse was perfectly compressed) of a few tens or hundreds of femtoseconds [99], [172], [173]. To simulate this, we require small time steps so that we can fit the spectrum (the smaller the time step the larger the spectral window in Fourier space) as well as a large time window, meaning 100K or more steps. This is the typical case where it is better to perform all initial simulations with the 1D version and refine the results later with other versions.

The 2D version makes use of a single spatial dimension in the beam plane, usually along the walk-off direction, along with the time dimension. The electric fields are 2D matrices, with a corresponding regular time grid and regular space "x" grid. In the y direction, we assume we have a plane wave. The aim of this version is to simulate spatial effects such as walk-off and diffraction, while keeping computation times and memory requirements low. With this version, we can now simulate non-collinear setups, though the plane wave approximation for the second space dimension is not usually valid. Just like the 1D version, this is meant more for early simulations and finding out which parameters have a significant effect. Only for a noncollinear setup with large beams would the results be valid (in the collinear case the 1D version is faster). The estimated conversion efficiency is still usually inaccurate, as we assume constant intensity in y direction and second order processes are strongly intensity dependent.

For a typical simulation with 2048 time steps, 64 space step ("x" grid) and 100 z steps, it takes about 22s. If a large number of time steps is required, simulation can become much more time intensive.

The 2D cylindrical version makes use of cylindrical symmetry so that a more accurate simulation can be performed with a spatial "radius" grid and the time grid. In most practical cases the beams

have cylindrical symmetry. The only component of equation 2.27 that breaks cylindrical symmetry is walk-off. As long as the ratio of beam diameter to crystal length is much smaller than the walk-off, it can be neglected (this is often the case). Consequently, unlike the 1D and 2D versions the results of the 2Dcyl version should be very accurate as long as we can neglect walk-off. Unfortunately, it is also impossible to simulate a non-collinear interaction with this version. Unlike other versions, the radius grid is not regular, but instead form the roots of a 0 order Bessel function. This is because the Fourier transform no longer works with cylindrical coordinates. Instead we use a Hankel transform[174] and this choice of grid lets us perform the discrete Hankel transform algorithm [175], [176]. This version of the application combines both computing speed and accuracy as long as the conditions for cylindrical symmetry are met. In fact, for the same simulation conditions as the 2D version (2048 time steps, 64 radius steps and 100 z steps) the calculation takes only 7s.

Finally, we have the 3D version. In this version all electric fields are 3D matrices, with a corresponding time grid, and 2 space grids (in x and y) for the lateral dimensions. No approximation at all is required, but the counterpart is a higher requirement for computing time and memory. Any beam shape can be simulated, and all effects discussed in section 3.2 are accounted for. For a 1024 steps time grid, 64 steps x and y grids, and 100 z steps, the calculation time is 2mn and 20s. This is far from prohibitive but can become so as soon as the grid sizes increase.

The current 4 versions of Wavemixer are well suited for all types of simulation, from quick pre-calculations with the 1D and 2D versions, to fully realistic simulations with the 2D cylindrical and 3D versions.

2.3.2   Modified split step Fourier algorithm

The actual simulation is performed using a modified split step Fourier algorithm[144]. The idea of such algorithm is to separate the linear parts of an equation, which are calculated in Fourier space, from the nonlinear part which is performed with a shift of a half step in real space. In our case the

modification arises from the treatment of SPM and CPM. We first convert all electric fields in real space (x,y,t) (for the 3D version; in other version there is just less coordinates) to Fourier space using fast Fourier transforms. We then perform a propagation step over a half step dz/2

$$E\left(\omega, k_x, k_y, \frac{dz}{2}\right) = e^{-j\sqrt{k^2-k_x^2-k_y^2}\frac{dz}{2}}E\left(\omega, k_x, k_y, 0\right)e^{-\frac{\alpha dz}{2}} \tag{2.39}$$

The first coefficient is a phase shift, arising from equation 2.19. The coefficient α is the absorption coefficient (in m^{-1}) and in many crystals is neglectable. Afterwards, we perform an inverse Fourier transform to come back to real space (x,y,t) representations. We then account for the effect of phase modulation (self and cross) over a half step (using equations 2.35 and 2.37). We now have the real space representation of all electric fields after a half step of propagation. This is where we perform the first mixing step using the equation system 2.8. For this we employ a Runge-Kutta algorithm[177] applied to the equation system. This algorithm is used to perform derivation operations on a discrete step with 4th order in dz accuracy. Following the mixing step we alternate between full steps of linear propagation in Fourier space (equation 2.20) followed by the SPM and CPM steps in real space and mixing steps. After the final mixing step, we perform another half step of linear propagation and phase modulation.

It would be possible to perform the phase modulation step along with the mixing in the Runge-Kutta algorithm. But it would add complexity and the third order phase modulation is a small correction, not the main effect we want to study. Furthermore, we are already using an isotropic approximation for those effects even if it is not valid, because accurate measurements of all available $\chi^{(3)}$ terms are not available. Self-steepening will not be accounted for by this algorithm, but it is usually neglectable. Multi-photon absorption is also not accounted for, because it is usually weak except near the UV (also dependent on the bandgap of the material [178]) and accurate coefficients are hard to find.

2.3.3   Optimization

The current versions of Wavemixer have been optimized for computing speed as well as reducing unnecessary operations. When working with very large grids like in 3D, the number of operations to perform is very large. For instance, with a 1024 time step grid and 64x64 space grid, there are 4 million elements per matrix representing an electric field, with 3 electric fields. For the linear step we need to perform a Fourier transform (the fast Fourier transform algorithm has a O(ln(n)n) complexity where n is the number of elements[179]), add a phase shift to each element (the phase shift per step can be calculated once for each (ω, k_x, k_y) combination as long as the crystal properties don't change in the z direction) and perform an inverse Fourier transform. Then we need to shift the phase of each element for the phase modulation step. The mixing step requires 12 multiplications operations on each element because of the use of a Runge-Kutta algorithm (we can neglect addition operations). So, for a 100 z steps we have about 1600 complex multiplication per element, and 200 calls of the fast Fourier transform function.

The initial versions of Wavemixer made no use of parallel computing and each of the operation on elements of the E fields was performed with for loops. Early attempts to parallelize the "for" loop calculations in MATLAB resulted in only small improvements or even an increase in calculation time. Much better results were reached by using matrix products instead of for loops to perform elementwise operation, resulting on average in 10 times faster calculations. This is likely because the matrix products are already parallelized and optimized in most programming languages. The fast fourier transform operations are also already optimized for speed (and parallelized) in most programming languages. For the 2D cylindrical version of "Wavemixer" the Hankel transform is used instead of a Fourier transform for the radial coordinate. For a given number of radial steps this can be done by applying a square matrix to each array of the electric field (for each time step). The matrix needs to be calculated only once for the whole simulation. This means complexity is in n^2 where n is the number of radial steps. While this is worse asymptotically than the fast Fourier transform algorithm, the 2Dcyl version is often faster than the 2D version for radial grids of less than 128 steps.

The initial versions of "Wavemixer" would save the electric field after each mixing step, which allowed to plot the spectrum, intensity and other parameters at any position within the crystal. This is practical if we are not sure which crystal length is best suited for our application, as the

simulation can be performed on a long crystal and we can check where exactly adverse effects start to appear. Technically there is a small error because we are missing a half step of linear propagation and third order phase modulation, but this is a very small error. For the 3D version the memory requirements for this becomes too large, as we would have 3 matrices of 400 million elements with the grid given as an example earlier. The time to store this on hard storage would massively slow down the application. Thus, there is no saving after each step in the 3D version. Instead, after each step the conversion efficiency is calculated and its dependence with z can be plotted at the end of the simulations. For the 2D and 2Dcyl versions savings data at each step is optional and should be avoided when using large grids. In the 1D version the memory requirements are small even for large time grids, so electric fields are still saved at each z step.

2.3.4 Input parameters

The application is meant to simulate various second order nonlinear processes in crystals. The first step is to choose the crystal we will be working with (Figure 2.1, "material" tab), for instance LBO (Lithium Triborate) or BBO (Beta-Barium Borate) are commonly used for the near IR or visible range. A list of crystals is provided for which all the relevant data has been saved. Alternatively, it is possible to add new crystals, which can then easily be shared with anybody using the application. For each crystal we need the following data:

- Is it a Biaxial or Uniaxial crystal?
- The Sellmeier equation of the main optical indexes (2 for Uniaxial crystals and 3 for Biaxial ones)
- The temperature dependence of the optical indexes. If this is not available, the effect of temperature cannot be calculated, and it is not possible to simulate non-critical phase matching
- The effective nonlinear coefficient tensor D_{eff} (meaning $\chi^{(2)}/2$) in pm/V
- The nonlinear refractive index n_2. A single value is provided like for an isotropic crystal, even if this approximation is not valid. This will be used as a default value. If more precise data is available for a specific polarization and propagation direction, it can be entered manually later.
- References for the source of all this data

Figure 2-1: Initial selection options for the "Wavemixer" applications

Secondly, we need to select the interaction we are interested in (Figure 2.1, "type of mixing" tab). This will determine what information is needed to start the simulations. For instance, in a SHG setup, there is only one wavelength entering the crystal (degenerate case where $\omega_1 = \omega_2$ in part 2.2.1). In a parametric amplification scheme a strong pump beam (frequency ω_3 in part 2.2.1) and a weak signal beam (frequency ω_1 in part 2.2.1) are superposed in the crystal. Similarly, for SFG we need information on the waves at frequencies ω_1 and ω_2. There is also an option to have all three frequencies from the start of the crystal (with non-zero energy), though this is rarely the case in practical setups. Once we chose the interaction we are interested in, we need to choose the phasematching options (Figure 2-1, "phase matching" tab): Non-critical phasematching (collinear), critical phase matching (collinear) or non-collinear. Once this is done there is an option to calculate all phase matching conditions in the crystal where the d_{eff} coefficient is non-zero (Figure 2-1, "phasematching conditions" button), and then select the one we want to use.

Finally, we need to provide information about the beams and pulses for all wavelength present at the start of the crystal (Figure 2-2). This means central wavelength, bandwidth, group delay

dispersion, delay between pulses, beam diameters, distance between the center of each beam, distance from the crystal front to the beam waist… (section "data on the input waves" in figure 2-2). For lower dimensions versions of "Wavemixer" less information is required. The beams and pulses can be Gaussian or super-Gaussian. Alternatively, measured spectra or beam profiles can be imported as well as results from previous simulations, which is useful for setups with several stages of amplification for instance[96]–[99]. This is done via the "import" buttons under the inputs for the different waves. We also need to indicate the crystal length and its temperature (except for non-critical phase matching). The phasematching condition will be calculated automatically, but we can introduce angular or temperature shifts to check the sensitivity to these parameters. The grid sizes can be chosen automatically for the given parameters or manually adjusted.
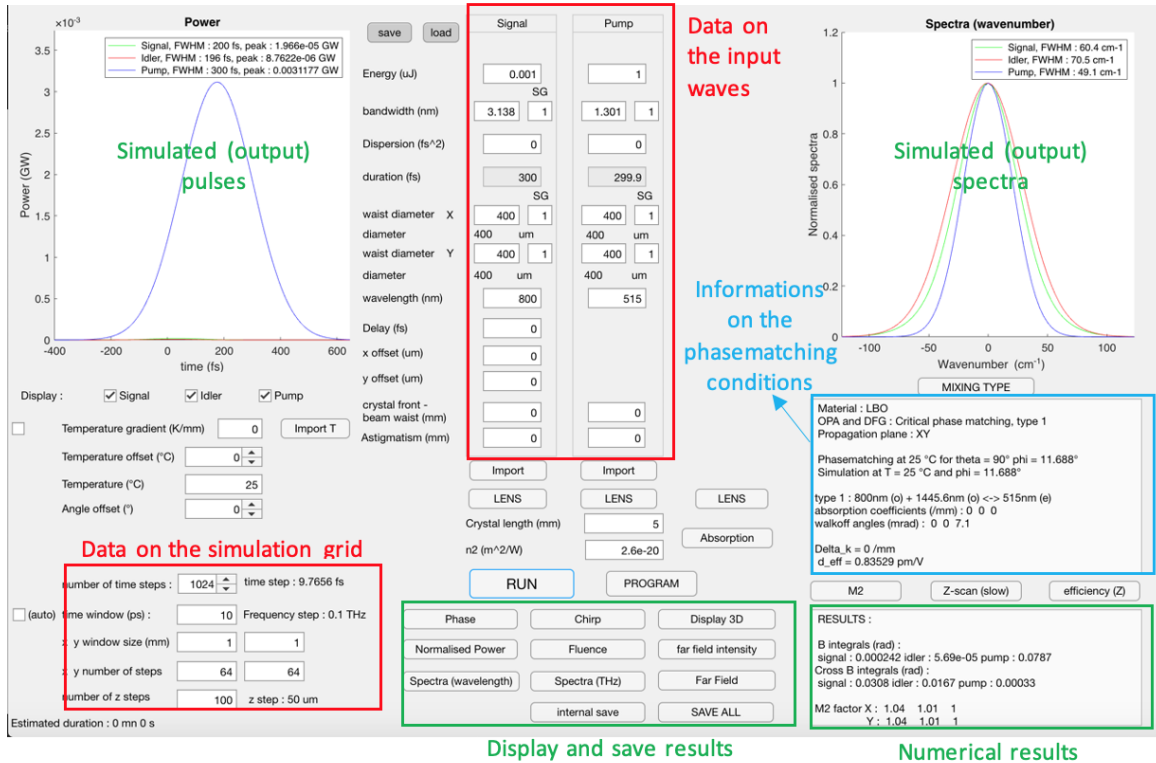
Figure 2-2: Main simulation screen for the "Wavemixer" applications. Here the simulation is for DFG, so 2 input waves are required. All data on the beams and pulses as well as the crystal size and temperature are provided here.

One of the advantages of "Wavemixer" over similar software [144], [148] is also the ability to model complex temperature profiles in the crystal. Temperature is one of the main parameters that

can strongly affect refractive indexes and therefore phasematching. Usually, the temperature of the crystal can be considered constant, but it can vary

2.3.5 Outputs

When the simulation ends, we have three electric fields matrices. From those intensity matrices can be calculated using equation 2.8. Integration over the space coordinates gives the power profile. The spectrum can be calculated by doing a Fourier transform of the electric fields along the time axis, and normalizing. The power and spectrum of all three waves is displayed on the main application screen (Figure 2.2). More graphs can also be plotted, for instance the beam profile ("Fluence" button), the phase, and so on. There is even an option to check the pulse properties at any point (x,y) in the beam (button "Display 3D"). By using "internal save" one of the complex electric field envelopes can be saved and used as an input in other simulations.

The final energy $\mathcal{E}_i$ (to differentiate from electric fields) for each of the three wavelength is calculated by integrating over time and space. We can then define the energy conversion efficiency η. For DFG the efficiency is:

$$\eta_{\text{DFG}} = \frac{\mathcal{E}_2 + (\mathcal{E}_1 - \mathcal{E}_1^0)}{\mathcal{E}_3^0} \tag{2.40}$$

Where $\mathcal{E}_i^0$ represents the initial energy of wave i. For a SFG or SHG setup the conversion efficiency is:

$$\eta_{\text{SFG}} = \frac{\mathcal{E}_3}{\mathcal{E}_2^0 + \mathcal{E}_1^0} \tag{2.41}$$

The conversion efficiency is one of the main results of a second order setup. However, the output pulse and beam are also important. In particular the beam focusability is characterized by the beam quality parameter M^2 [180]. For a Gaussian beam $M^2=1$, and it increases the further the beam is from a Gaussian. The beam quality will affect the relationship between the divergence angle and the beam waist by modifying the Rayleigh length z_R:

$$z_R = \frac{k w_0}{2M^2} \tag{2.42}$$

Where w_0 is the waist radius ($1/e^2$) and k the wave vector at the central wavelength. The evolution of the beam diameter in the propagation direction is simply given by:

$$w(z) = w_0 \sqrt{1 + \frac{z^2}{z_R^2}} \tag{2.43}$$

Equation 2.43 is how beam quality is measured by performing a Z-scan[180]. The beam diameter is measured around the focal point of a lens and fitting the curves gives M^2. The larger M^2, the larger the beam waist is for a given focal length. Thus, large M^2 can be a problem for microscopy. In our case we can calculate beam quality by using a mathematical formula[114]:

$$M^2 = \frac{w_k^2 w^2}{2} \left(1 - \frac{w^2 k^2}{w_k^2 R^2} \right) \tag{2.44}$$

Where w is the beam radius (at $1/e^2$), w_k the angular width in m^{-1} (meaning the radius in fourier space) and R the radius of curvature. The radius of curvature can be calculated from the phase of the electric field.

For each simulation the main results are summarized in the "numerical results" textbox (Figure 2.2). This includes the conversion efficiency, the peak intensity for each wave as well as the total energy, the B_{int} values for self and cross phase modulation, the M^2 values for each of the lateral space dimensions and the pulse duration.

2.3.6   Validation

In order to use the "Wavemixer" program we need to be absolutely sure that the results are valid. Validation of the results of "Wavemixer" was carried out in three different ways: Checking that

results match simple theoretical predictions in some specific cases, comparison with simulation results from SNLO [148] and another more limited simulation program created at EKSPLA. Finally, comparison to experiment.

In section 2.2 we reviewed all the physical effects that were to be implemented in the "Wavemixer" program. First, by choosing $n_2 = 0$ and canceling all linear propagation components, the implementation of the second order mixing was checked. When the crystal is short enough that depletion is neglectable, the results matched equation 2.12 for SFG and equations 2.17 and 2.18 for OPA. Then we performed DFG simulations where either the pump or signal initial was set to 0, also with $n_2 = 0$, meaning there was no mixing and only linear propagation. We observed the predicted diffraction (equation 2.43), the excepted shift of the beam center due to walk-off for the extraordinary polarization, the expected group velocity and the expected stretching of the pulse due to GVD. Finally, linear propagation terms were removed and n_2 set to non-zero (with still no mixing) to check that SPM was correctly implemented. The effects on self-focusing, the increase in bandwidth and the stretching of the pulse matched theory for the calculated B_{int} values. This means all the different components of the algorithm were checked to match theoretical results when an analytical solution exists.

The second step is comparison with other simulation tools. For this we can check the whole application for different values of the input parameters. Good match was observed in SFG, SHG and OPA simulation. A self-consistency test was also made: if we perform DFG simulation in a 2mm LBO crystal, save all the output results and import them as input in a "3 wave" simulation (simply meaning all 3 waves have non zero initial energy) in 2mm of LBO, we get the same results as if we directly propagated over 4mm. Some options are not available in other programs, such as a temperature profile varying with z in the crystal.

The crystal properties were checked by calculating the phasematching conditions at known wavelength and temperature, as well as checking the refractive indexes, group indexes and d_{eff} coefficient (typically for SHG from 1064nm and 800nm for the visible/ near infrared range). If the results match, it is unlikely that there is a mistake in the Sellmeier equations. This also proves that the calculation of phasematching conditions work as expected. The calculation of the beam quality

parameter M^2 was checked in 3 different ways. First, by checking that the value of M^2 for some specific beam shapes. For a gaussian beam M^2 should be 1 and for Hermite-Gaussian beams [181] M^2 should take integer values depending on the Hermite-Gaussian mode. Second, by plotting the beam diameter dependence on z when the beam is propagated in free space (simulating a Z-scan) and checking that the curve matches the theoretical one for the calculated M^2. Third, by studying the change of M^2 due to SPM when there is no mixing and checking the dependence of M^2 on B_{int} matches known results [182].

Finally, the last part of validation is experimental proof. Simulations were performed using experimental parameters for SH and two stages third harmonic generation setups (first a stage of SH and then SFG) with a good match. Overall simulation tends to overestimate the conversion efficiency by at least 10%. This is not surprising as the simulation assumes perfect condition (Gaussian beam, gaussian pulse, flat spectral phase…). It is possible to refine results by importing experimental data, in particular the pulse shape and phase obtained by Frequency Resolved Optical Gating (FROG)[183].Globally, the "Wavemixer" tool performs well and allows for choosing experimental parameters and relatively good estimation of the output parameters of a second order nonlinear setup.

2.4 CONCLUSION

In this work we developed a new simulation tool for second order non-linear interactions in crystals. We included all relevant linear and nonlinear effects in the algorithm. We use the optical properties of the chosen crystal to find the phase-matching condition and calculate the propagation of optical wavs in the crystal. The "Wavemixer" tool was successfully tested against theoretical results, other simulation tools and experiments. We can now use this tool to better design OPA, SHG or SFG setups and test novel approach, such as a temperature gradient in the crystal.

The simulation tool Wavemixer that was created and tested here was used in all the following chapters to test the effects of several parameters on second order nonlinear interactions and to choose appropriate crystals and beam diameters for experiments and prototype systems.

Chapter 3:
Peculiarities of Second Harmonic Generation with Chirped Femtosecond Pulses at High Conversion Efficiency

Second harmonic generation is often used to provide a pump for an optical parametrical amplification setup. In most such schemes the conversion efficiency from the fundamental to the second harmonic wavelength should be as high as possible, while maintaining good spatial properties of the second harmonic beam. Because second harmonic generation is highly sensitive to intensity, the second harmonic generation will often be performed on a well compressed pulse so that the pulse power is maximal. Here we study the effect of small amounts of group delay dispersion and higher order dispersion on the second harmonic generation process. We demonstrate that the conversion efficiency and beam quality are highly sensitive to small changes in the spectral phase, even if the fundamental pulse is not significantly stretched. Ideally, reducing the beam diameter and shortening the crystal length can reduce the sensitivity of second harmonic generation to group delay dispersion, but photodamage and Kerr effect limit the peak intensity. The sensitivity to group delay dispersion should be a practical concern when designing a high conversion efficiency second harmonic generation setup, as group delay dispersion or higher order dispersion terms can rarely be perfectly compensated.

This chapter is based on the article "Peculiarities of Second Harmonic Generation with Chirped Femtosecond Pulses at High Conversion Efficiency » published in Optics communications (volume 455, January 2020), by Pierre-Marc Dansette, Raimundas Burokas, Laurynas Vesely, Audrius Zaukevičius, Andrejus Michailovas and Nerijus Rusteika. Pierre-Marc Dansette performed all the simulations and the final experiments presented in this work. He was the main author of this work. Raimundas Burokas provided the initial experiments indicating a higher-than-expected sensitivity of second harmonic generation to group delay dispersion. Laurynas Veselys provided the source laser for the final experiments and advice. Audrius Zaukevičius helped Pierre-Marc Dansette create the simulation tool used in this article. Nerijus Rusteika and Andrejus Michailovas managed the project.

3.1 INTRODUCTION

Visible ultrashort pulse lasers are useful for a large array of applications, such as spectroscopy [184], non-linear microscopy [185] or micro-machining [186]. Because good broadband laser gain media in the visible range is not available, visible femtosecond pulses can be generated by frequency doubling of near infrared (NIR) femtosecond laser pulses. Furthermore broad tunability can be achieved by optical parametrical amplification or optical parametric generation when pumped with femtosecond visible pulses [140], [187]. Tunable femtosecond pulses in the 600-1300 nm spectral range are used in some bio-photonic applications [188]–[190].

Several parameters are known to control the second harmonic generation (SHG) process for transform limited pulses (TL), such as the non-linear properties of the crystal, the pulse duration, the focusing conditions and the pulse energy [133], [134]. The importance of the spectral phase of the fundamental radiation for SHG was predicted by modelling [191] and observed in BBO and LBO crystals [192]. The spectral phase of the fundamental radiation was shown to be the main parameter governing the second harmonic (SH) pulse duration and its spectrum. Recently it was shown that SHG efficiency in BBO with 300 fs pulses from a Yb:KGW laser drops asymmetrically when the pulses are positively or negatively chirped [158]. It was also shown that the sign of the chirp affects efficiency asymmetrically for surface SHG [193] and SHG in plasma [194]. Lastly, quasi-phasematching with chirped gratings can be used in conjuncture with chirped pulses for frequency doubling [122], [146]. In this article we will expand the viewing of previous work on the effect of spectral phase and chirp [158], [191], [192] to further the analysis of the influence of group delay dispersion (GDD) and higher order dispersion on SHG efficiency and the resulting beam quality.

3.2 NUMERICAL SIMULATION METHODS

Simulations of the second harmonic generation (SHG) was performed using a split step Fourier method [144]. We used a full 3D grid in time and the lateral dimensions x and y of the beam (z being the propagation direction). The second harmonic crystal analyzed in this work was lithium

triborate (LBO), one of the most common nonlinear crystals used for SHG of ultrashort pulses [192], [195]. However most effects are expected to be similar in other nonlinear crystals. The phasematching conditions were calculated using Sellmeier's equations for LBO [196]. The propagation step was performed in Fourier space:

$$E(\omega, k_x, k_y, z + dz) = e^{-i\sqrt{k^2 - k_x^2 - k_y^2}\, dz} \mathrm{E}(\omega, \mathrm{k_x}, \mathrm{k_y}, \mathrm{z})$$ (3.1)

Where ω is the frequency, k_x and k_y the wave vector components in x and y directions and k is the norm of the wave vector. E is the complex amplitude of the electric field envelope. The wave vector norm will depend on the principal refractive indexes of the crystal, n_X, n_Y and n_Z. Here (X,Y,Z) designate the principal coordinate system of the crystal, different from the coordinates we used previously *(x,y,z)*, where z is the propagation direction, defined by angles θ and ϕ to the principal coordinate system. For type 1 phase matching in LBO crystal propagation is in the XY principal plane (θ=90°) and the wave vector in the ordinary polarization is given by:

$$k(\omega) = \frac{n_o(\omega)\omega}{c}$$ (3.2)

Where n_o is the ordinary refraction index, in here equal to n_Z. For the extraordinary polarization direction:

$$k^2(\omega, k_x) = \frac{\omega^2}{c^2} \frac{n_X^2(\omega)n_Y^2(\omega)}{n_Y^2(\omega)\sin^2\phi_{k_x} + n_X^2(\omega)\cos^2\phi_{k_x}}$$ (3.3)

$$\text{With } \phi_{k_x} = \phi_0 - \arcsin\left(\frac{k_x}{k(\omega, k_x)}\right)$$ (3.4)

Where ϕ_0 is the phasematching angle [156]. Equation 3 can be developed to the second order in k_x :

$$k^2(\omega, k_x) = \left(\frac{n_e(\omega)\omega}{c}\right)^2 + A(\omega, k_x)k_x + B(\omega)k_x^2$$ (3.5)

Where n_e is the extraordinary refraction index, $A(\omega, k_x)$ is responsible for spatial walk-off and

$B(\omega)$ for non-paraaxial diffraction :

$$n_e^2 = \frac{n_X^2\, n_Y^2}{n_Y^2 \sin^2 \phi_0 + n_X^2 \cos^2 \phi_0} \tag{3.6}$$

$$A(\omega, k_x) = -n_e^4 \frac{\omega}{c} \frac{n_X n_Y \sin(2\phi_0)\, (n_X^2 - n_Y^2) \sqrt{\dfrac{n_X^2 n_Y^2}{n_e^2} - \dfrac{k_x^2 c^2}{\omega^2}}}{n_X^4 n_Y^4} \tag{3.7}$$

$$B(\omega) = n_e^4 \frac{n_Y^4 \sin^2 \phi_0 + n_X^4 \cos^2 \phi_0 - n_X^2 n_Y^2}{n_X^4 n_Y^4} \tag{3.8}$$

With k as defined above, the linear propagation accounts for full material dispersion, non-paraxial diffraction and spatial walk-off due to birefringence. The non-linear propagation step was performed in real space. For each dz step, self- and cross-phase modulation were accounted for using a zero order approximation:

$$E_f(z + dz) = E_f \exp\left(-j \frac{n_2 \epsilon_0 \omega_0}{2}\left[n_o(\omega_0)|E_f|^2 + \frac{2}{3} n_e(2\omega_0)|E_{SH}|^2\right] dz\right)$$

$$E_{SH}(z + dz) = E_{SH} \exp\left(-j n_2 \epsilon_0 \omega_0 \left[\frac{2}{3} n_o(\omega_0)|E_f|^2 + n_e(2\omega_0)|E_{SH}|^2\right] dz\right) \tag{3.9}$$

Where ω_0 is the central frequency of the fundamental radiation, ϵ_0 the vacuum permittivity, E_f and E_{SH} the complex amplitudes (at z unless specified) of the fundamental and second harmonic radiations respectively. To lighten notations we left out the *(x,y,t)* dependence of the fields. This equation as well as equation 3.10 are applied to each position *(x,y,t)* in the grid. n_2 is the non-linear refractive index (for LBO $2.6\ 10^{-20}\ m^2/W$ [197]).

The second harmonic generation is performed using a fourth order Runge-Kutta method [177], meaning we had a precision up to the fourth order on the z step. SH generation was characterized by the effective non-linear coefficient d_{eff} calculated from the second order susceptibility matrix [149] and given by the following system of coupled equations:

$$\begin{cases} \dfrac{dE_{\mathrm{f}}}{dz} = j\,\dfrac{\omega_0 d_{\mathrm{eff}}}{n_o(\omega_0)c}\,E_{\mathrm{f}}^{*}E_{\mathrm{SH}} \\[3mm] \dfrac{dE_{\mathrm{SH}}}{dz} = j\,\dfrac{2\omega_0 d_{\mathrm{eff}}}{n_e(2\omega_0)c}\,E_{\mathrm{f}}^{2} \end{cases} \tag{3.10}$$

The algorithm starts with a half step of propagation (equations 3.1 to 3.8) performed in Fourier space (k_x, k_y, ω), followed by a Fourier transform to come back to real space (x, y, t) and a half step of phase modulation (equation system 3.9). Then we iteratively perform a full step of non-linear mixing (equation system 3.10), a full step of propagation and a full step of cross and self-phase modulation. The last step consists in a full step of non-linear mixing, a half step of propagation and a half step of cross and self-phase modulation. This means the nonlinear mixing is performed with a half step shift in comparison to propagation and phase modulation. This method slightly diverges from a classic split step Fourier method, in which all non-linear phenomena – meaning the nonlinear mixing and the phase modulation – are calculated with a half step shift in comparison to the linear step – the propagation in Fourier space. However, we did not wish to implement a Runge-Kutta algorithm on both cross and self-phase modulation and the nonlinear mixing. This allows us to gain processing speed. Thus, we treated phase modulation with the linear part. We note that phase modulation depends only on intensity (equation 3.9). For typical values of group velocity dispersion intensity varies only little due to propagation, but the SH intensity will initially increase exponentially with propagation length. Therefore, it is better to treat phase modulation at a half step shift with the nonlinear mixing.

The input pulse at the fundamental wavelength was modelled using a Gaussian spectrum and introducing some spectral phase tailored with second, third and fourth order dispersion. The beam quality, defined as the focusability parameter M^2, was calculated by applying an analytical formula [114] to the modelled beam after propagation :

$$M^2 = \frac{w_k^2 w^2}{2}\left(1 - \frac{w^2 k^2}{w_k^2 R^2}\right) \tag{3.11}$$

Where w and w_k are respectively the beam radius and angular width, calculated by the $D4\sigma$ [198] method, k is the wave vector and R the radius of curvature of the wave front [180]. The beam

focusability parameter depends only on the spatial properties of the beam, not on the temporal or spectral properties (such as GDD). It will not be affected by diffraction or spatial walk-off, but can be affected by cross and self phase modulation (Eq. 9) as well as the mixing process (equation 10) as those are intensity dependent.

3.3 NUMERICAL SIMULATION

We performed a set of simulations with transform limited Gaussian pulses with durations from 30 fs to 1 ps (FWHM) and central wavelength of 1030 nm. The spatial beam profile was also assumed Gaussian and the beam diameter ($1/e^2$) in the crystal was set at 300 µm. For this diameter the corresponding Rayleigh length in LBO was 110 mm, much longer than all crystals lengths considered in this work (0.8 – 15.9 mm). Though diffraction could be neglected, it was included in simulations anyway. Below we will present the results of numerical simulations exploring the effects of group delay dispersion (GDD) and higher order dispersion on SHG efficiency and SH beam quality for different pulse intensities, bandwidth and crystal lengths.

3.3.1 Effect of peak intensity at the fundamental wavelength

As a starting point in simulations, we chose Gaussian pulses with transform limited duration of 300fs and the initial crystal length was set to be equal to the group velocity mismatch length (L_{GVM}) between the pulses at the fundamental and SH. For LBO crystal at the chosen pulse parameters, this corresponds to 4.8 mm. The incident pulse peak intensity was varied from the lowest value of 0.89 GW/cm^2 to the highest of 89 GW/cm^2, which corresponded to pulse energies from 100nJ to 10µJ (Table 3.1, the first and the second columns). Additional modelling results are also presented in Table 3.1: Efficiency of the conversion to SH, accumulated non-linear phase (B integral[161]) and the SH pulses focusability parameter M^2.

Intensity (GW/cm^2)	Energy (μJ)	B integral (rad)	Efficiency (%)	M^2
0.89	0.1	0.003	22	1
1.77	0.2	0.009	35.8	1.01
17.7	2	0.2	82.6	1.03
44.3	5	0.58	90.9	1.05
88.6	10	1.19	80.9	1.8

Table 3-1: Peak conversion efficiency to the SH for different peak intensities of the fundamental wavelength beam obtained from the numerical simulation for 300fs pulses and 4.8mm long LBO crystal. B-integral for SH pulses and M^2 parameter for the SH beam obtained from the same simulation are also provided.
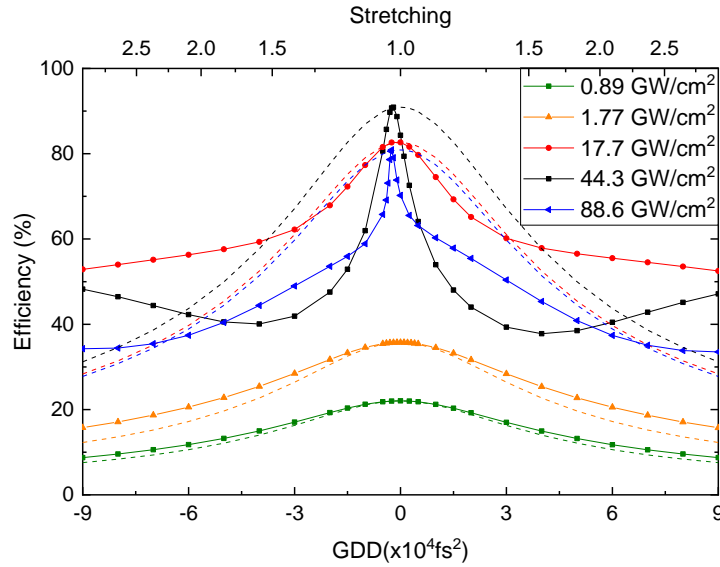
Figure 3-1: Numerical simulation results of SHG conversion efficiency as a function of GDD applied to pulses at the fundamental wavelength for different values of peak intensity (solid curves) and SHG efficiency dependence on GDD using a simple model disregarding depletion at the fundamental wavelength and phase effects (dashed curves), normalized so that the peak efficiency is the same as in numerical simulation. The pulse stretching factor (duration divided by TBW duration when GDD=0fs^2) caused by GDD (bottom axis) is indicated on the top axis.

A modeled dependence of SHG conversion efficiency on GDD of the pulses with different intensities is shown in Figure 3.1 by solid lines. The modelled range of GDD corresponds to a relatively small stretching of the pulse (up to 3 times time bandwidth (TBW) limited pulse

duration, see top axis). It is worth to note that the stretching dependence on GDD is non-linear (it becomes asymptotically linear for large values of GDD). For all pulse intensities, peak efficiency is achieved at GDD close to zero, with a slight shift to negative GDD when intensity is increased, up to GDD = -2500 fs^2 at 88.9 GW/cm^2. Peak conversion efficiency of 90.9% is reached at around 44.3 GW/cm^2 peak intensity of the fundamental radiation and decreases to 80.9% for the highest peak intensity within simulation conditions (table 3.1). This effect is well known as being caused by back-conversion of the energy of the SH pulse to the fundamental radiation [134], [199]. For all modeled intensities, efficiency falls down at both positive and negative GDD approximately symmetrically in respect to the peak. However, the drop rate vs introduced GDD dramatically depends on the intensity.

One of the effects of GDD is to increase pulse duration. When the pulse at the fundamental wavelength is stretched we expect the SH conversion efficiency to drop. In order to estimate the role of pulse stretching on the SH conversion efficiency, we compare fully modelled efficiency dependence on GDD with the one which results from a simple model. In this model it is assumed the SH pulse energy is proportional to the integral of the squared peak intensity of the fundamental radiation [153].

$$\epsilon_{SH} \propto \int I_f{}^2 dt \qquad (3.12)$$

Where I_f is the peak intensity of the fundamental radiation and ϵ_{SH} the energy at the second harmonic wavelength. This model accounts only for pulse duration change due to dispersion. This approximation is valid only if we can neglect the depletion of the fundamental radiation, which is clearly not the case at higher conversion efficiency, as well as if phase effects are ignored. Those approximation are not necessarily valid with the chosen simulation parameters, but this model provides a useful estimate of the expected effect of GDD in practical situations. For Gaussian pulses, conversion efficiency scales as an inverse of time bandwidth (TBW) limited pulse duration τ within this model. At very low peak intensity of the fundamental radiation (0.89 GW/cm^2), we observe a good match between the simplified theoretical behavior (dashed curves) and the fully modeled curve of efficiency. For example, at 80 000 fs^2 GDD pulse duration is stretched from 300

fs to 800 fs and therefore efficiency with this simple model falls ~2.7 times from the peak. Full model puts it at 2.5 times lower - quite a good match. When peak intensity is increased to 1.77 GW/cm2, the drop of SHG efficiency vs GDD gets slower for the full model in comparison with $1/\tau$ simplified theory, which can easily be explained by the depletion of the fundamental radiation causing a flatter curve. However, at higher intensities, starting from 17 GW/cm^2, this behavior is reversed: starting from 17 GW/cm^2 conversion efficiency dependence on GDD becomes steeper in comparison to the simplified model. At the highest intensities SHG efficiency manifest extremely fast drop around the peak. This behavior dramatically differs from results predicted by simplified model We note that at high fundamental radiation peak intensities (44.3 GW/cm^2 or 88.9GW/cm^2) SH conversion efficiency reaches local minima for positive and negative GDD. The SH conversion efficiency increases for larger values of absolute GDD only until a certain point. For instance, at fundamental radiation peak intensities of 44.3 GW/cm^2 a local maxima of 52.5% SH conversion efficiency is reached at ±165 000 fs^2 of GDD. It then starts to decrease for larger amounts of GDD and asymptotically decrease as 1/GDD. Generally, the simplified model remains valid only in the asymptotic case when GDD tends to ±∞, where the assumption that fundamental depletion can be neglected remains valid.
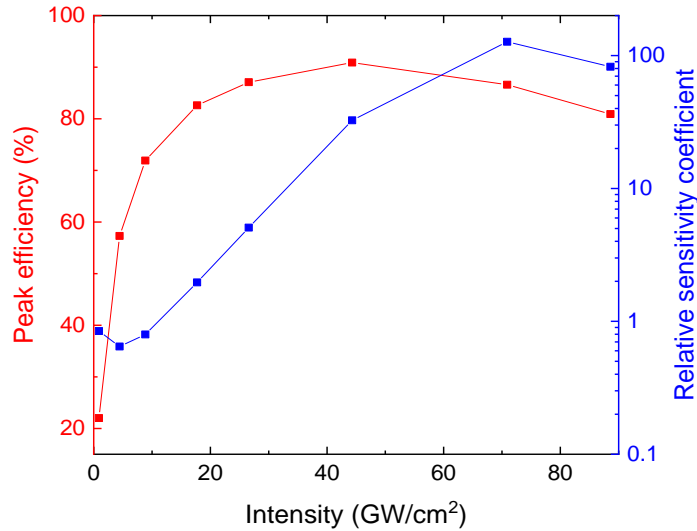
Figure 3-2: Left axis: Dependence of peak SHG conversion efficiency on the peak intensity at the fundamental wavelength (red curve); Right axis : Dependence of the SHG conversion efficiency sensitivity coefficient on the peak intensity at the fundamental wavelength (blue curve). See explanations in the text.

To quantify this behavior we introduced a parameter α characterizing the sensitivity of the SHG conversion efficiency (η) to GDD variations. To calculate this sensitivity coefficient, a second order fit was performed on the relative SHG efficiency curve as a function of GDD near the peak. In figure 3.2, this coefficient is given relative to the GDD sensitivity of SHG conversion efficiency in a simplified model, when we neglect fundamental radiation depletion and phase effects. It characterizes the "sharpness" of the "SHG efficiency peak". The absolute value of the sensitivity coefficient of SHG conversion efficiency to GDD in the simplified model is 4.02×10^{-8} %/fs^4 for the chosen pulse duration (independent on intensity). This value was used throughout as a reference sensitivity and modeled sensitivity was normalized to it. The dependence of this normalized sensitivity parameter is shown in figure 3.2 alongside the peak SHG conversion efficiency dependence on the peak intensity of the fundamental radiation. At high intensities this parameter gets very large (sensitivity is ~120 times larger for 44GW/cm^2 peak intensity than that in the simplified model) and can limit practical applications of SHG in actual femtosecond laser systems with such high conversion efficiency. For example, a practical femtosecond laser system with chirped pulse amplification may have a GDD in stretcher or compressor of the order of 30ps^2 (or 3.10^7 fs^2, corresponding to ~280 ps stretched pulse duration). The change of this dispersion by 0.01% would correspond to a GDD change of 3000 fs^2. This change would affect conversion efficiency only slightly (<0.5% change) at relatively low pulse peak intensity (< 10 GW/cm^2), but for a pulse peak intensity around 40 GW/cm^2 which corresponds to highest efficiency (~91%), this change would decrease efficiency by ~12%, which would be prohibitive for most practical applications.

Figure 3-3: Beam quality parameter M^2 of the SH beam as a function of GDD applied to the fundamental wavelength pulse for different values of its peak intensity.

Further, we investigated the dependence of the beam quality parameter (M^2) on the introduced GDD. The response of the beam quality to GDD variations was quite unexpected (figure 3.3). Firstly, at the same low GDD value corresponding to efficiency peak (from 0 to -2500 fs^2 depending on peak intensity), the beam quality is very good ($M^2 \leq 1.05$) for all pulse intensities up to 44 GW/cm^2 where absolute efficiency peaks. Only for the highest peak intensity of 89 GW/cm^2 beam quality gets significantly reduced ($M^2 = 1.8$) at low GDD. At low peak intensity (below 20 GW/cm^2) M^2 remains below 1.05 for all modelled values of GDD. However at 44 GW/cm^2 beam quality rapidly worsens when GDD is changed from the value corresponding to the peak of efficiency. M^2 reaches maxima of ~2.3 for GDD around ±30 000 fs^2. For larger amounts of GDD M^2 improves again. Similar M^2 dependence is observed at lower intensities, though M^2 increases to lower maximal values depending on intensity. At the highest modeled fundamental radiation peak intensity of 89 GW/cm^2 M^2 rises sharply to ~2.6 when small amounts of GDD are introduced, but then remains largely flat in the modeled range of ±90 000 fs^2 and starts improving for higher GDD.

The dependence of M^2 and SH conversion efficiency on GDD mirror each other. As the peak of efficiency gets narrower, the rise of M^2 gets steeper too. We did not estimate the sensitivity parameter for M^2, but it correlates very well with the sensitivity parameter for efficiency.
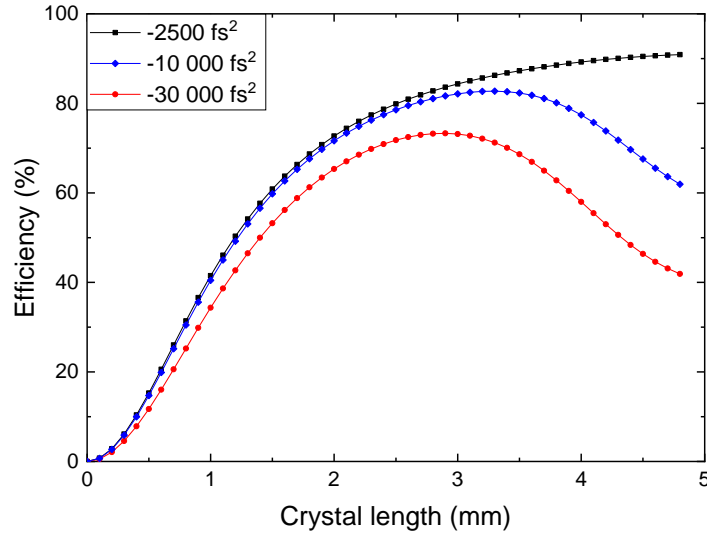
Figure 3-4: Numerical simulation results of energy conversion efficiency from the fundamental to SH wavelength as a function of crystal length for different values of GDD applied to the fundamental wavelength pulse. Pulse energy was kept at 5µJ in all cases.

To better understand these dependences, we calculated the conversion efficiency as a function of propagation length in the crystal for different amounts of GDD (Fig 4.). At 44 GW/cm^2 for the value of GDD corresponding to peak efficiency (GDD =-2500 fs^2), efficiency increases along the crystal up to the maximal simulated length of 4.8 mm. However when GDD of -30 000 fs^2 is introduced, at first efficiency increases with added crystal length up to 72% for a 2.7mm long crystal, and then starts decreasing down to 40% for the maximal modelled length of 4.8 mm. This indicates back conversion from the SH to the fundamental radiation. The length of crystal after which back conversion starts varies with the introduced amount of GDD. It is known that back conversion negatively affects beam quality, and its effect vary with intensity. Thus, both the behavior of M^2 and of conversion efficiency is caused by back conversion. For the highest modelled peak intensity of 89GW/cm^2 (not plotted), back conversion is observed even at the peak of efficiency. At GDD= ±30 000 fs^2, there is actually a full cycle of conversion and back conversion: After a short length of crystal (2.1 mm) back conversion starts and efficiency starts to drop, and further on (after 3.9 mm) conversion restarts and efficiency increases again. This might explain the qualitative difference in the dependence of M^2 and SH conversion efficiency on GDD that we observed for this peak intensity.

3.3.2 Effect of crystal length

Due to the very high sensitivity of SH conversion efficiency of femtosecond pulses on GDD at high intensity, a natural question arises: Are there conditions when high conversion efficiency can be achieved in relatively broad GDD range with good beam quality? Trying to answer this question, we performed a set of simulation for different crystal lengths. We selected the peak intensity of the fundamental radiation so, that peak efficiency was close to 90% in all cases. The required intensities to achieve this peak conversion efficiency are tabulated in table 3.2 for different crystal lengths. At low conversion efficiency, disregarding phase effect and the depletion of the fundamental radiation, conversion efficiency should be proportional to $L^2 I_f$, where L is the crystal length and I_f is the peak intensity of the fundamental radiation. Thus, the required peak intensity to maintain the same SH conversion efficiency should vary as $1/L^2$. At high conversion efficiency those assumptions obviously do not hold and the required peak intensity scales at a lower rate with crystal length (Table 3.2). For instance reducing crystal length 7.5 times (from 6mm to 0.8 mm) requires the increase of peak intensity 34 times only (instead of 56 if the $1/L^2$ dependence held). However, peak intensity scales much faster than $1/L$. Therefore B integral, which is an integral of peak intensity multiplied by the non-linear refractive index n_2 over the crystal length, increases for shorter crystal while SH peak conversion efficiency is kept at 90%. In practice it will limit the use of very short crystals for SHG.

L (mm)	I_f (GW/cm^2)	E (μJ)	B integral (rad)	M^2
0.8	1063	120	2.14	1.31
1.5	310	35	1.21	1.12
3	88.6	10	0.71	1.06
4.8	44.3	5	0.58	1.05
6	31	3.5	0.51	1.06

Table 3-2: Required fundamental radiation peak intensity I_f and corresponding pulse energy E required to maintain a 90% SH peak conversion efficiency for different nonlinear crystal lengths

L, for 300 fs pulse duration and 300 µm beam diameter. B-integral for SH pulses and M^2 parameter for the SH beam are calculated for the tabulated crystal lengths and intensities
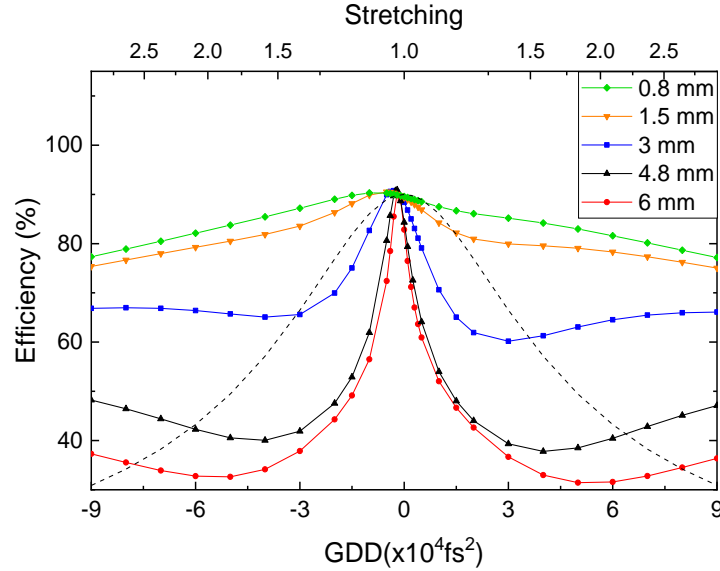
Figure 3-5: Numerical simulation results of conversion efficiency from the fundamental to SH wavelength as a function of GDD applied to pulses at the fundamental wavelength for different values of the crystal length (solid curves) when the fundamental radiation peak intensity is chosen so that peak efficiency is close to 90%. Relative efficiency using a simple model disregarding depletion of the fundamental radiation and phase effects (dashed curve), normalized to the peak efficiency of 90% is presented for comparison

The evolution of efficiency with GDD for the different combinations of crystal length and peak intensity is shown in figure 3.5. We notice that the sharpness of the efficiency peak decreases rapidly as the crystal length is reduced. For crystals of 1.5 mm or less the peak is even much less sharp than a $1/\tau$ curve (the very simplified model described in section 3.1). For crystals shorter than 3 mm the curve is asymmetric for positive and negative dispersion, which may explain previous experimental observations of asymmetry with respect to GDD[158], [193], [194]. It is also notable that the shorter the crystal length is (and the higher the peak intensity) the more efficiency peak shifts to the negative GDD. For a 0.8 mm crystal the peak is reached at -10 000 fs^2. Both the asymmetry and the shift of the efficiency peak toward negative GDD are related to Kerr effect: switching off Kerr effect in simulations (n_2=0) leads to symmetrical efficiency curves with a peak around 0 fs^2.

The calculated parabolic coefficient of relative sensitivity α (figure 3.6) drops from ~45 for a 6mm crystal to ~0.3 for a 0.8 mm LBO crystal. The values are indicated relative to the parabolic

coefficient α of the simplified model (when depletion and phase effects are neglected). This is a much more favorable situation for practical purposes, but we notice the required peak intensity also increases up to 1TW/cm^2, which would be prohibitive due to surface damage of the LBO crystal with femtosecond pulses. Damage threshold, extrapolated from picosecond damage studies [200], should be of ~400GW/cm^2 for 300fs duration pulses, assuming $1/\sqrt{\tau}$ scaling of threshold damage peak intensity. However, accounting for the damage threshold of anti-reflection coatings on the crystal and the fact that practical SHG system with modern lasers should be operational for up to 10^{14} pulses (corresponding to 3 years of operation at 1MHz repetition rate) a reasonable practical limit (albeit somewhat arbitrary) for LBO crystal has to be set at ~100GW/cm^2 for 300fs pulse duration. At this peak intensity the relative sensitivity of the SH conversion efficiency on GDD parameter is ~5 with 3mm long LBO crystal, which is still quite high (~2% change in efficiency for 3000fs^2 change in GDD). Thus, we could not find very favorable conditions to achieve 90% efficiency with 300fs pulses. Either the sensitivity to GDD is too large (for long crystals), or peak intensity is too high (for short crystal).
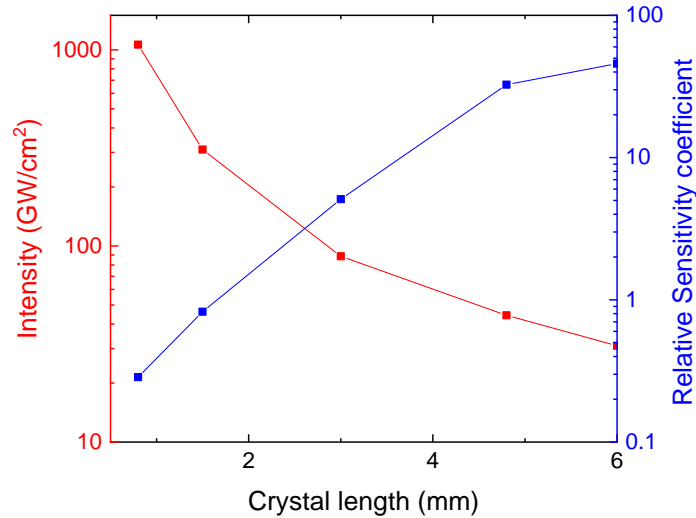
Figure 3-6: Left axis: Peak intensity of the fundamental radiation required for 90% or higher efficiency of the conversion to SH (red curve); right axis: Dependence of the conversion efficiency sensitivity coefficient on the length of the crystal (blue curve).

We performed a second set of simulations for the same crystal lengths but optimizing the peak efficiency to around 80%. To achieve this efficiency for different crystal lengths, required fundamental radiation peak intensity is given in table 3.3, along with corresponding pulse energy

(for the same 300fs pulse duration and 300μm beam diameter) as well as calculated GDD sensitivity parameter α, B integral and M^2 parameter. Firstly, somewhat unsurprisingly, the sensitivity of conversion efficiency to GDD is greatly reduced in comparison to 90% efficiency case. It still increases with crystal length, but for peak intensity of around 100GW/cm^2 sensitivity parameter decreases from ~5 for 90% efficiency to 0.3 for 80%, corresponding to a 0.1% SH power change for a GDD change of 3000fs^2 and ~1% for 10 000fs^2, which is more than 3 times lower than predicted by $1/\tau$ scaling. At 3mm crystal length a good compromise between fundamental radiation peak intensity (31 GW/cm^2) and sensitivity to GDD (~0.6 times the sensitivity for $1/\tau$ dependence) is achieved. In general, to optimize the crystal length for maximal practical second harmonic efficiency one should have a target efficiency as well as should know the allowed peak intensity on the crystal and the allowed sensitivity to GDD.

L (mm)	I_f (GW/cm^2)	E (μJ)	B integral (rad)	α	M^2
0.8	398	45	0.73	0.24	1.08
1.5	115	13	0.39	0.3	1.03
3	31	3.5	0.21	0.58	1.02
4.8	14	1.6	0.16	1.25	1.03
6	9.7	1.1	0.13	1.81	1.03

Table 3-3: Required fundamental radiation peak intensity I_f and corresponding pulse energy E to maintain a conversion efficiency to SH of 80% for different crystal lengths, for 300 fs pulses and 300 μm beam diameter. B-integral for SH pulses, conversion efficiency's sensitivity coefficient to GDD α (relative to the sensitivity when depletion and phase effects are neglected) and M^2 parameter for the SH beam obtained from the same simulation are also provided
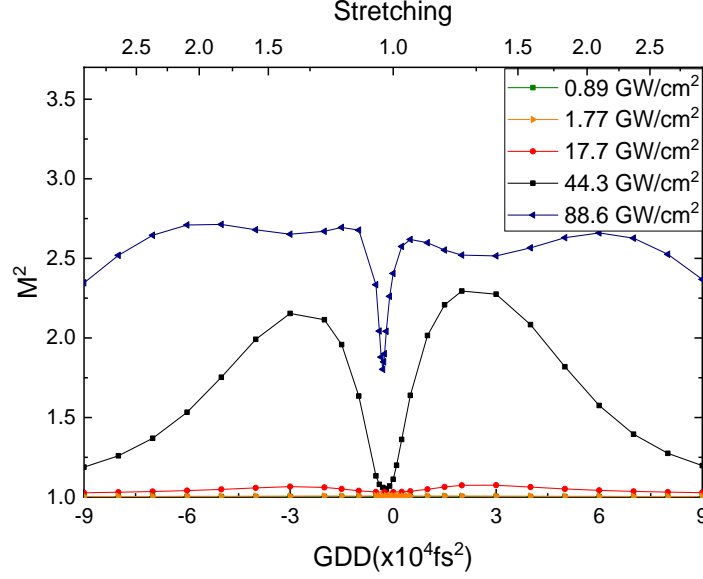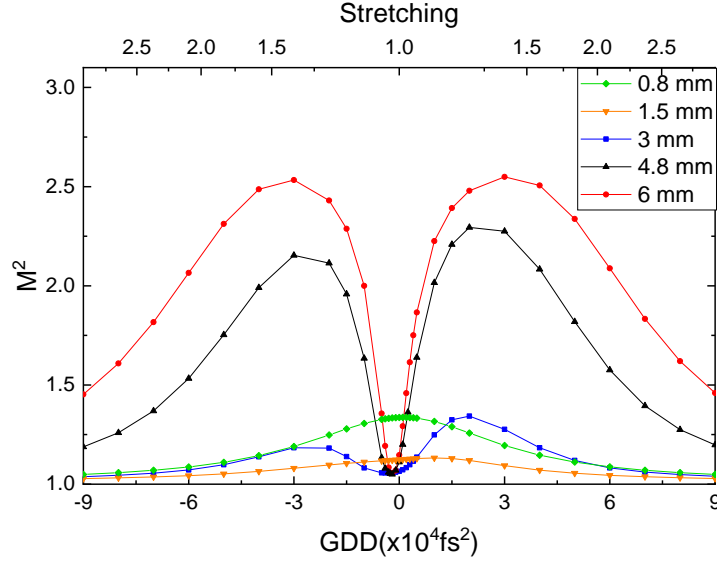
Figure 3-7: Beam quality parameter M^2 of the SH beam as a function of GDD applied to the pulse at the fundamental wavelength for different values of the crystal length, when the fundamental radiation peak intensity is chosen so that the peak efficiency is ~90%

The simulation results on dependence of beam quality parameter on GDD for different LBO crystal lengths at fixed SH efficiency of 90% are given in figure 3-7. For crystal lengths of 4 to 6mm behavior is very similar as in 4.8mm crystal length case described in section 3.1 (figure 3-3): M^2 is very good (<1.1) at low GDD corresponding to the peak of SH conversion efficiency. M^2 then rises for both negative and positive GDD and peaks at ~±30 000fs^2. At this point the worst beam quality is observed for the longest crystal (6mm) at $M^2 = 2.5$. For intermediate crystal length of 3mm the worst beam is at positive GDD of ~20 000fs^2 with $M^2 = 1.3$. At negative GDD of -20 000fs^2 M^2 is ~1.2 showing significant asymmetry in regard of the sign of the chirp. We found that the main driver of the observed asymmetry is Kerr effect in the nonlinear crystal, as when a simulation was run at $n_2 = 0$, asymmetry in respect to GDD sign disappeared. For the shortest crystal lengths of less than 2mm there is a single peak around 0 fs^2. This is in line with what we would expect from simple self-phase modulation in nonlinear medium [182]. Indeed from numerical simulation we obtained a B integral of 2.1 rad for the shortest crystal (0.8mm) at the peak of 90% efficiency, which according to [182] should yield an M^2 of 1.25, which is very close to $M^2 = 1.3$ from numerical simulation. We also confirmed this by running a simulation of nonlinear propagation of only SH beam at the same B integral value (2.1 rad) and obtained beam quality parameter of $M^2 = 1.27$ confirming the hypothesis that beam quality for short crystal length deteriorates primarily due to accumulation of nonlinear phase from self-phase modulation. In the case of SHG in short crystals, the efficiency gets lower when GDD is introduced, following the reduction of B integral for stretched pulses.

3.3.3   Extension to different pulse durations with different bandwidth

After investigating the effects of GDD on efficiency and beam quality of the SH in different combinations of intensity, crystal length and peak efficiency for 300 fs initial pulse duration of the fundamental radiation, an obvious question arises: can these observations be generalized for different pulse durations? To answer to that we performed a set of simulations for different initial pulse durations τ (at GDD=0 fs^2) between 30 fs and 1ps. We previously observed that sensitivity to GDD decreases when the crystal length is reduced and the fundamental radiation peak intensity increased to maintain high efficiency (section 3.2). The main practical limitation is the practical maximum peak intensity for the nonlinear crystal, which we previously estimated at ~100GW/cm^2 for a 300fs pulse duration. The dependence of peak intensity damage threshold on pulse duration in subpicosecond regime is somewhat complicated - different studies provide different results [111], [201]. In most cases the dependence can be assumed to fall in between $1/\sqrt{\tau}$ and $1/\tau$. By running additional simulations not shown here, we did not find a qualitative difference in the results between $1/\sqrt{\tau}$ and $1/\tau$ peak intensity scaling and therefore only analyze $1/\sqrt{\tau}$ case bellow. Assuming $1/\sqrt{\tau}$ scaling, maximal allowed peak intensity can be calculated for different pulse durations. We also optimized the crystal length for each pulse duration so that SH conversion efficiency is maximized (table 3.4).

τ (fs)	L (mm)	I_f (GW/cm^2)	B int. (rad)	η_{max} (%)	α	M^2
30	1.5	337	1.03	79.9	8.2	1.12
100	2.3	183	1.09	87.8	31	1.12
300	3.2	106	0.93	91.7	14	1.08
1000	4.2	58.2	0.68	92.3	1.5	1.06

Table 3-4: Crystal length L that maximize the SH conversion efficiency peak for different TBW limited pulse durations τ of the fundamental radiation with the fundamental radiation peak intensity I$_f$ set at the estimated surface damage threshold. For a 30fs pulse duration, L is limited by the phasematching bandwidth. The peak of efficiency η_{max} is provided, along with B-integral (B int) for SH pulses, a relative sensitivity coefficient α to GDD and M² parameter

for the SH beam obtained from the same simulation. To obtain α the absolute sensitivity is divided by the sensitivity parameter for the simplified model (when depletion and phase effects are neglected), which scales as τ^4.
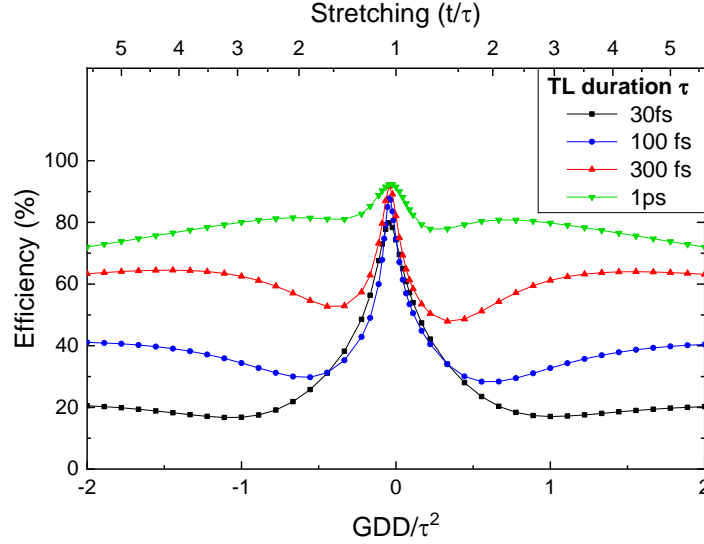
Figure 3-8: Numerical simulation results of SH conversion efficiency for different values of the initial TBW limited pulse duration τ of the fundamental radiation, when crystal length is chosen to maximize peak efficiency and the peak intensity of the fundamental radiation is set to the damage threshold. On the top axis, the pulse stretching ratio t/τ (pulse duration divided by the TBW limited duration) is shown, which corresponds to the normalized GDD shown on the bottom axis.

A different criterium had to be used for the shortest (30fs) initial pulse duration, as the peak conversion efficiency keeps slowly rising with crystal length (up to 90%), even for crystals as long as 15mm. This behavior is unlike what we observed at longer pulse durations, where the peak of efficiency reaches a maximum, and then starts to decrease due to back conversion. But for a 30fs pulse, the group velocity mismatch length (L_{GVM}) is ~0.5 mm, so after 1mm of crystal or more, pulses at the SH and fundamental wavelength are completely temporally separated. Because of this, there can be almost no back conversion. However, using extremely long crystals for very short pulses is unpractical, since the gain in efficiency with long crystal comes at the cost of longer SH pulses, which defeats the purpose of using very short pulses in the first place. Thus, we limited ourselves to a 1.5 mm crystal for a 30fs. For all other pulse durations the crystals are sufficiently short so that there is no problem of phase matching bandwidth. Indeed we note that for all considered parameters, at the peak of conversion efficiency the SH pulse duration when exiting the crystal was very close to the initial pulse duration of the fundamental radiation, what could be

expected for high conversion efficiency. We also calculated the TBW limited pulse duration of the SH, which varied from 16% shorter than the TBW limited pulse duration τ of the fundamental radiation for $\tau = 1$ps, to 27% shorter for $\tau = 100$fs.

The SHG efficiency dependence on normalized GDD (divided by the square of the TBW limited pulse duration τ) is shown figure 3-8. The choice of using normalized GDD scale levels the differences between pulses with different initial bandwidth. The stretching (as a fraction of TBW limited duration) associated with normalized GDD is the same for all bandwidths (figure 3.8, top axis). The sharpness of the efficiency peak increases with shorter pulse durations down to 100fs. For a fundamental radiation TBW limited pulse duration of 30 fs, the peak is less sharp (table 3.4), but peak conversion efficiency is significantly lower (80%). The SH conversion efficiency dependence on GDD always displays local minima, which are observed at larger normalized GDD values for shorter pulses. As, e.g., at GDD $\approx \pm 0.3$ τ^2 for a 1ps pulse, and at GDD $\approx \pm 1 \tau^2$ for a 30 fs pulse. SH conversion efficiencies at minima varies from 80% for a 1 ps pulse to 17% for a 30 fs pulse. For larger amounts of added GDD, the efficiency reaches local maxima before dropping again.

The behavior of the beam quality parameter (figure 3-9) is very similar to that was described in previous sections, with the value of M^2 at local maxima increased when pulse duration shortened from 1ps to 100fs. For a 1ps pulse duration, beam quality remained relatively good for all modelled values of GDD, with $M^2 < 1.15$. For a 30 fs pulse the maxima of M^2 were reached at larger values of GDD (GDD $\approx \pm 0.7 \tau^2$) than for longer pulse duration (GDD $\approx \pm 0.3 \tau^2$), but their value is lower than for a 100 fs pulse (maximum M^2 of 2.45 for a 100fs pulse duration and 2.12 for a 30 fs pulse). A possible explanation for this is the temporal separation between pulses at the fundamental and SH wavelength, due to group delay mismatch. Indeed, for a 30fs pulse L_{GVM} is ~0.5 mm, 3 times shorter than the crystal length (1.5 mm). We saw previously that the worsening of beam quality and the drop in SH conversion efficiency when GDD is introduced comes from back conversion (section 3.1). However, since the pulses are no longer temporally well overlapped there can only be very little back conversion. As L_{GVM} increases with pulse stretching, so there can still be back conversion when pulse are stretched.
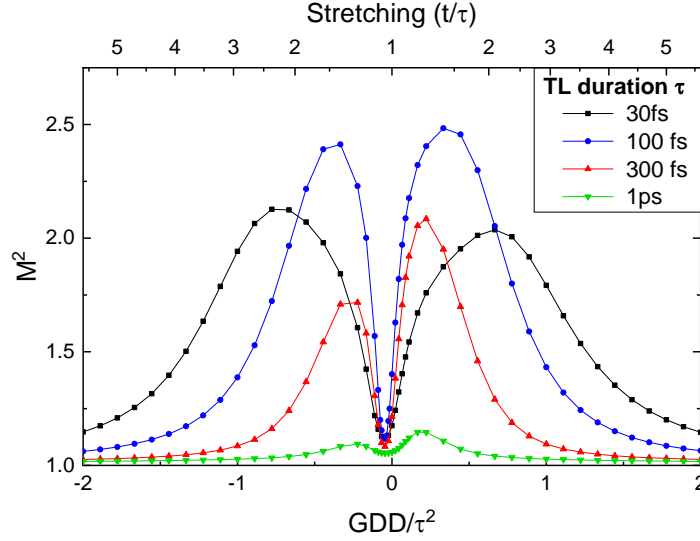
Figure 3-9: Beam quality parameter M^2 of the SH beam as a function of normalized GDD (i.e. GDD divided by the square of the initial TBW limited pulse duration τ) of the pulse at the fundamental wavelength for different values of τ, when crystal length is chosen to maximize peak efficiency and the fundamental radiation peak intensity is set to the damage threshold.

While SHG efficiencies of 60% are regularly achieved for pulses longer than 100 fs [146], [158], [202], achievable efficiency tends to drop for shorter pulses. Our numerical simulation clearly shows that it is indeed difficult to achieve practically high conversion efficiency for very short pulses. Peak efficiency drops because for very short pulse durations the crystal length is limited by the phasematching bandwidth and the fundamental radiation peak intensity is limited by the damage threshold of the nonlinear crystal. Furthermore, conversion efficiency is still very sensitive to GDD near the peak and can drop to only ~20% for stretched pulses (2 times or more).

Generally, the sensitivity of SH conversion efficiency and SH beam quality parameter M^2 on GDD is more problematic for very short pulses. For pulses of 1ps or longer it is possible to operate at the highest achievable peak efficiency and have a relatively low sensitivity to GDD. But for pulses of a few hundred femtosecond, the only way to obtain practically acceptable sensitivity to GDD is to operate at lower peak efficiency (i.e. use a shorter crystal or lower the fundamental radiation peak intensity).

3.3.4 Influence of higher order dispersion

In many practical situations, the spectral phase of ultrashort pulses may not only possess a quadratic spectral dispersion term (linear chirp), but also higher order spectral dispersion terms due to imperfectly compensated dispersion, nonlinear effects, or both [203]. As quadratic spectral phase is the first expansion term in Taylor series, in our modelling we looked at the influence of higher order phase terms only as a contributing factor to the effects of linear chirp. Indeed, it is difficult to imagine a practical system (but it is definitely feasible to construct one) where only third or fourth order spectral dispersion terms would change, while GDD is constant.

In this section, the initial conditions of simulation were chosen to be the same as in part 3.1: TBW limited pulse duration of the fundamental radiation was 300fs and the initial beam diameter was 300 µm, with a 4.8 mm LBO crystal length and fundamental radiation peak intensity of 44.3 GW/cm^2 at GDD=0fs^2.
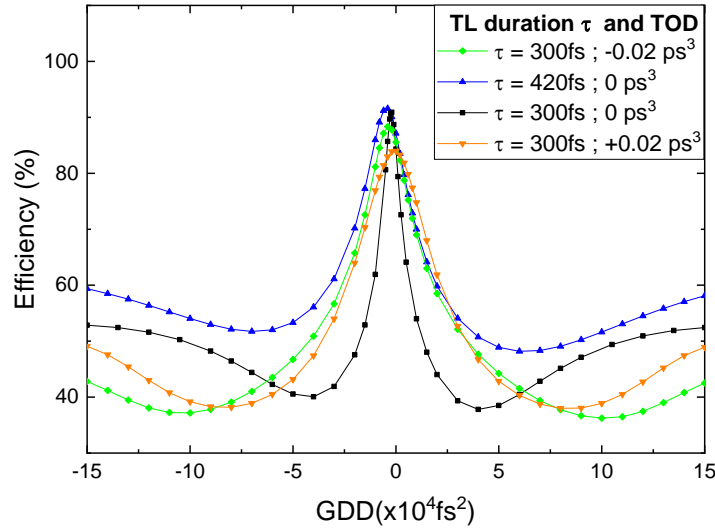
Figure 3-10: Numerical simulation results of conversion efficiency from fundamental to SH wavelength as a function of GDD at the fundamental wavelength, for different values of TOD and TBW limited pulse duration τ of the fundamental radiation. Crystal length is set at 4.8 mm and fundamental radiation peak intensity at GDD = 0 fs^2 is 44.3 GW/cm^2 in all cases

At first, the effect of GDD when a large amount of third order dispersion (TOD), corresponding to a cubic spectral phase term, was investigated. TOD value of ±0.02 ps^3 was chosen such, that initial pulse duration at GDD = 0 fs^2 increased quite significantly (from 300 fs to 420 fs) but

temporal Strehl ratio [204], [205] relative to the Gaussian pulses of the same FWHM duration (420 fs) was still high (92%). It indicated that pulses are still of good temporal quality. Energy of the pulses with cubic phase was increased to 7.3 µJ to keep the same peak intensity of 44GW/cm^2. The evolution of SHG conversion efficiency versus GDD with and without cubic phase is shown Figure 3.10. We also plotted the dependence of efficiency on GDD for a 420 fs TL pulse with the same peak intensity (corresponding to 7µJ pulse energy). The obtained efficiency peak got smoother when TOD increased. The maximal efficiency also decreased. The first conclusion is that the effect of the sign of TOD is relatively small: peak efficiency is lower for positive TOD (84% in comparison to 88.2%), sensitivity on GDD is slightly lower for positive TOD and the local minimum of efficiency at around GDD = $\pm$100 000 fs^2 is higher for positive TOD than for negative TOD (45% vs 38%). Around the peak of efficiency the dependence on GDD is very similar to that of a TL pulse of the same duration (420 fs). However, the minima of efficiency are lower and almost the same as for a 300 fs TL pulse (which has the same bandwidth).

The evolution of beam quality depending on GDD for different amounts of TOD is shown figure 3-11. In all cases M^2 is close to 1 at the GDD corresponding to maximal SHG efficiency, then increases and reaches local maxima for positive and negative GDD. While those are reached respectively for $\pm$30 000 fs^2 and $\pm$50 000 fs^2 for 300 fs and 420 fs TL pulses, they are shifted to much larger GDD values (around $\pm$80 000fs^2) in the presence of TOD (positive or negative). Close to GDD= 0fs^2 the dependence on GDD in the presence of TOD is similar to that of a 420fs TL duration pulse, but maximal M^2 values are similar to those for a TL pulse of the same bandwidth (300fs TL duration).
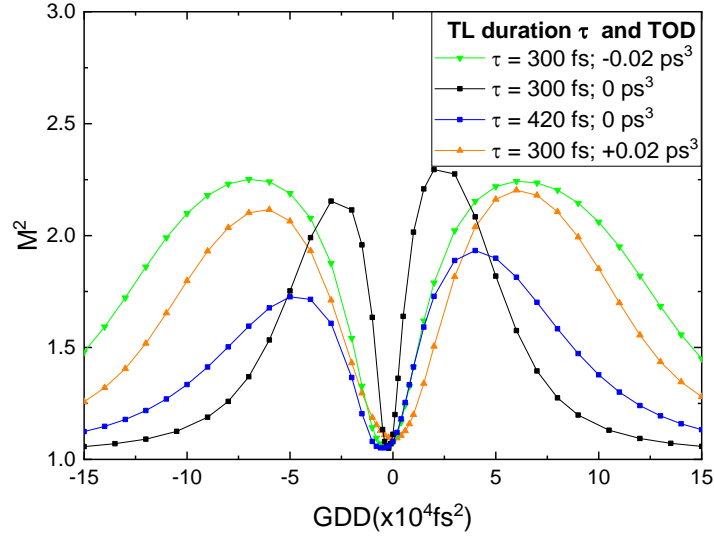
Figure 3-11: Beam quality parameter M^2 of the SH beam as a function of GDD applied to the pulse at the fundamental wavelength for different values of TOD and TBW limited pulse durations. Crystal length is set at 4.8 mm and fundamental radiation peak intensity at GDD = 0 fs^2 was 44.3 GW/cm^2.

Finally, a numerical simulation of SHG with pulses subjected to fourth order spectral phase or, in other words, fourth order dispersion (FOD) was performed. Combined effects of FOD and GDD on SHG were modelled. Initial parameters were the same as in the previous case (with TOD), but a chosen amount of FOD was applied instead of TOD. The value of FOD was chosen so that a temporal pulse quality (Strehl ratio) would be ~90% and the same minimal pulse duration as in TOD case (420fs). FOD can be partly compensated by GDD [206], therefore to make a meaningful comparison a precompensation of FOD with GDD was performed. This precompensation was set at the value corresponding to maximal fundamental radiation peak intensity for a given amount of FOD. The amount of FOD leading to a pulse duration of 420 fs after compensation was $\pm0.025ps^4$. Interestingly, relative Strehl ratio (pulse quality) of pulses stretched by TOD and FOD (after precompensation with GDD) is quite similar (93% and 89% respectively, table 3.5).

τ (fs)	TOD (ps^3)	FOD (ps^4)	t (fs)	ρ (%)	η_{max} (%)	α
300	-0.02	0	420	93	88.3	4.7
300	0	-0.025	420	89	82.9	0.97
300	0	0	300	100	90.9	33
420	0	0	420	100	91.6	4.5
300	0	0.025	420	89	75.8	0.91
300	0.02	0	420	93	84	2.4

Table 3-5: Peak conversion efficiency to the SH for different amounts of TOD or FOD applied to the fundamental pulse of TBW limited pulse duration τ, at 44GW/cm² fundamental radiation peak intensity in a 4.8mm LBO crystal. The ratio ρ of the peak power of the fundamental pulse at GDD=0 to the one for a Gaussian pulse with the same FWHM duration (Strehl ratio) is also provided. SH conversion efficiency sensitivity parameter α on GDD is calculated relative to the sensitivity for a simplified model (depletion and phase effect neglected) for TL pulse duration τ=300fs

The SHG efficiency as a function of GDD when ±0.025 ps^4 of FOD is applied and precompensated with ±0.120 ps^2 of GDD (negative GDD is used for positive FOD and vice versa) to optimize the Strehl ratio of the pulses at the fundamental radiation shown Figure 3.12. Peak SHG efficiency is reduced for both positive and negative FOD but more so for positive FOD. Efficiency dependence becomes asymmetric for positive and negative GDD: for positive FOD, efficiency drops faster for negative GDD, and slower for positive GDD. For positive FOD the situation is reversed. We note that the pulse duration and shape also varies asymmetrically with GDD when some FOD is applied. That could explain the asymmetrical conversion efficiency dependence observed in previous studies [158], [193], [194]. The sensitivity to GDD around the peak of efficiency is significantly reduced (table 3.5), even when compared to a TBW limited pulse of the same duration (420fs).
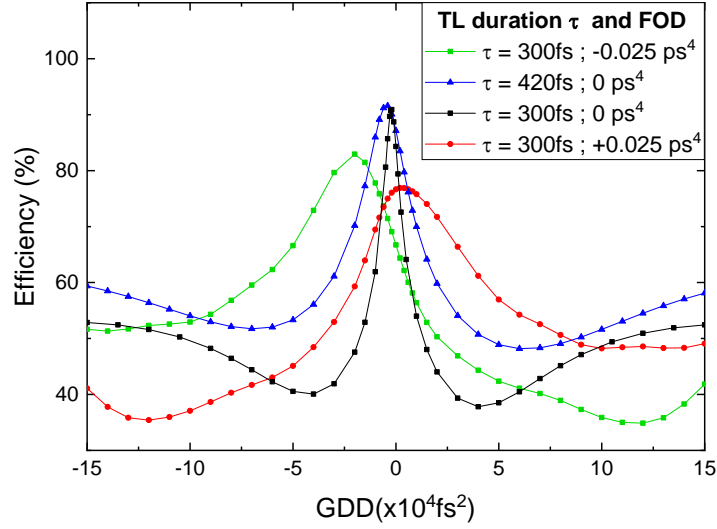
Figure 3-12: Numerical simulation results of efficiency of the energy conversion from fundamental to SH wavelength as a function of GDD applied to fundamental pulses for different values of FOD (also applied to the fundamental pulse). Precompensation was applied when FOD is non zero and GDD=0 fs^2 corresponds to maximal fundamental radiation peak intensity. Crystal length is set at 4.8 mm, transform limited duration at 300 fs and fundamental radiation peak intensity at 44.3 GW/cm^2.

The beam quality evolution is given in figure 3.13. The most notable effect of FOD is introduction of asymmetry in the GDD dependencies. Positive FOD causes a large but asymmetric improvement of M^2 in comparison to a 300fs pulse without FOD when positive GDD is introduced. The value of the M^2 maximum for positive GDD drops from 2.3 to 1.6 (in comparison to a 300 fs pulse with no FOD), while the M^2 maximum value for negative GDD drops from 2.15 to 1.85. For negative FOD the opposite holds. We also notice that the maxima of M^2 correspond to larger amounts of absolute GDD when FOD is introduced. For negative FOD the dependence of both M^2 and SH conversion efficiency on small amounts of positive GDD matches that of a 420 fs TL pulse. The reverse holds for positive FOD.
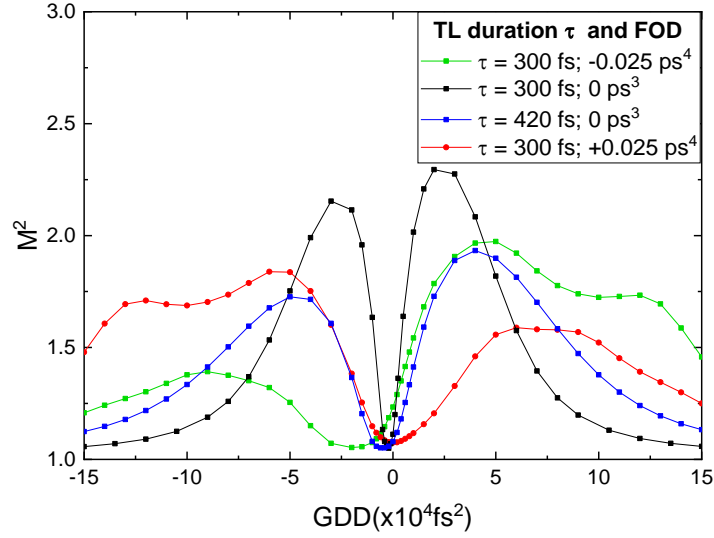
Figure 3-13: Beam quality parameter M^2 of SH as a function of GDD for different values of FOD. Crystal length is set at 4.8 mm, transform limited duration at 300 fs and peak fundamental radiation peak intensity at 44.3 GW/cm^2

3.4 EXPERIMENTAL VALIDATION

In the previous section through numerical simulations the effects of SHG with femtosecond pulses at different set of parameters were explored. We modelled the separate and cumulative effects of different order of spectral dispersion on both: the conversion efficiency from the fundamental to the SH wavelength for femtosecond pulses and the resulting SH beam focusability parameter M^2, which describes the spatial beam properties. However, the ultimate proof of any theoretically obtained results is the experimental evidence. Therefore, we set to validate some of more interesting features of numerical simulations by experiment.

The laser source was an experimental femtosecond fiber laser produced by EKSPLA, delivering pulses with a FWHM duration of 240 fs, with an average power of 3.3 W at 1MHz repetition rate and a central wavelength of 1030nm. A chirped fiber Bragg grating (CFBG) with a linear temperature gradient along the fiber was used in the laser to stretch the pulse [203]. This allowed to add a desired amount of second order dispersion, depending on the temperature gradient. The third and higher order dispersion added by the temperature gradient along the CFBG was negligible in this experiment. At the output of the laser, the pulses were compressed in a diffraction grating compressor. M^2 beam quality parameter of the laser used in experiments was less than 1.1.

The laser beam was focused in the 3.7 mm long LBO crystal, available at the time, down to the diameter of 240 µm to generate second harmonic when the phase matching conditions are met. After separating fundamental and second harmonic radiations, both conversion efficiency and beam quality of SH were measured. As the pulses from the fiber laser were not transformed limited, an exact pulse intensity and phase data were required to compare experimental result and simulation. This characterization was performed with a home built second harmonic FROG (Frequency Resolved optical grating) autocorrelator. The reconstructed pulse and phase of the pulses at the fundamental wavelength used in SHG experiments are shown in figure 3-14.
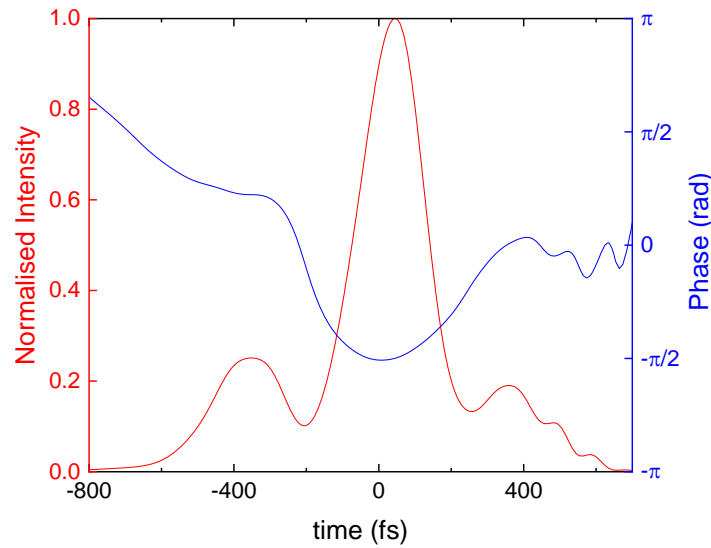
Figure 3-14: Pulse temporal profile of intensity and phase at the fundamental radiation wavelength reconstructed from SH FROG measurement, for the case when temperature gradient on the CFBG was optimized for shortest output pulse duration from the laser

The experiment was performed by varying temperature gradient on CFBG stretcher and measuring second harmonic power using a thermoelectric power meter and performing z-scan measurements of the beam diameter to evaluate M^2 for several GDD values. As was mentioned about fourth order dispersion, even orders of spectral phase can partly compensate each other. Therefore, the GDD=0 fs^2 point was determined using two-photon absorption measurement with a photodiode. It corresponds to the peak of two-photon absorption (which should also correspond to the peak of second harmonic generation when depletion of the fundamental can be neglected, as described in our simplified model).
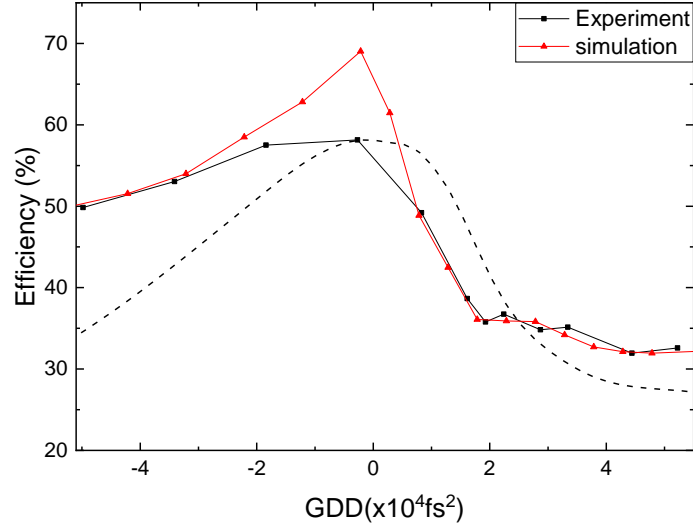
Figure 3-15: Efficiency of SHG as a function of GDD measured with an experimental laser setup in 3.7 mm LBO crystal. The black curve is the values of experimental measurements. The dashed curve is obtained using a simplified model accounting only for the pulse stretching, while neglecting fundamental radiation depletion and phase effects (see section 3.1) The red curve displays the simulation results using phase and amplitude reconstructed from FROG, accounting for 10% optical losses in the system. Simulation was performed without any fitting parameters.

To compare the simulation and experimental results we used the parameters of the FROG reconstructed pulse (figure 3-14). These laser pulses were not Gaussian and the spectral phase could not be approximated by a parabola, which means that the pulses were not only chirped, but also possessed some higher order dispersion. A temperature gradient of the CFBG was set to minimize second order dispersion of the compressed pulse. Varying the temperature gradient allows to add or remove GDD.

The measured SHG efficiency as a function of GDD is given in figure 3-15 (black curve) along with simulated curves. The peak intensity of the fundamental radiation assuming actual pulse shape on the crystal was ~46GW/cm^2. The peak of efficiency was measured around 58%. We observed that efficiency drops sharply for positive GDD but much more slowly for negative GDD, indicating a significant amount of FOD (see figure 3.13). For GDD =30 000 fs^2, efficiency drops to ~35%, while for GDD=-30 000 fs^2 it drops to ~52% only. Part of this asymmetry may be explained by the asymmetric stretching of the pulse for positive and negative GDD. Indeed, the dashed curve, corresponding to the very simplified model presented in section 3.1, also features strong asymmetry. As one can see, the simplified model still does not match well with experiments.

The drop in efficiency for negative GDD is too sharp, while the effect of small amounts of positive GDD (below 10 000 fs^2) is too small, leading to a much smoother efficiency peak. Conversion efficiency from the fundamental to SH wavelength starts dropping sharply for GDD values >10 000 fs^2.
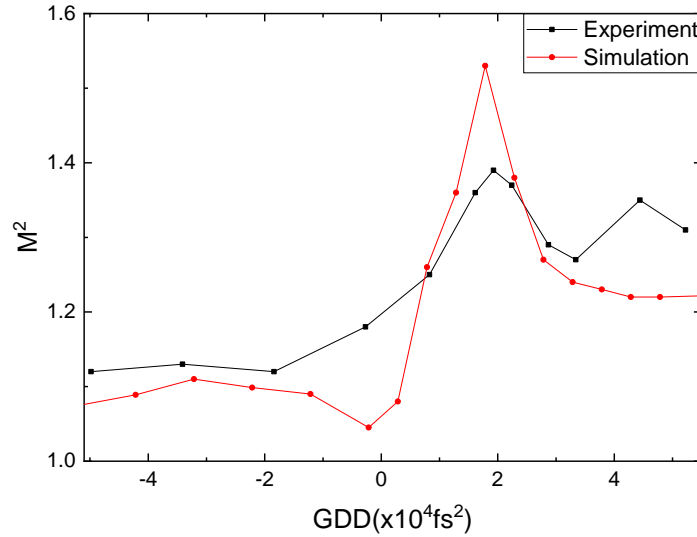
Figure 3-16: M^2 quality parameter of the SH beam generated in a 3.7 mm LBO crystal as a function of GDD. The black curve is the experimental measurement. The red curve displays the simulation result using phase and amplitude reconstructed from FROG.

When a full model numerical simulation was performed taking into account amplitude and phase of the real laser pulses (red curve), the calculated dependence of SHG conversion efficiency on GDD matched the experimental results quite well. The simulated curve displays the same slow decrease of efficiency for large amounts of negative GDD as observed in experiment. It also matches the sharp drop of efficiency for positive GDD. However, even when accounting for losses, it still overestimates the peak efficiency by ~10% and its sharpness. We attribute this to the fact that FROG technique is a very delicate method and the exact intensity and phase profile of the laser pulse may be somewhat different from what was retrieved from FROG data. This difference would obviously influence the modelled SH generation efficiency dependence on GDD in a minor way. Additionally, for the purpose of simulation, we assume the laser beam is Gaussian and its waist located at the front of the LBO crystal. Any experimental deviation from those ideal conditions could affect the SH conversion efficiency dependence on GDD.

The measured dependence of beam quality parameter M^2 on GDD is shown in figure 3-16 (black curve). It is worth noting a sharp rise of M^2 for positive GDD, with a maximum value of 1.4 for GDD around 20 000 fs^2. It corresponds to the same GDD at which sharp drop of SHG conversion efficiency was obtained (figure 3.15). Beam quality then slightly recovers for larger GDD. The beam quality is much better for negative GDD (<1.2 for all experimental GDD values). The dependence of M^2 on GDD variations is fairly well reproduced in simulation, especially the asymmetry with respect to sign of GDD as well as a significant increase of M^2 for positive GDD. This asymmetric dependence of both SH conversion efficiency an SH beam quality parameter on GDD matched the effect of a residual FOD (section 3.4). This could be explained by the fact that dispersion control of the experimental femtosecond laser allowed tuning GDD and TOD, but FOD was fixed by design. On the other hand, nonlinear effects in the fiber amplifier may also lead to higher order phase distortions, which cannot be compensated in the laser system.

3.5 SUMMARY AND CONCLUSION

In this article we presented the results of a study of the effects of GDD and higher order spectral dispersion on frequency doubling in LBO with different set of parameters of fundamental radiation pulses (peak intensity, transform limited duration) and nonlinear crystal length. We demonstrated that at high peak intensity for long crystals, when resulting conversion efficiency to SH is very high (~90%), even relatively small amounts of GDD can have a detrimental effect on SHG conversion efficiency, which can be up to a 100 times larger when compared to low conversion efficiency case. It can cause prohibitive instability of the SH pulses in both short and long term in practical systems, if GDD of the laser system fluctuates or drifts. Reducing the length of the nonlinear crystal helped to mitigate sensitivity to GDD, but then the peak intensity of the pulses needed to be increased to reach a high conversion efficiency and thus, would exceed the damage threshold of the nonlinear crystal surface, making this an impractical approach.

For our knowledge, in this work for the first time the effects of GDD on the SH beam quality at high conversion efficiency regime were systematically studied. In particular, we observed that introducing moderate amount of GDD might considerably degrade SH beam quality, which is very

important and could have practical implications for femtosecond laser systems with tunable pulse duration and SHG.

Numerical simulations of SHG conversion efficiency of transform limited femtosecond pulses with durations in range from 30 fs to 1 ps manifested, that B integral accumulated in the nonlinear crystal is the limiting factor to obtain very high conversion efficiency for the shortest pulses durations. Accumulated nonlinear phase results in significant degradation of the beam quality.

Numerical simulations accounting for higher order spectral dispersion demonstrated that very high conversion efficiency could be obtained with lower sensitivity to non-compensated GDD if a slight degradation of the pulse temporal quality is acceptable. With cubic spectral phase (or TOD), conversion efficiency dependence on GDD is symmetric in respect to the GDD sign. However, introduction of fourth order spectral phase (or FOD) leads to strong asymmetry of SH conversion efficiency and SH beam parameter M^2 in respect to GDD sign.

Finally, experiment with femtosecond fiber laser demonstrated a good agreement between experimental results and numerical simulations, using full intensity and phase information of the laser pulse retrieved from FROG. Asymmetric behavior of SH conversion efficiency and beam quality parameter M^2 was observed for applied positive and negative GDD, which is apparently caused by the uncompensated fourth order dispersion in the laser system or self-phase modulation in the fiber amplifier. This could also explain similar results presented in other studies.

To conclude, a comprehensive set of numerical simulations of SHG of femtosecond pulses showed a rich behavior of conversion efficiency and beam quality of SH in respect to GDD, which was previously not reported in detail.

Chapter 4:
Continuous Compensation of the Phase Mismatch by using Temperature Gradients for Second Harmonic Generation

In the previous chapter, the effect of group delay dispersion on second harmonic generation for nearly compressed pulses was analyzed. Here, we look into a novel parameter that can interact with the group delay dispersion to provide better control of the output. We demonstrate that by applying a temperature gradient along the propagation direction in a long nonlinear crystal, the conversion efficiency and beam quality of the second harmonic of a stretched pulse improves significantly. Furthermore, depending on the sign of both the group delay dispersion and the temperature gradient, the bandwidth and duration of the second harmonic are significantly affected. With a well-chosen temperature gradient, it is possible to reach relatively high conversion efficiency (above 50%) and to compress the second harmonic pulse. Alternatively, it is also possible to maximize the bandwidth of the second harmonic (also at high conversion efficiency), though the pulse will be significantly stretched. A temperature gradient in a bulk nonlinear crystal is a promising transverse parameter, that adds a new degree of freedom in the design of second harmonic generation setups for ultrashort pulses. The effect is similar to chirped quasi-phasematching, but unlike the grating of a periodically polarized crystal it is an easily controlled parameter.

This chapter is based on the article "Continuous Compensation of the Phase Mismatch by using Temperature Gradients for Second Harmonic Generation », in Optic Communications (published online, volume 484, 1st of April 2021), by Pierre-Marc Dansette, Maksim Eremchev and Andrejus Michailovas. The simulation work was performed by Pierre-Marc Dansette. Maksim Eremchev measured the dependence of the conversion efficiency, beam quality and second harmonic spectrum on temperature gradients. Pierre-Marc Dansette performed a second series of experiment including the measurement of the 4th harmonic power, so that all results came from the same setup and laser. The experimental results presented in the article came from Pierre-Marc Dansette. Andrejus Michailovas supervised this project.

4.1 INTRODUCTION

Frequency doubling of an infrared ultrashort laser in a nonlinear crystal is a popular technique[133], [134], [158] to generate visible range radiation due to the lack of good broadband gain media for the visible range. The visible radiation can for instance then be used to pump a parametrical amplifier [140], [187] if broadband tunability is required.

In a typical second harmonic generation (SHG) setup an important first step is to compress the fundamental pulse before it enters the nonlinear crystal. This is achieved by removing dispersion terms, in particular the group delay dispersion (GDD), with a prism compressor or chirped mirrors[207]. Indeed, the transform limited (TL) pulse duration is determined by the spectrum, and nonlinear terms of spectral phase will cause an increase in duration, and thus reduce the efficiency of all nonlinear processes. Furthermore, the dispersion will also affect the temporal phase profile, which has been shown to cause back conversion and thus also significantly affects SHG conversion efficiency[158], [191] as well as the second harmonic beam focusability [157]. Focusability is an important factor for nonlinear microscopy applications for instance[188].Yet this approach can have some drawbacks, as the large sensitivity to GDD at high energy conversion efficiency for nearly transform limited fundamental radiation pulses can cause instability[157], [158], [191]. The pulse duration of the second harmonic will typically be between $\tau/\sqrt{2}$ (at low conversion efficiency) and τ where τ is the input fundamental radiation pulse duration, yet because SH frequency bandwidth can be up to double that of the fundamental radiation, SH pulse durations as short as $\tau/2$ are theoretically possible. One technique allowing high conversion efficiency for second harmonic generation of a stretched fundamental pulse is the use of aperiodic quasi phase-matching (QPM) grating crystals with a linear chirp. Depending on the QPM crystal period chirp, it can be used to generate nearly transform limited SH pulse[123], [208] or to improve the SH bandwidth[124], [209], allowing for shorter pulse duration once the SH pulse is compressed.

The mechanism which take place in the case of chirped QPM should also apply to a linear change of the phase mismatch in the propagation direction. This can be achieved with a temperature gradient in the crystal, as long as the refractive indexes are sufficiently temperature sensitive. Advantageously the temperature gradient can be adjusted on a wide temperature range, while the period chirp of a periodically polarized crystal is fixed, though it can be thermally tuned too [210]. Lithium triborate (LBO), a crystal widely used for SHG and other nonlinear processes, is an ideal

candidate for this application. It can be used for non-critical phase matching. We will investigate the effects of temperature gradients on second harmonic generation with ultrashort pulses.

4.2 NUMERICAL SIMULATION RESULTS

4.2.1 Numerical simulation methods

Numerical simulation is performed with a split-step Fourier method[144]. The effects of temperature changes affect the linear propagation, which is calculated in Fourier space with the full Sellmeier equations of LBO[196]. The formula for linear propagation includes walk-off and paraxial diffraction. Then, the nonlinear mixing is performed in real space, using a fourth order Runge-Kutta method. Cross and self-phase modulation are also accounted for, (with the nonlinear refraction index $n_2 = 2.6x10^{-20}$ m^2/W for LBO)[197].

The fundamental input beam is simulated as Gaussian with $1/e^2$ diameter of 500μm (meaning a Rayleigh length of 760mm). Initial laser parameters : the bandwidth of the fundamental pulse allows for a transform limited (TL) duration of 260fs (full width at half maximum, FWHM), which is typical for passively mode-locked Yb-doped fiber lasers [211]. The spectrum shape is Gaussian and positive or negative temporal chirp is introduced to stretch the pulse to a duration of 900fs. The crystal length is set at 30mm which is rather long for femtosecond pulses, and the crystal is cut at θ=90° and φ=0° corresponding to type I Non-Critical phase matching. The temperature at the center of the crystal is set at the phase matching temperature (here 194°C). A temperature gradient can be applied along the propagation direction, but the central temperature is kept the same.

4.2.2 Results

The refractive index of LBO is strongly dependent on temperature. Therefore, different temperatures will correspond to phasematching for different wavelength. The bandwidth of the pulse is 6nm, and the non-critical phasematching temperature for type I second harmonic generation in LBO will be 198°C at 1027nm, 194°C at 1030nm and 190°C at 1033nm. The phase mismatch Δk between the second harmonic and fundamental radiation is given by:

$$\Delta k = \frac{4\pi}{\lambda_0}\left(n_e\left(\frac{\lambda_0}{2}, T\right) - n_f(\lambda_0, T)\right) \tag{4.1}$$

Where n_e and n_o are the refractive indexes of LBO in the extraordinary and ordinary polarization respectively, λ_0 is the fundamental wavelength and T the temperature. At T=194°C and 1033nm, $\Delta k = -0.083\text{mm}^{-1}$ and at 1027 nm , $\Delta k = 0.083\text{mm}^{-1}$. This means that the maximum crystal length to amplify the whole bandwidth is 19mm. However, applying a temperature gradient in the propagation direction will mean that different wavelength will be phasematched at different point in the crystal. Another important property of the crystal is the group index difference Δn_g between the second harmonic and fundamental radiation. In this case $\Delta n_g = 0.015$, meaning that for a propagation distance of 30mm, the SH and fundamental pulse peaks will be shifted by about 1500fs. However, because new SH photon will be generated near the fundamental peak, the delay between the 2 pulses at the exit of the crystal should be smaller.

We simulated second harmonic generation using models described in [157] with a set of temperature gradients, varying from -1.5K/mm to 1.5K/mm (meaning 45K difference between the front and back of the crystal). The modeled SH energy conversion efficiency is shown Figure 4-1. We observe a symmetrical behavior of SH conversion efficiency with regard to the sign of the temperature gradient, as well as the sign of the chirp. Due to back conversion of the second harmonic radiation to the fundamental wavelength in the long nonlinear crystal, the efficiency is low when there is no gradient. When a temperature gradient is introduced, it improves and reaches maxima for positive or negative temperature gradients, before slowly decreasing towards 0%. The maximum conversion efficiency increases with the intensity of the fundamental beam, and the peak of conversion efficiency is reached for slightly larger temperature gradients when the intensity of the fundamental is higher. The temperature gradient corresponding to maximum conversion efficiency at 0.5GW/cm^2 is ±0.4 K/mm, corresponding to 200°C and 188°C at the front or back of the crystal (depending on the sign). This is slightly more than the phasematching temperature for 1033nm and 1027nm, which is not necessarily surprising as 6nm is the full width at half maximum (FWHM) of the spectrum, and there is still some energy out of this wavelength range. When the temperature gradient is larger, there is no phasematched wavelength at the front and end of the crystal, so the crystal length is effectively reduced. Using an appropriate temperature

gradient it is possible to increase conversion up to three times in comparison with a constant temperature in the crystal.
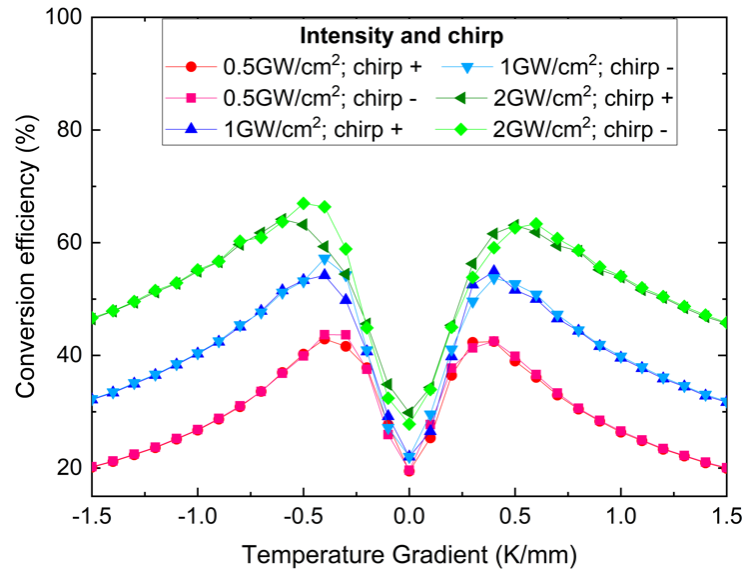
Figure 4-1: Modeled SH energy conversion efficiency dependence on the temperature gradient in a 30 mm long LBO crystal for different peak intensities of the fundamental radiation, as well as different signs of the initial chirp (250 fs TL pulse stretched to 900fs).

We expect to observe a strong deterioration of the beam profile when there is back conversion. The SH beam quality parameter M^2 [157], [212] variations with temperature gradients in the crystal are shown Figure 4.2. M^2 is maximal (meaning the spatial properties of the beam are bad) for a constant temperature in the crystal (no temperature gradient) and improves for increasing temperature gradients. Once again the behavior of M^2 is mostly symmetrical in respect to the sign of both the temperature gradient and the chirp, except for the highest modeled fundamental radiation intensity of 2.5GW/cm^2, where the peak of M^2 is significantly worse for a negative chirp than for a positive one. For increasing temperature gradients, M^2 tends towards unity value, meaning a perfect gaussian beam. While from Figure 4.1 we observed that increasing the fundamental radiation peak intensity also increases the value of the maxima of efficiency, the beam quality also worsens. The ~55% peak SH conversion efficiency at 1GW/cm^2 corresponds to M^2~1.4 which is already relatively high, and the 66% peak SH conversion efficiency at 2.5GW/cm^2 corresponds to M^2~1.7, which would be prohibitive for microscopy applications for instance. A compromise between the SH conversion efficiency and the beam quality needs to be found.
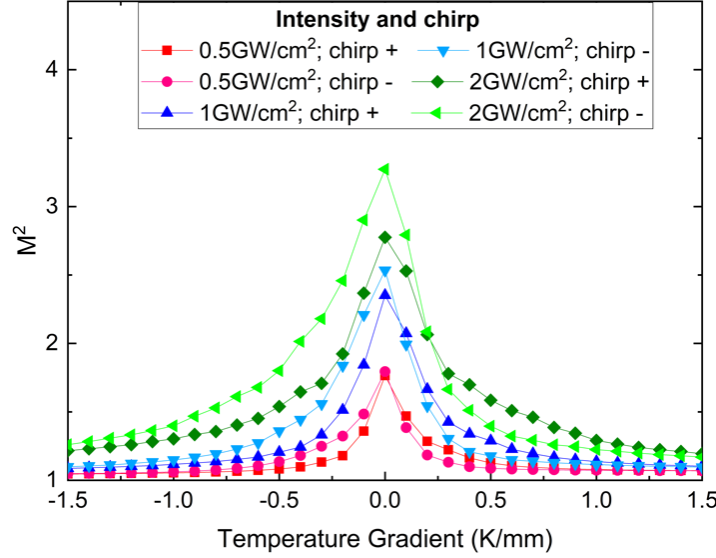
Figure 4-2: Modeled SH beam quality parameter M^2 dependence on the temperature gradient in the LBO crystal for different peak intensities of the fundamental radiation, as well as different signs of the initial chirp (250 fs TL pulse stretched to 900fs).

The FWHM pulse duration of the second harmonic radiation as a function of temperature gradient is plotted figure 4.3, also for different fundamental radiation peak intensities. This is the duration of the SH pulse jut after the LBO crystal without any compression. Unlike the SH conversion efficiency or the beam quality parameter M^2, the pulse duration depends asymmetrically the sign of the temperature gradients but, applying a positive chirp and temperature gradient is the same as applying a negative chirp and temperature gradient. For a positive chirp and a positive gradient, the SH pulse duration is reduced compared to a situation with no gradient. It reaches a minimum for temperature gradients around 0.4 K/mm. For higher temperature gradients the duration slowly increases and tends to reach a plateau around 500fs. When chirp is positive and a negative temperature gradient is applied, the SH pulse can become much longer than in the absence of a temperature gradient. Maximum pulse duration of 2.2 ps is reached for a temperature gradient -0.4 K/mm. For larger negative temperature gradients the SH pulse duration decreases. The SH pulse duration is mostly independent on the peak intensity of the fundamental radiation. We can also notice some sharp variations of the SH duration for large temperature gradients. Here the pulse duration is defined as the FWHM of the pulse, but for some temperature gradients the SH pulse presents several not fully separated small peaks. When the position and amplitude of those peaks changes it can cause a sharp change of pulse duration. For 2GW/cm^2 fundamental intensity, self and cross phase modulation tends to smooth those peaks.
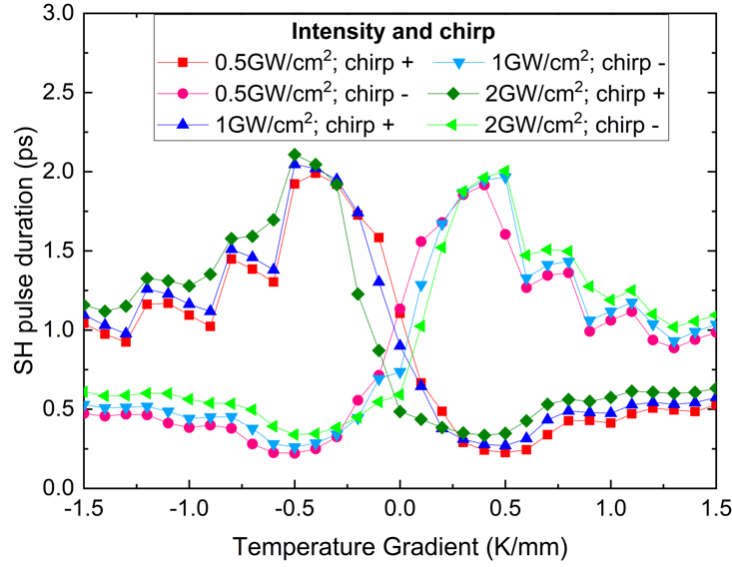
Figure 4-3: Modeled SH pulse duration at the output of the LBO crystal dependence on the temperature gradient for different peak intensities of the fundamental radiation as well as different signs of the chirp (250 fs TL pulse stretched to 900fs).

The dependence of the SH pulse duration on the temperature gradient can be qualitatively understood. For a positive temperature gradient, the temperature at the front of the crystal corresponds to a longer wavelength. The SH is slower than the fundamental radiation (due to the group index difference). When the fundamental is positively chirped, the longer wavelengths are shifted towards the leading edge of the pulse. Because they are converted first, the SH peak starts in front of the fundamental pulse. As both pulses propagate in the crystal, the fundamental catches up, and the wavelength that correspond to $\Delta k = 0$ are located later in the fundamental pulse. Thus, for a certain temperature gradient, the peak of SH will be superposed with the section of the fundamental pulse that is phasematched, so the conversion will be particularly efficient and the SH pulse will remain short. In this case for a 0.5K/mm temperature gradient, there will be 16mm between where the temperature is 190°C and where it is 198°C (phasematching for 1033nm and 1027nm). The group index difference means the SH will be delayed by 800fs over that distance, which is almost the same as the pulse duration. It is lucky that the temperature gradient that allows for good compression of the SH also corresponds to the peak of conversion efficiency.

On the other end, for a negative temperature gradient, the conversion will start with the tailing edge of the fundamental pulse, and the SH being slower, new SH photon will always be generated in front of the current SH pulse. There cannot be efficient back conversion because the fundamental pulse will always be in front of the SH. The SH pulse will be extremely long as the delay due to group velocity mismatch (GVM) is added to the fundamental duration. Indeed, without a group velocity mismatch the SH pulse duration is $\sqrt{2}$ times shorter than the fundamental duration in the low conversion efficiency approximation, and if we add the delay of 1.5ps due to GVM, we can predict a 2.1ps SH pulse duration, which is the same as in figure 4.3. Admittedly, the low conversion efficiency approximation should not be valid in this case. For larger temperature gradients, we mentioned before that the crystal length is effectively reduced for SH generation, as the front and back end have very little effect. Therefore, delay between SH and fundamental gets smaller and the SH duration is shorter. When the sign of both the temperature gradient and chirp is changed, the situation is reversed, which we also observe in simulations. What is more surprising is that the conversion efficiency and beam quality are the same for a positive or negative chirp, because the mechanism is very different.

In many practical cases a compressor (using prisms or gratings) is built after the nonlinear crystal to compress as much as possible the SH pulse. Most compressors only compensate for GDD (second order spectral phase in a Taylor expansion), though it is possible to also compensate for higher dispersion terms (higher order spectral phase terms) such as third[213] or even fourth order dispersion[214]. Here we simply calculated the Fourier transform of the SH pulse spectrum and measured its FWHM duration. This is the theoretical minimum for the pulse duration, when all dispersion terms have been compensated. The evolution of this transform limited (TL) pulse duration with temperature gradients in the crystal is shown Figure 4.4. The dependence of TL pulse duration on temperature gradient is completely asymmetrical with regard to the sign of the temperature gradient, but a negative chirp and temperature gradient has the same effect as a positive chirp and temperature gradient. For a positive chirp, the TL pulse duration increases for positive temperature gradients and reaches a peak at 0.4K/mm, before decreasing and reaching a plateau around 230 fs. Interestingly at 0.4 K/mm and for a fundamental peak intensity of 1 GW/cm^2 the SH pulse is almost perfectly compressed: the pulse duration is 281fs and the TL duration is

277fs. When a negative temperature gradient is applied to the crystal (still for a positive chirp), the SH TL pulse duration decreases and reaches a minimum at 0.8 K/mm. It then slowly rises for larger negative temperature gradients. The higher the fundamental radiation peak intensity, the lower this minimum TL duration. At 2.5 GW/cm^2 intensity the SH TL duration can be as low as 140 fs. The theoretical minimum for the SH TL pulse duration is 125fs, because the bandwidth in frequency can be up to double that of the fundamental.
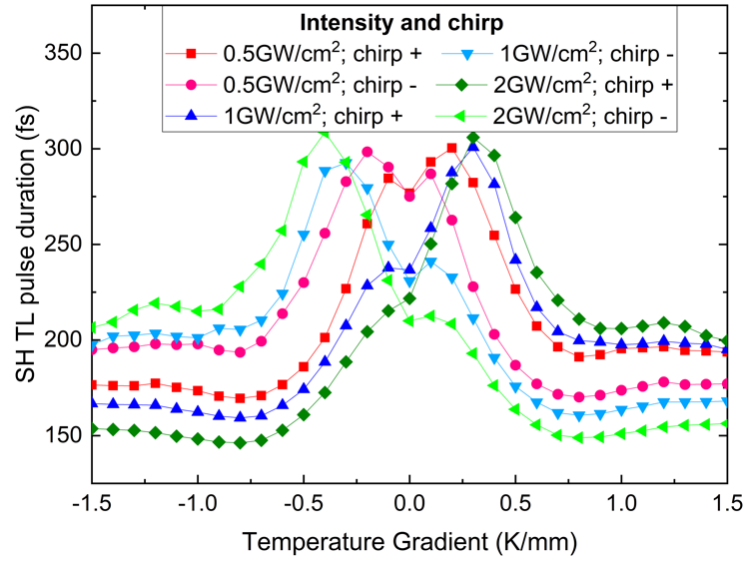
Figure 4-4: Calculated SH transform limited (TL) pulse duration dependence on the temperature gradient in the LBO crystal for different peak intensities of the fundamental radiation.

The effect of temperature gradient on SH bandwidth can also be explained qualitatively. In the case of a positive gradient and a negative chirp, the SH is always tailing the fundamental. Because the different spectral component are separated in time, they never interact with each other. Each spectral component is frequently doubled and conversion efficiency is high, so the SH bandwidth is nearly double that of the fundamental. On the other end, for a positive chirp the phasematching and the SH peak can temporally overlap for a temperature gradient of ~0.5K/mm. This means that conversion efficiency will be particularly high for wavelength that are already present in the SH pulse, and is what likely leads to a shorter SH bandwidth.

We have now thoroughly investigated the effect of SHG in an LBO crystal with applied temperature gradients for a given value of the fundamental TL pulse duration (250fs), when the pulse is stretched 3.6 times (to 900fs). Would the effect be the same when the bandwidth is wider

or narrower (meaning when the Transform limited duration is resp. shorter or longer), or when different amounts of stretching are applied? The modeled SHG conversion efficiency for different values of the fundamental pulse duration is shown figure 4.5 on the left, and the effect of more or less stretching on the right. The larger the bandwidth (so the shorter the TL duration), the larger the temperature gradient required to maximize the conversion efficiency. For a given temperature there is phasematching is realized for a certain wavelength, thus, this is not surprising, as a large temperature gradient means a larger range of wavelength for which there will be phasematching realized within the crystal length. The peak of conversion efficiency decreases for large bandwidth but still remains above 40% even for a 100fs TL pulse duration of the fundamental radiation. A 100fs TL pulse duration corresponds to a 16nm bandwidth (for a Gaussian spectrum). The phasematching temperatures for 1038nm and 1022nm frequency doubling are respectively 183°C and 205°C. To have these temperatures at the front and back end of the crystal we need a ±0.7K/mm, very close to where the peaks of conversion efficiency are observed (±0.8K/mm). When the fundamental TL duration is kept the same but different amounts of chirp are applied (figure 4.5 right), there almost no effect on the peak of efficiency or asymptotic behavior unless there is no chirp at all (TL pulse). For a TL pulse we have a higher conversion efficiency without any gradient. However, the conversion efficiency and beam quality might become much more sensitive to small amounts of dispersion[157]. The effect of the temperature gradient on M^2 is not shown here, as there is no significative change compared to figure 4.2: There is always a peak of M^2 when there is no temperature gradient and it improves when a temperature gradient is introduced. The only exception is when the pulse is transform limited, in which case M^2 is always good (smaller than 1.2). We note that the peak of efficiency for a fundamental radiation with 100fs TL pulse duration (stretched to 360fs) corresponds to $M^2\sim1.1$. Thus, the intensity of the fundamental beam could be increased to get a higher conversion efficiency (like in figure 4.1) while keeping good beam quality.
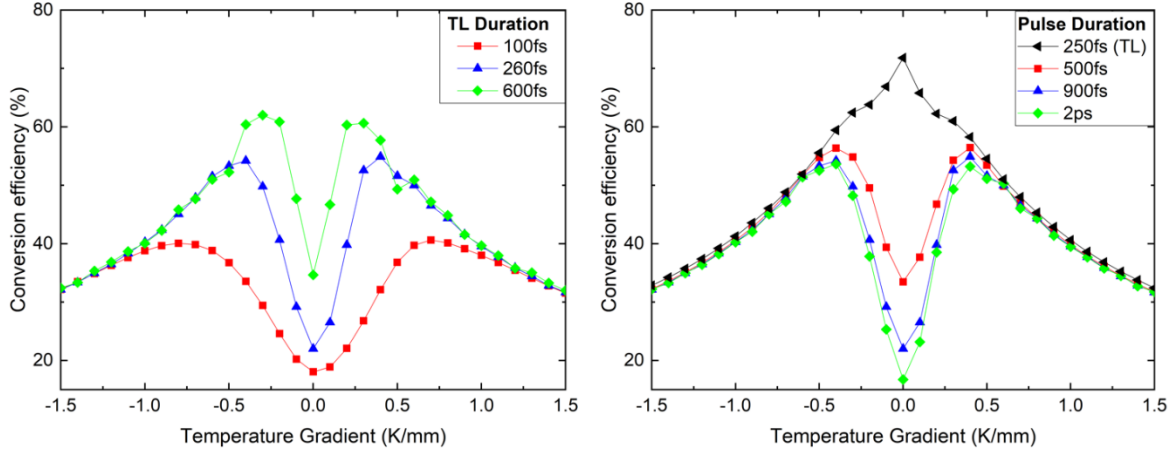
Figure 4-5: Modeled SH energy conversion efficiency dependence on the temperature gradient in a 30 mm long LBO crystal for 1GW/cm² intensity of the fundamental radiation. On the left, several pulse durations of the fundamental radiation are modeled for the same amount of relative stretching (3.6 times) using positive chirp. On the right, the TL duration of the fundamental pulse is 250fs and different amounts of positive chirp are applied in order to stretch the fundamental pulse.

In figure 4-6, we show the effect of the fundamental TL duration (left) and of the amount of chirping (right). When a negative temperature gradient is introduced the pulse duration tends to increase. For larger values of the fundamental TL duration (left) or of the stretching (right), the peak gets higher. For different values of the fundamental TL duration, the peak of efficiency for positive chirp corresponds to a shorter pulse duration than the one for negative chirp. Unfortunately, the maximum compression is not necessarily observed at the peak of efficiency. On the right we see that the amount of stretching affects the position of the shortest pulse duration. Therefore, using a temperature gradient to compress the SH pulse will work well only for certain values of the stretch. Using a different crystal length might be necessary for different amounts of dispersion. As we mentioned earlier, the temperature gradient that leads to a compressed pulse also corresponded to maximum conversion efficiency for a 260fs stretched to 900fs, but this is not necessarily the case. We deduced that the maximum SH pulse duration $\tau_{SH\ max}$ should be:

$$\tau_{SH\ max} = \frac{\tau_f}{\sqrt{2}} + \frac{\Delta n_g L}{c} \qquad (4.2)$$

Where τ_f is the pulse duration of the fundamental radiation, L is the crystal length and c the speed of light in vacuum. We already calculated that the delay due to GVM is 1500fs. This formula is

relatively well verified for all considered fundamental durations and TL duration, except when there is no chirp.
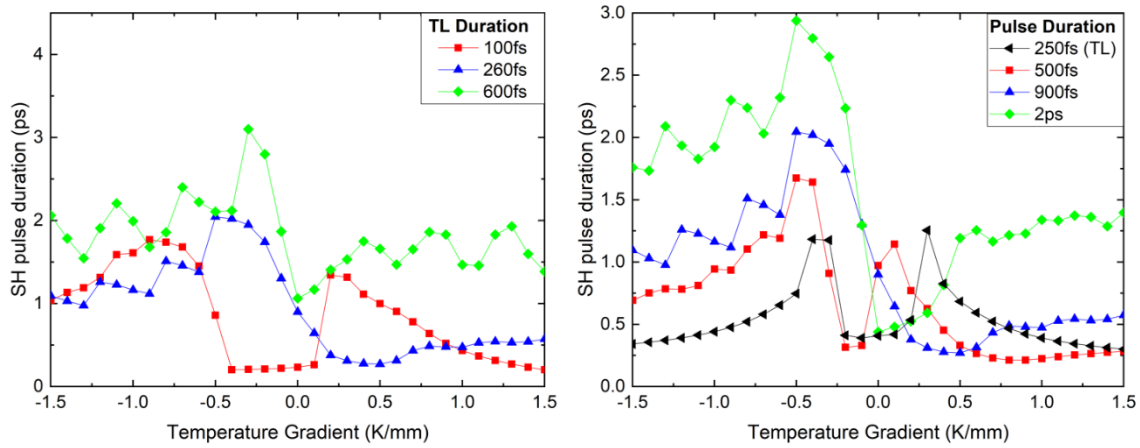
Figure 4-6: Modeled SH pulse duration dependence on the temperature gradient in a 30 mm long LBO crystal for 1GW/cm² intensity of the fundamental radiation. On the left, several pulse durations of the fundamental radiation are modeled for the same amount of relative stretching (3.6 times) using positive chirp. On the right, the TL duration of the fundamental pulse is 250fs and different amounts of positive chirp are applied in order to stretch the fundamental pulse.

Finally, the TL duration of the SH pulse dependence of temperature gradient was modelled for different values of the fundamental duration (Figure 4.7, left) and different amounts of stretching (Figure 4.7, right). For pulses with a large bandwidth (100fs TL duration) the dependence becomes more symmetrical, but in all cases the peak of efficiency for a negative temperature gradient corresponds to a shorter SH TL duration than the one for positive temperature gradients. When the fundamental bandwidth remains the same but the amount of chirp changes (right), the peak of SH TL duration is affected. We also observe that while having a TL fundamental lets us reach a higher conversion efficiency (figure 4.5), the bandwidth of the SH will be much shorter (450fs TL duration). The effect of negative temperature gradients on the SH TL duration is mostly unaffected by the amount of positive chirp.
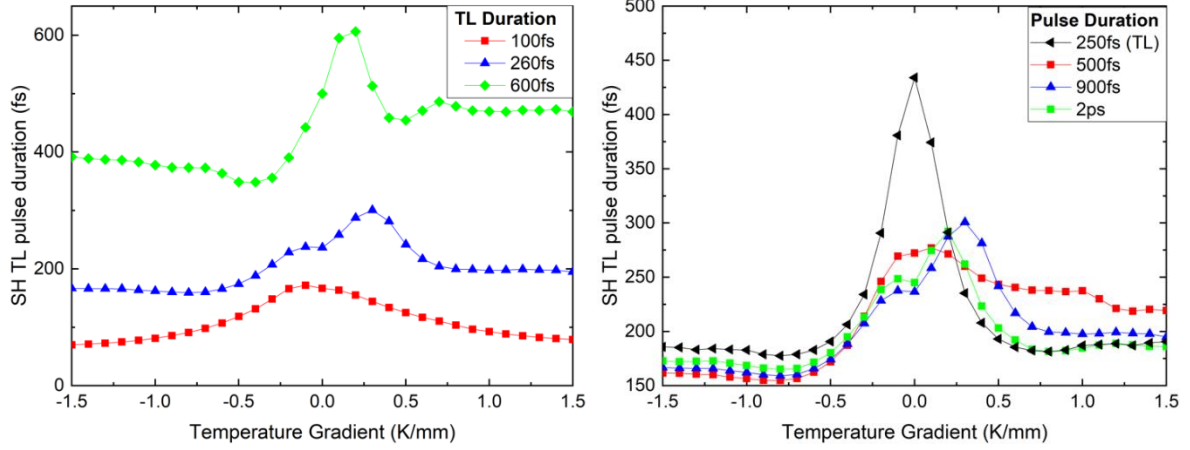
Figure 4-7: Modeled SH TL duration dependence on the temperature gradient in a 30 mm long LBO crystal for 1GW/cm² intensity of the fundamental radiation. On the left, several pulse durations of the fundamental radiation are modeled for the same amount of relative stretching (3.6 times) using positive chirp. On the right, the TL duration of the fundamental pulse is 250fs and different amounts of positive chirp are applied in order to stretch the fundamental pulse.

4.3 EXPERIMENTAL RESULTS

In the previous section we simulated the effect of temperature gradients in LBO for SHG. For well-chosen temperature gradients we observed not only a large improvement of both the energy conversion efficiency to SH and the SH beam quality, but also reduction of either the SH pulse duration or of the TL pulse duration. We now proceeded to perform experimental measurements to confirm simulation results. Indeed, when using imperfectly Gaussian pulses and beams, as well as more complex phase profiles.

4.3.1 Experimental setup

We used a Femtolux 3 (Ekspla Ltd.) femtosecond Yb doped fiber laser with a TL pulse duration of 260fs and central wavelength of 1030nm as the fundamental radiation. A chirped fiber Bragg grating with temperature gradient imposed any desired amount of GDD on the fundamental radiation (positive or negative)[203]. The frequency doubling was performed in an LBO crystal of 30 mm (as in simulation) placed in a specifically designed oven[215] that could impose two different temperatures on the front and back end of the crystal, thus creating any desired

temperature gradients. However, the design of the oven imposed a higher temperature at the back end than at the front end. Without rotating the oven (and changing the crystal position) it was not possible to impose negative temperature gradients. We could also not impose temperature gradients higher than 1.2 K/mm (which according to simulation was a large enough range: Figure 4.1-4.4). Instead of rotating the oven we chose to stretch the fundamental radiation with positive or negative chirp alternatively, as simulation showed that using a negative chirp with a positive temperature gradient was equivalent to using a negative temperature gradient with a positive chirp. Furthermore, a second set of measurements where the oven was rotated so the temperature gradients were negative was also performed and confirmed this tendency. The fundamental radiation pulse was stretched to 900 fs as in simulation. The fundamental radiation beam diameter at the crystal was 500 µm ($1/e^2$ diameter) with a beam quality parameter $M^2\sim1.1$.

We performed measurement of the power of the SH beam (and so the energy conversion efficiency), the spectrum of the SH and the beam quality parameter M^2 by performing a Z-scan on the SH beam. The spectrum of the SH was used to calculate a TL SH pulse duration by performing a Fourier transform. We also measured fourth harmonic conversion efficiency (frequency doubling of the SH pulse) in a low efficiency setting. This allows us to evaluate the SH pulse duration.

4.3.2   Experimental results

The measured SH energy conversion efficiency as a function of temperature gradient is shown Figure 4.8 for two different fundamental peak intensities. Like in simulation the application of a temperature gradient improves conversion efficiency up to a maximum. As expected, the behavior of SH conversion efficiency is very similar for positive or negative temporal chirp. The peak of conversion efficiency is observed at slightly higher values of the temperature gradient for negative chirp. At 2GW/cm^2 fundamental radiation peak intensity, peak conversion efficiency is ~55% for either positive or negative temporal chirp. At 1GW/cm^2, peak conversion efficiency is slightly higher for positive chirp (48%) than for negative chirp (45%). Those results are similar to simulation, even if the peak conversion efficiency is observed for stronger temperature gradients and is slightly lower.
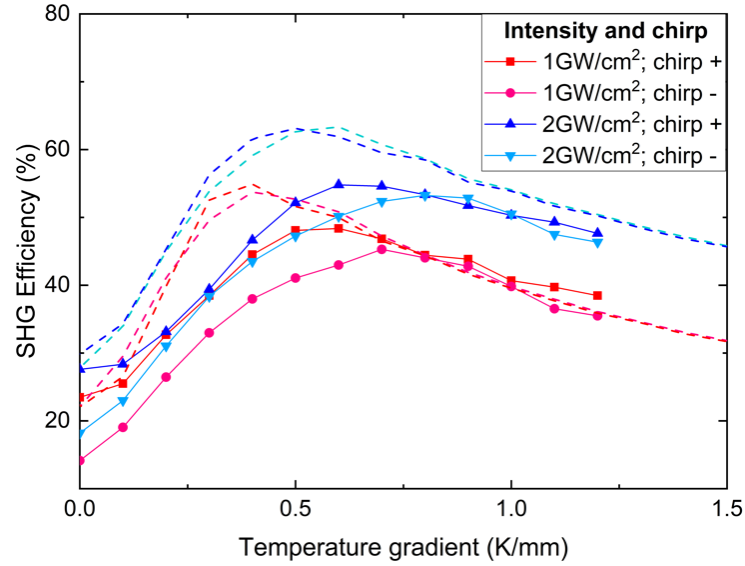
Figure 4-8: Measured SH conversion efficiency dependence on the temperature gradient in the LBO crystal for different peak intensities of the fundamental radiation as well as different signs of the chirp parameter. Dashed curves are the simulation results for the same parameters.

The variations of the beam quality parameter M^2 of the SH (measured by Z-scan) with temperature gradients are plotted Figure 4.9. M^2 improves with increasing temperature gradients and is slightly better for negative than for positive chirp. It is very high when no temperature gradients is applied. At $1GW/cm^2$ M^2 drops below 1.5 for positive temporal chirp and 1.25 for negative temporal chirp for the temperature gradients that maximize the energy conversion efficiency (Figure 4.5). At $2GW/cm^2$ and with a positive chirp M^2 remains too high: the maximum of efficiency corresponds to $M^2\sim1.8$. While operating at higher intensity of the fundamental radiation is tempting because it improves conversion efficiency, it would be impractical for applications requiring higher beam quality. There is a very good match between simulation and experimental results, though the measured M^2 at $2GW/cm^2$ remains higher, possibly because the fundamental beam is not perfectly gaussian.
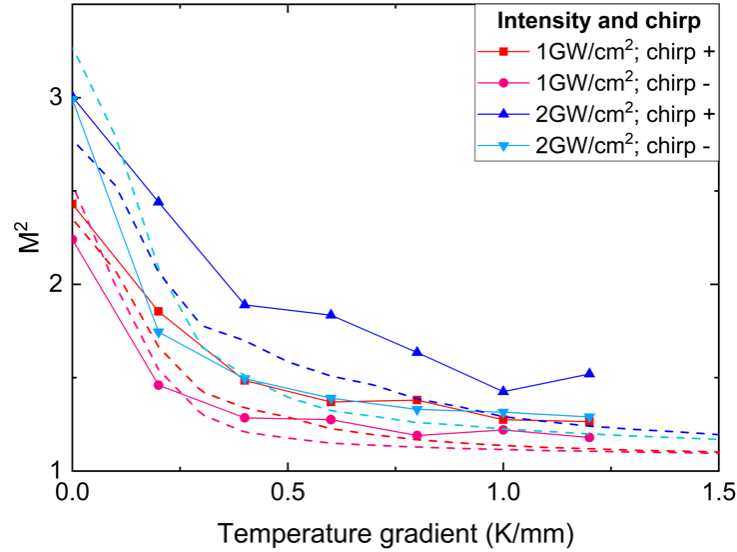
Figure 4-9: SH beam quality parameter M^2, measured by Z-scan, dependence on the temperature gradient in the LBO crystal for different peak intensities of the fundamental radiation. Dashed curves are the simulation results for the same parameters.

Next, we measured the SH spectrum. By performing a Fourier transform we can get a TL duration of the SH pulse. However, this duration might be difficult to achieve in practice, if there are accumulated large high order spectral dispersion terms (third order or higher). The dependence of this calculated TL SH duration on temperature gradients in the LBO crystal is shown Figure 4.10. The TL SH duration is shorter at 2GW/cm^2 fundamental radiation intensity than at the lower intensity of 1GW/cm^2. This might be in part due to self and cross phase modulation. For negative temporal chirp the TL duration decreases for increasing temperature gradients and seems to reach a plateau around 170 fs at 1GW/cm^2 and 150fs at 2GW/cm^2. For positive temperature gradients the TL duration slightly increases in comparison with a constant temperature in the crystal. At 1GW/cm^2 the SH TL duration is almost constant at ~300fs for temperature gradients between 0 and 0.8 K/mm, and then becomes longer. At 2GW/cm^2 it is much shorter, between 200 and 240fs. Like in simulation a positive temperature gradient with a positively chirped fundamental pulse results in a longer TL pulse duration, while a negatively chirped pulse with a positive gradient (which is equivalent to a negative gradient with a positively chirped pulse) results in a shortening of the SH TL duration. The measured TL pulse duration closely matches simulation results for negatively chirped pulses, but there is far more difference for positively chirped ones. The SH TL duration seems mostly independent of the temperature gradient and starts increasing for large gradients. In section 2, we described how for a specific temperature gradient the peak of the SH

would overlap in time the section of the fundamental pulse that was phasematched. Because of this there could be back conversion of the SH, different spectral components of the fundamental could interact, which can lead to a shorter SH bandwidth. This is a complex phenomenon, and the way it would be affected by a change in the fundamental spectrum or spectral phase is unknown. However, for a negative chirp, the SH is mostly temporally separated from the fundamental where there is phasematching, so there should be much less interaction after the initial conversion.
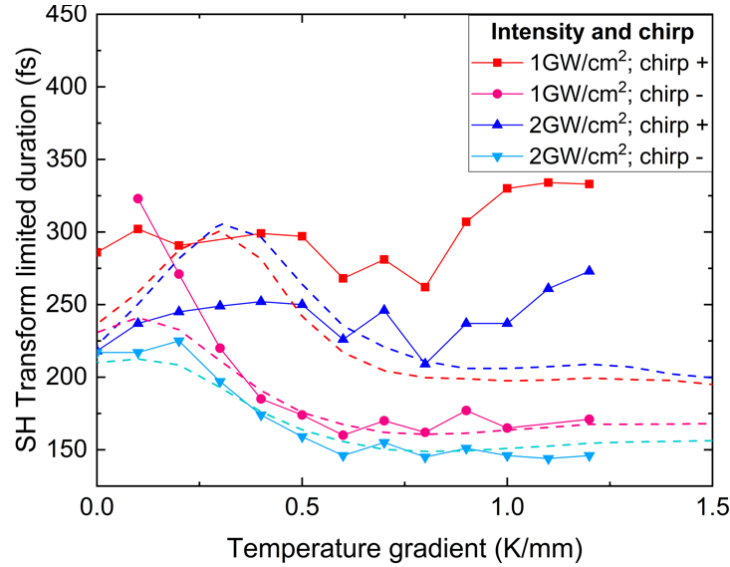
Figure 4-10: Calculated SH transform limited (TL) duration dependence on the temperature gradient in the LBO crystal for different peak intensities of the fundamental radiation. TL duration was calculated using the measured spectrum of the second harmonic radiation. Dashed curves are the simulation results for the same parameters.

The evaluation of the actual pulse duration is a more complex problem. Frequency resolved optical gating (FROG [183]) could be used to reconstruct the pulse. Alternatively, the autocorrelation trace provides an estimate of the pulse duration as long as the pulse is mostly gaussian. However, at 257nm (the wavelength of the fourth harmonic), we had no equipment available to perform these measurements. One of the main applications of ultrashort pulses is for nonlinear phenomena, as they are highly intensity dependent. Thus, measuring the efficiency of a nonlinear phenomenon also informs us on the pulse duration. From simulation results it appears the pulse shape can become non-Gaussian depending on the temperature gradient applied. Here we simply used a 2mm BBO crystal in order to frequency double our SH pulse. The acceptance bandwidth of for this crystal is 0.7nm, which is unfortunately shorter than the bandwidth of the bandwidth of the SH. In

the low efficiency approximation, the relationship between the fourth harmonic generation conversion efficiency η_{4H} and the SH pulse duration is given by:

$$\eta_{4H} = \alpha \frac{E_{SH}}{\tau_{SH}} * p \qquad (4.3)$$

Where E_{SH} is the energy of the SH pulse, p coefficient to account for the limited acceptance bandwidth of the crystal and α depends on the crystal properties, the geometry and the beam diameter. The coefficient p was calculated by dividing the integral of the squared SH spectrum over the acceptance bandwidth of the crystal and dividing by the integral over the whole SH bandwidth. Indeed, within the low conversion efficiency approximation, the spectrum of the frequency doubled radiation is the spectrum of the fundamental radiation squared. Thus, to retrieve the SH pulse duration we need to calculate the proportionality coefficient α. To do this we generated SH with a much shorter LBO crystal of 2mm (without any temperature gradient), leading to low efficiency conversion. Here the acceptance bandwidth is quite large (33 nm), so we don't need a coefficient p. Since the fundamental pulse can be considered Gaussian, the SH pulse duration can be estimated as $\tau_f/\sqrt{2}$ where τ_f is the duration of the fundamental pulse (260fs). Similarly, we estimated the bandwidth of the SH and used it to calculate the coefficient p for this reference pulse. We then frequency doubled this SH pulse and measured the fourth harmonic power (the pulse energy multiplied by the repetition rate). Knowing the SH pulse duration along with the second and fourth harmonic powers (and so the SH pulse energy E_{SH} and the conversion efficiency η_{4H}), we calculated α. Finally, we replaced the 2mm LBO crystal with our 30mm crystal and measured the second and fourth harmonic power for a set of temperature gradients. Because the geometry didn't change, the coefficient α is still the same, and we calculated the SH pulse duration with equation 3.
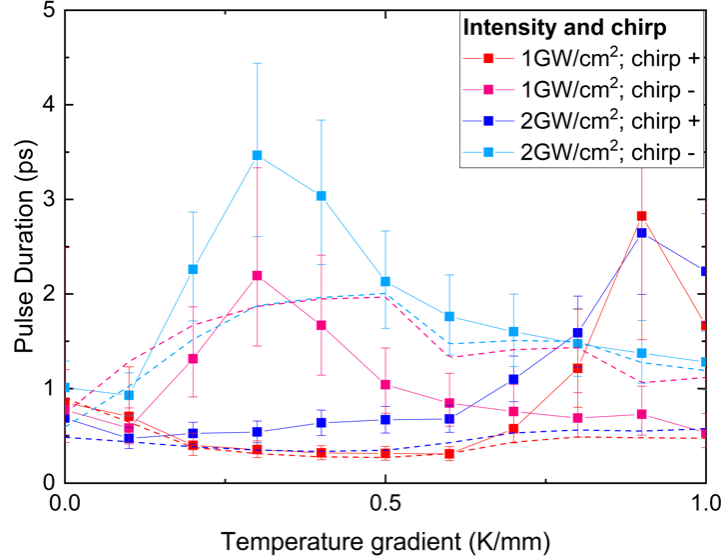
Figure 4-11: Calculated SH duration dependence on the temperature gradient in the LBO crystal for different peak intensities of the fundamental radiation. The duration was calculated by using low conversion efficiency approximation (see above)

The calculated SH duration is shown figure 4.11. An error bar was estimated for this measurement. First, we assume that there is a +/- 20% uncertainty on the value of the alpha coefficient (equation 3). The proportionality relationship is valid only when 4th harmonic conversion efficiency is low (in our case it was always less than 10%), and the method used to evaluate α also has some inherent uncertainty, in part because the acceptance bandwidth of the BBO crystal is so short. The second source of uncertainty is the measurement of the 4th harmonic power, which lets us retrieve the 4th harmonic pulse energy (repetition rate is 1MHz). Here we estimated a measurement error of 0.2 mW. This matters little when the 4th harmonic power is high (a few tens of mW), meaning when the pulse duration is short. When the 4th harmonic power is low (around 1mW), meaning the SH duration is long, this means a larger error window. Nevertheless, the calculated SH duration follows the expected behavior from simulation. When the chirp is positive, duration drops for a positive temperature gradient, and the pulse is relatively well compressed. At 1GW/cm^2 the pulse duration drops to ~280fs (+/- 35fs) for a 0.5K/mm temperature gradient. When the chirp is negative the pulse can become extremely stretched (several ps), but from figure 4.10 we know this corresponds to a large bandwidth. The experimentally calculated SH durations at 1GW/cm^2 are extremely similar to the SH pulse duration from simulations. At higher intensity of the fundamental radiation, there is a much larger divergence between simulation and experiments, which can mean an increasing influence of multiphoton processes on SH generation.

Experimental results match relatively well with the simulation results for conversion efficiency and beam quality. There is more difference for the pulse duration and bandwidth of the SH, though the experimental behavior is qualitatively reproduced. There are multiple possible source of error: The simulation assumes a Gaussian spectrum and no high order dispersion of the fundamental pulse, which is not necessarily completely true especially. In our case the chirped pulses are obtained by detuning a chirped fiber Bragg grating [203], which can lead to some higher order dispersion. The simulation also doesn't include two photon absorption, which can lead to loss of SH power as well as modify the temperature profile in the crystal.

4.4 CONCLUSION

In this work we analyzed the effect of a temperature gradient for frequency doubling of a chirped IR femtosecond pulse in an LBO crystal. We first performed a numerical simulation of this effect, which showed how a temperature gradient in LBO can affect the SH radiation properties. In this study we present the results of frequency doubling of a chirped near IR femtosecond pulse in an LBO crystal with a temperature gradient. Globally we can distinguish two interesting situations depending on the objectives. On the one hand if we seek to avoid using a compressor before or after the nonlinear crystal, we can apply a positive temperature gradient and the SH pulse should be well compressed at the output. On the other hand, if our objective is to increase the SH bandwidth, and thus to compress the SH pulse to shorter duration, it is better to apply a negative temperature gradient. The resulting TL duration of the SH should be almost half that of the fundamental, the theoretical minimum. In both cases this can be achieved while enhancing the SH conversion efficiency and maintaining a good beam spatial profile. The results should apply to a relatively large range of chirps and fundamental bandwidth, though the crystal length might need to be selected to allow a better match between the minima of duration and TL duration with the maximum of conversion efficiency. This technique seems particularly well adapted when the fundamental bandwidth is large (100fs TL duration and shorter), as the sensitivity to the temperature gradient is low for the conversion efficiency, and an even larger bandwidth can be obtained for the SH.

Secondly, we performed experimental measurements to verify the predictions from simulation. The expected improvements of SH energy conversion efficiency and SH beam quality where observed, as well as the lengthening and shortening of SH TL duration for positive and negatively chirped fundamental pulses respectively (for positive temperature gradients) and the reverse effect for the SH pulse duration.

The use of bulk nonlinear crystals with a temperature gradient, which generates a refractive index gradient, can be advantageous for the frequency doubling of chirped pulses. There is a strong similarity with periodically poled crystals where the period is chirped. While we cannot achieve the very high second order susceptibilities of some QPM crystals with LBO (which has an effective nonlinear coefficient of 0.85 pm/V for type I phase-matching), the use of a temperature gradient allows for great flexibility in design. We saw for instance that at different focusing conditions (fundamental peak intensity) the ideal temperature gradient can change. Here we investigated frequency doubling of pulses with a relatively low stretching (~3 times the TL duration) and highlighted several interesting effects. Just like in the case of QPM crystals, more complicated temperature profiles could also be used depending on the desired effect, with for instance periodical variations of temperature or parabolic temperature profiles. This novel technique can likely prove beneficial for parametric amplification.

Chapter 5:
Assembling and testing of a parametric amplification source for Multi-Photon Microscopy

The initial objective of this thesis was the construction of a new laser source based on optical parametrical amplification, to be used on a multiphoton microscope. Here we describe the design and properties of this laser source. The design was guided by simulation results. As can be expected, the output power is slightly smaller than predicted by simulations, because some ideal properties were assumed. The optical parametrical setup is composed of four distinct parts. First, a supercontinuum generation scheme which provides the seed to be amplified. Second, frequency doubling of the laser source so that it can be used as pump for the amplification. Third, the actual optical parametrical amplification, where the strong pump is used to amplify the weak seed signal. Fourth and last, the compressor so that the dispersion accumulated by the signal pulse can be removed.

The new tunable ultrashort laser source was integrated to a multiphoton microscope at EPFL, and the performances for different samples were compared with the existing femtosecond laser source. The throughput is significantly increased thanks to the much shorter pulse duration and higher pulse repetition rate. The improvement is in line with theoretical expectations.

The parametrical amplification setup described in the first section of this chapter was designed by Pierre-Marc Dansette and assembled together with Maksim Eremchev. Maksim Eremchev also did some of the experiments on supercontinuum generation in yttrium oxide and yttrium vanadate oxide. All microscopy experiments in the second half were performed conjointly by Pierre-Marc Dansette, Maksim Eremchev and David Roesel. The parametrical amplification design and assembling was supervised by Andrejus Michailovas, and the testing on the microscope by Sylvie Roke.

5.1 INTRODUCTION

Second harmonic microscopy and two photon excitation microscopy have intrinsic specificity to several biological tissues [12], [13], [31], and can also be used with some markers [19], [189]. Because the illumination is done in the near infrared the penetration depth is increased. Also, both processes are quadratically dependent on the intensity, so only the focal region will produce signal. Furthermore, those modalities can easily be combined to more informative images [17]. Those properties make them extremely attractive imaging modalities. Their main limitation is that intense illumination is required, meaning that femtosecond lasers are well suited as sources, as the average power can be quite low (preventing thermal damage) but the peak powers can be in the MW or GW range. Furthermore, tunable light sources are advantageous to probe the excitation wavelength of fluorophores.

Here we start with an Yb based fiber laser (1030nm central wavelength) with 260fs pulse duration but would like to achieve tunability and shorten the pulse duration. Our objective was to achieve a wide tunability range between 1000nm and 700nm in the visible and near infrared range, with pulses shorter than 50fs and pulse energy of at least hundred nJ. The output power of second order processes varies as $1/\tau$, where τ is the pulse duration, so the output signal should be higher for a given pulse power. Advantageously damage for ultrashort pulses is less sensitive to pulse duration [111], so shorter pulses should still allow for higher signal output while staying below the damage threshold.

We note that the pulse duration we expect to achieve is much shorter than that of our source laser. Indeed, the parametrical amplification process can be used to amplify pulses with a much larger bandwidth than the pump radiation [95] (and so a shorter pulse duration when compressed). The main limitations for the bandwidth of the output of a parametrical scheme are the bandwidth of the weak input signal and the phasematching in the nonlinear crystal.

5.2 PARAMETRICAL AMPLIFICATION

5.2.1   Initial laser source

Our source laser is a Femtolux 3 [216] from Ekspla Ltd. This is an Yb doped fiber laser with a compressed pulse duration of 260fs at 1030nm, 1MHz repetition rate and 3.3W of maximum output power. This means each pulse has a maximum energy of 3.3µJ. The output beam is nearly Gaussian with a beam quality factor M^2 of 1.1, though the pulse is not necessarily perfectly Gaussian (Chapter 3 section 4). The pulse compression is insured by a chirped fiber Bragg grating [203] and by detuning it is possible to introduce a desired amount of group delay dispersion (GDD) and increase the pulse duration. The repetition rate can be reduced with an optoacoustic element. It is also possible to increase the repetition rate beyond 1MHz, but the maximum output power remains 3.3W, meaning the pulse energy decreases. This is not advisable for use in second order nonlinear system such as Multi-photon microscopes, as the second harmonic energy depends quadratically on the fundamental pulse energy, and the increased repetition rate will only linearly affect the second harmonic power. Furthermore the use of too high a repetition rate can cause thermal damage to the samples [38].

5.2.2   Optical scheme

In order to achieve the desired results, we will need to perform several nonlinear transformations with our initial laser. The optical scheme for the entire parametric amplification process is shown figure 5-1.

The beam is initially split, with part of the energy is used for supercontinuum generation (SC generation) in a nonlinear crystal, here YVO_4. SC generation is a process through which a very wide bandwidth (often octave spanning) but low energy pulse can be generated when a narrower bandwidth radiation is focused in matter (there can be supercontinuum in liquids [217], [218] and gases [219], [220] as well as crystals). Unlike all other processes described in this work so far, SC generation is not only a second order nonlinear phenomenon, but also includes high order nonlinear interaction, self-focusing (a third order effect), Raman scattering and plasma generation. The SC

radiation should include all of our tunability range. A portion will later be amplified by the optical parametric amplifier (OPA).
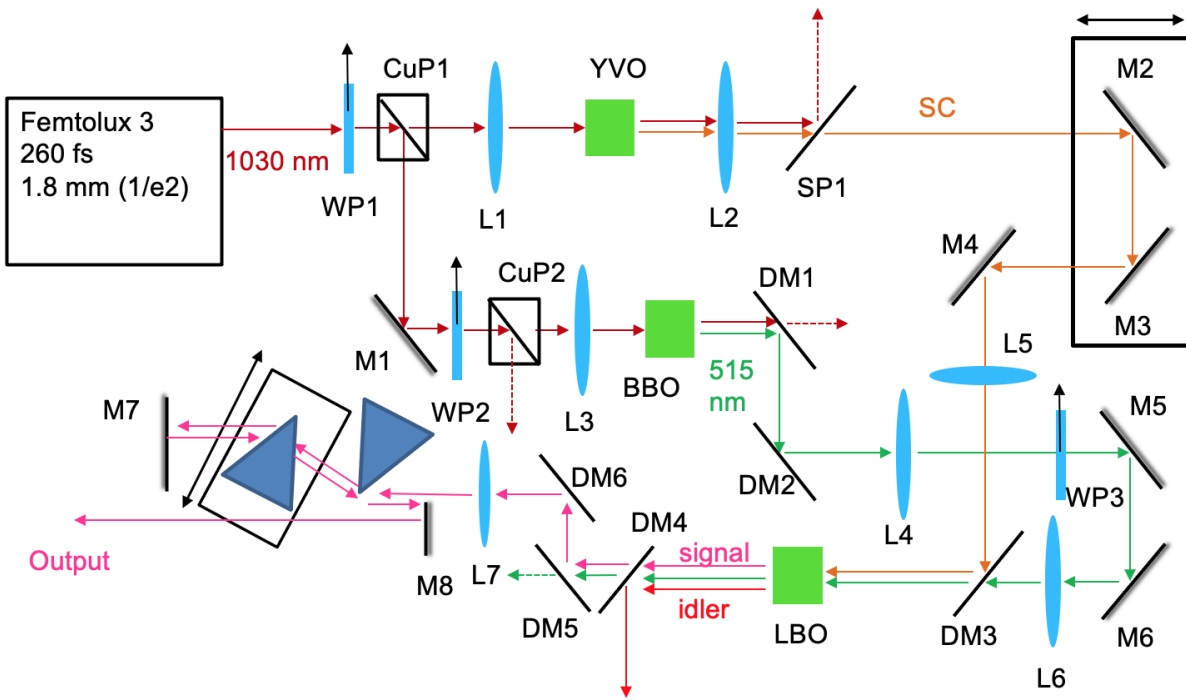
Figure 5-1: Optical scheme for the complete parametrical amplification setup. Abbreviations used: WP=Waveplate; CuP=Cube polarizer; L=Lens; SP=Short pass filter; M=Mirror; DM=Dichroic mirror; SC= supercontinuum; YVO_4=Yttrium orthovanadate; BBO= Beta-barium borate; LBO=Lithium tri-borate.

The portion of the beam that is not used for SC generation is frequency doubled in a BBO crystal (the central wavelength becomes 515nm). Phasematching for second harmonic generation is achieved by rotating the BBO crystal and the focal condition as well as the crystal properties are chosen to maximize conversion efficiency while maintaining good beam quality. The second harmonic beam can then be used as the pump at the optical parametrical amplification stage. For this the SH pulse needs to overlap the portion of the supercontinuum we want to amplify in time. Thus, we need a delay stage (mirrors M2 and M3). A dichroic mirror (DM3) lets us achieve spatial overlap of the SH and SC beams.

The actual parametrical amplification process takes place in a lithium tri-borate (LBO) crystal. The weak SC radiation is amplified by OPA with the strong second harmonic. A complementary wavelength is generated, called idler. We do not make use of the idler in our case. The tunability

range of the signal corresponds to idler radiation between 1100 and 2000nm. While those could also be used in nonlinear microscopy [221]–[223], we are limited by the sensitivity range of our camera and could not make use of it. The central wavelength of the signal is determined by both the angle of the LBO crystal (we use critical phasematching once more) and the delay between the SC and SH. At this stage we seek to achieve a broad enough bandwidth, high pulse energy and good beam spatial properties.

Finally, we need to compress the signal after the parametrical amplification. Indeed, the numerous optical elements add a significant amount of GDD, meaning the pulse duration is far from transform limited. The GDD can be removed with a prism compressor, the exact amount depending on the insertion of the second prism, which is placed on a translation stage.

We will now examine more thoroughly each part of the optical parametric amplification setup.

5.2.3   Supercontinuum generation

Supercontinuum generation in bulk nonlinear crystals happens when the intensity of a laser radiation is sufficient to generate femtosecond filamentation [103], [224]. Femtosecond filamentation is a complex phenomenon caused by a combination of self-focusing, self-phase modulation and plasma generation cause by ionisation via multi-photon absorption. This filament generates a coherent very wide bandwidth beam, that can cover the visible range for instance. This can be used as the source signal in parametrical amplification. Because self-focusing is required, there is a threshold power for supercontinuum generation. For a gaussian pulse the power threshold for self-focusing is:

$$P_{threshold} = \frac{3.72\,\lambda^2}{8\pi\,n_0(\lambda)\,n_2} \tag{5.1}$$

Where λ is the central wavelength of the laser, n_0 the refractive index of the material and n_2 the nonlinear refractive index. In our case the pulse is not necessarily Gaussian, so the coefficient might change slightly. Since we have a fixed pulse duration, for a given crystal we will look at the

pulse energy threshold instead of the power threshold. The higher the refractive index and nonlinear refractive index, the lower the threshold should be.

The main process causing spectral broadening of the supercontinuum is self-phase modulation, governed by the nonlinear refractive index n_2. Raman effect and four-wave mixing are also involved in the spectral broadening, to a lesser extent. While self-focusing on its own would indefinitely reduce the beam diameter, it competes with the diffracting effect of the plasma and losses from multiphoton absorption and ionisation. Thus, the intensity stabilizes at a certain level which is mainly determined by the bandgap U_g of the medium. The larger the bandgap, the higher the intensity and thus the broader the supercontinuum spectrum. Unfortunately the value of n_2 also tends to diminish for larger bandgaps [225].

The process of supercontinuum generation in photonic fibres has been well studied [226]–[229] and the many interacting nonlinear effects involved can be simulated [226], [230], [231]. However, this is a very different process because of soliton formation. Because the supercontinuum breaks into several solitons in fibres, it would also be difficult to use as a source of signal for parametric amplification.

The supercontinuum generation process in bulk crystal is not particularly efficient, with the SC energy often representing only a few percent of the energy of the input. Thus, we wish for the threshold energy to be as low as possible, so that we can keep more energy for second harmonic generation. When depletion of the pump can be neglected in OPA, the energy of the output signal depends exponentially on the pump energy and linearly on the input signal energy. While this approximation will no longer be entirely valid in our case (because at higher conversion efficiency the depletion of the pump can no longer be neglected), it shows that the priority should be to keep energy for pumping the OPA, not for the seed. We also cannot reuse the remaining pulse at 1030nm after SC generation, because its spatial and temporal properties are strongly affected by the many nonlinear processes. The second important characteristic of the SC for our application is its bandwidth. Indeed, we need it to cover all the tunability range of our OPA. Lastly, there should be no photodamage to the SC crystal. This is a problem as the requirement for SC generation is self-focusing and generation of a plasma filament, so we have to operate near damage threshold. The

SC spectrum extends on both side of the input wavelength, but here we use only wavelength shorter than 1000nm. The remains of the input radiation and the IR part are removed with a short pass filter.

Several candidate crystals were tested for our applications (figure 5-2). Here we will discuss the properties of the SC with a YAG (yttrium aluminium garnet), YVO_4 (yttrium orthovanadate), Y_2O_3 (yttrium oxide) and KGW (potassium gadolinium tungstate). The relevant properties for SC generation in those crystals are given table 5-1. Second order dispersion of the SC pulse is the product of GVD by the crystal length after the filament. Other optical elements will also contribute. The higher the dispersion of the SC, the more separated in time the different spectral components will be. This can reduce the bandwidth of the amplified signal after the OPA because only part of the SC overlaps the pump pulse in time. GVD also affects the SC generation as it quickly separates the different spectral components, limiting how long they can interact in the filament.

Crystal	n_0 at 1030nm	n_2 $(10^{-20}m^2/W)$	U_g (eV)	GVD at 800nm[*] (fs^2/mm)
YAG	1.82 [232]	6.2 [233]	6.5 [234]	98
YVO_4	1.96 [235]	15 [236]	3.8 [237]	286
Y_2O_3	1.90 [238]	5.8 [239]	5.8 [240]	186
KGW	2.06/2.01 [**] [241]	11 [236]	4.05 [241]	293/256 [**]

Table 5-1: relevant optical properties of different nonlinear materials for supercontinuum generation. Refractive index n_0, nonlinear refractive index n_2 (both for the central wavelength of the laser), bandgap and GVD in the spectral region of interest (for the supercontinuum). [*] The group velocity dispersion calculated from the same Sellmeier equation as the refractive index [**] refractive indexes n_g and n_m and corresponding GVD of KGW as the crystal we use is birefringent (b-cut)
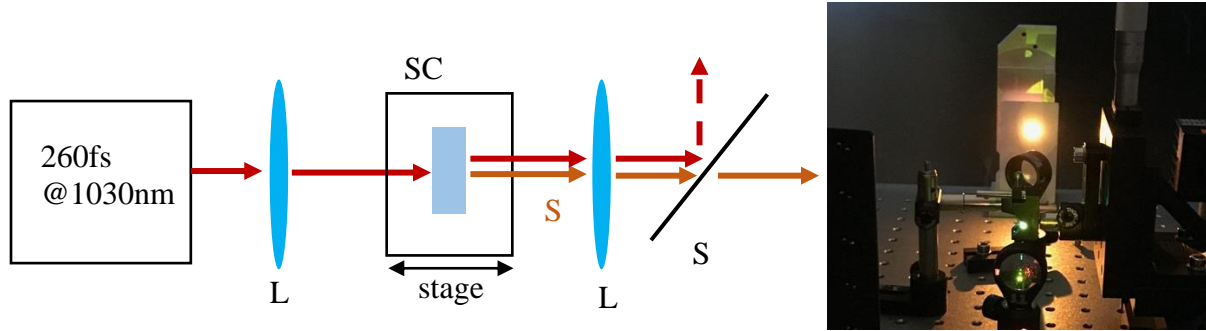
Figure 5-2: Left: Optical scheme for testing supercontinuum generation in different crystals. The SC crystal is mounted on a translation stage so that the position of the filament can be shifted in the crystal. L1 is the focusing lens with f from 30mm to 75mm and L2 the achromatic collimating lens (f=30mm). SP is a 1000nm short pass filter. Several measurements can be performed on the output SC beam: Z-scan to calculate M^2 as well as spectrum and power measurement. Right: Photo of the supercontinuum and the optical elements with a YAG crystal.

5.2.3.1 Yttrium aluminium garnet

Supercontinuum was generated in a 5mm YAG crystal, towards the end of the crystal, and with a numerical aperture (NA) of 0.04 (focal length of 50mm with a 2mm collimated beam from the Femtolux3). Several numerical apertures were tested, and this led to the best stability. The measured threshold for SC generation was 625nJ, which is a rather large portion our total pulse energy out of the femtolux laser (3.3µJ). Generating SC just above the energy threshold leads to a large instability, as the SC can vanish with small variations of the input pulse properties. It is only from 700nJ that the SC becomes stable enough for use in parametric amplification. From figure 5-3 we see that the cut-off wavelength of the SC starts around 500nm and slightly increases with the input pulse energy. This is more than enough bandwidth to cover our whole tunability range. The spectrum has a large peak around 600nm and almost linearly decreases from 650 to 950nm. For an input energy of 2.6µJ we observe interference fringes in the spectrum near 900nm. This means that the energy is high enough for 2 plasma filaments to form. In our case, it is desirable for the spectrum to be as smooth as possible as the spectral features of the SC will be partially transmitted to the final amplified signal (though the OPA process can have a smoothing effect).
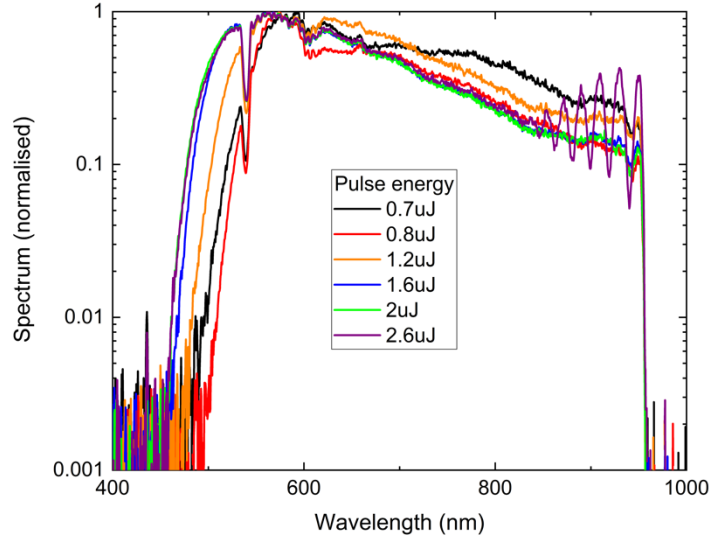
Figure 5-3: Spectrum of SC with YAG for different input energy (at 1030nm, ~250fs) Additionally, we need the SC to be stable both on the short and long term. The total standard deviation of the power of the supercontinuum was 3.4% for 700nJ input energy over two minutes. This value might seem high, but the parametrical amplification tends to reduce energy variations when depletion of the pump is significant for the amplified signal because a higher initial signal energy will lead to more depletion of the pump and so lower conversion efficiency (and the opposite for a lower signal energy).

Furthermore, the SC beam was then focused on a photodetector. This lets us separately detect each pulse, and we then measure the standard deviation of the photodetector signal for 400 pulses. It should be noted that the voltage variation measured from the Si based photodetector do not truly show the pulse shape, as there is a nanosecond rise and fall time for the photodiode current. Yet because we operate the photodiode in photoconductive mode [242], the dependence of the voltage on the peak intensity is linear. Thus, the standard deviation of the peak voltage should also be the standard deviation of the peaks measured with the photodiode. The measured standard deviation was only 0.7% for our whole SC bandwidth (after the short-pass filter). Bandpass filter with a bandwidth of 40nm were used to investigate the SC stability around 700, 800, 850 and 900nm. At 900nm the standard deviation rose up to 0.88%, most likely because we have less SC power. Standard deviation also rose to 0.83% at 700nm, likely because we are closer to the spectral peak (600nm, see figure 5.3) which tends to be slightly unstable. For 800 and 850nm standard deviation was less than 0.3%. A very good pulse to pulse stability is actually an expected feature for SC generation [103]. The discrepancy between the standard deviation measured with the powermeter and the photodiode might be linked to the different times considered: two minutes in the first case

and 0.4ms (400 pulses) in the second. This means the variations of the SC are slower (possibly due to some thermal instability in the original laser pulse for instance)

In order to evaluate the effect of long-term use, the power of the supercontinuum was then measure over 50h of continuous use and remained the same with a small increase of the standard deviation up to 5%. The increased standard deviation might indicate some small amount of damage to the crystal, but this is still very satisfying for our application. If the crystal becomes damaged it is possible to simply rotate it slightly so that the location of the filament changes, as long as the damage doesn't occur too fast.

Globally YAG was a good candidate as it exhibits good stability and a wide supercontinuum spectrum. The only negative point is that 700nJ necessary for a stable supercontinuum represents more than 20% of our energy budget. The good stability of the SC generated with YAG is not surprising as YAG is widely used for SC generation as a source of signal for parametric amplification[243], [244]. Because the product of n_2 and n_0 determines the energy threshold, the other crystals should have a lower threshold (see table 5-1).

5.2.3.2 Yttrium orthovanadate

The yttrium orthovanadate (YVO$_4$) crystal we used was 4mm long, numerical aperture was NA=0.67, and the crystal was translated so the filament was towards the back end of the crystal. The energy threshold was measured at 180nJ, and the supercontinuum becomes reasonably stable (enough to perform measurements) after 220nJ. The SC spectra are shown figure 5-4 for different input pulse energies. Near the threshold (225nJ) the SC cuts off at ~740nm, which is too short for our application. If we increase pulse energy to 300nJ, the cut-off wavelength becomes 640nm, so the SC covers our whole desired tunability range. The shape of the spectrum is more dependent on the pulse energy than with YAG, with a very strong peak (ten times as intense as the rest of the SC spectrum) appearing around 650nm for 600nJ pulse energy for instance. Interference due to the formation of a second filament starts appearing for a 1.1 µJ pulse energy, though they are not as well defined as for YAG. The 300nJ and 350nJ spectra are quite nice for our application as they

are relatively flat from 700 to 900nm. The dip around 950nm is less favourable, but the SC generated with YAG was also much less energetic around 950nm than 700nm (figure 5-3).
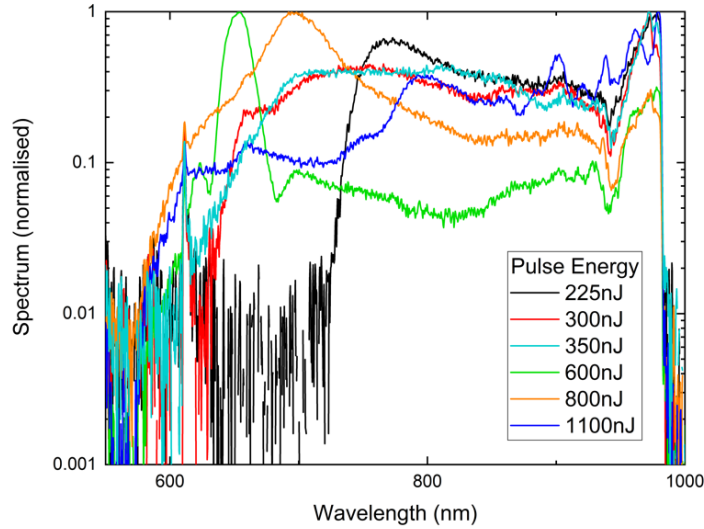
Figure 5-4: Spectrum of supercontinuum in YVO_4 for different input pulse energy

The next step was investigating the stability of the SC. With 350nJ input pulse energy the SC pulse energy (the portion above 1000nm wavelength) was 8nJ with only 0.5% standard deviation of the measured SC power (possibly even lower as this might come from the powermeter and not the SC generation itself). The standard deviation was similar when bandpass filters were used (as for YAG) to check the stability on different spectral ranges.
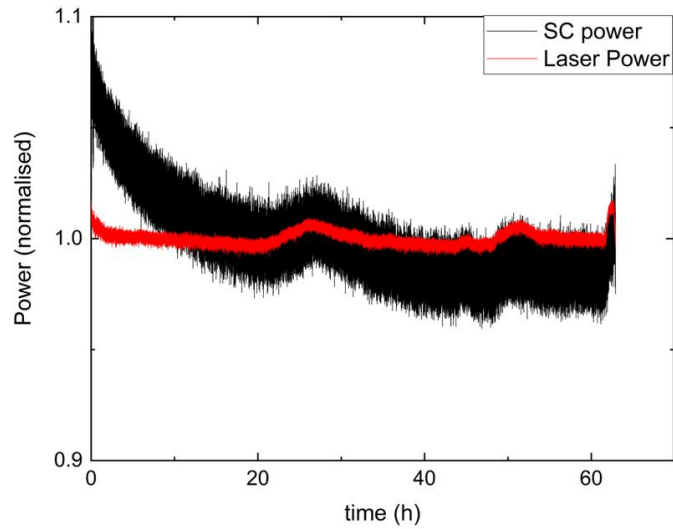
Figure 5-5: Supercontinuum (black) and laser (red) power evolution over 63h of use.

Thirdly, the SC power was measured over 63h along with the laser power (figure 5-5). The average power of the SC was 8nJ, but here the normalised power is plotted for both the laser and the SC on the same graph. We can observe an early drop of the SC power that also correspond to a smaller drop of the laser power. Some of the other long scale changes (after 24h and towards the end of the 63h) also correspond to changes in the laser power. The laser properties probably varied due to thermal effects. The change may also affect pulse duration, which explains why the SC power drops faster than the laser power during the first 10 hours. Those might be due to the thermal conditions in the room for instance. There is no sign of damage to the crystal, which is our main concern.

Finally, a Z-scan was performed on the SC beam. This means focusing the beam with a long focal length achromatic (because the SC is broadband) lens (200mm) and measuring the beam diameters in two orthogonal direction for different positions of the camera relative to the focus. By fitting the curves, the beam quality parameter M^2 is calculated (the larger M^2, the larger the divergence angle for a given focal diameter). Initially a very large M^2 of more than 3 was measured, but by introducing an iris after the collimating lens (Figure 5.2), we can largely improve the beam quality without too large a loss of power (about 20%). Indeed, there is a cone of angularly dispersed light around the SC [103], yet the centre of the beam is not angularly dispersed. The beam quality was measured after 3 different bandpass filter centred around 700, 800 and 900nm respectively, with 40nm bandwidth. At 800 and 900nm, an M^2 of 1.1, which nearly corresponds to a Gaussian beam. At 700nm M^2 is 1.5, which would be too high for our final output of the OPA. However, the signal and idler spatial properties mostly depend on the pump for the OPA (The second harmonic of our laser source) and not the seed. Thus, an M^2 of 1.5 is still acceptable. It would mostly affect the focusing conditions inside the parametric amplification crystal and might reduce conversion efficiency, but the spectral density of energy is also higher at 700nm which should compensate.

YVO_4 is an excellent candidate for the SC generation as the source of a seed pulse for our OPA. The energy threshold of 180nJ is much lower than YAG (625nJ), and the pulse energy we found to provide satisfying stability of the SC is 350nJ, versus 700nJ for YAG. As long as we use an iris to select only the central part of the SC beam, the beam quality is quite good. Furthermore, the

stability properties are exceptionally good and no damage was observed on a 63h of use period. With 350nJ initial energy we can get 4nJ of SC after the short pass filter and iris.

5.2.3.3 Yttrium oxide

The energy threshold for SC generation with Y_2O_3 was measured at 260nJ. This is slightly higher (but similar) to YVO_4, which can be a little surprising because the refractive index and nonlinear refractive index are almost the same as for YAG, which has a much higher threshold. While this would make Y_2O_3 a good candidate for the SC generation, it gets damaged extremely fast. We initially used a Y_2O_3 ceramic to generate SC, before trying a Y_2O_3 monocrystal in case the damage was due to the defects in the ceramic. In both case the SC lasted less than a minute even when the pulse energy was kept near the threshold. The damage also occurred independently of the focusing conditions (for a focal length of 30, 50 or 75mm of the focusing lens) The damage mechanism was determined to be inelastic because even blocking the laser and waiting for a few minutes before unblocking it didn't restore the Supercontinuum. Also, the damage appears not to be thermal: The pulse repetition rate was lowered down to 10kHz, yet after a few minutes of SC generation (in a fresh position in the crystal) the SC still extinguished. Thermal damage should be strongly dependent on the pulse repetition rate[201], unlike what we observed. The duration after which we observe damage is also relatively random. Thus, damage is likely caused by a single pulse, and intensity related.
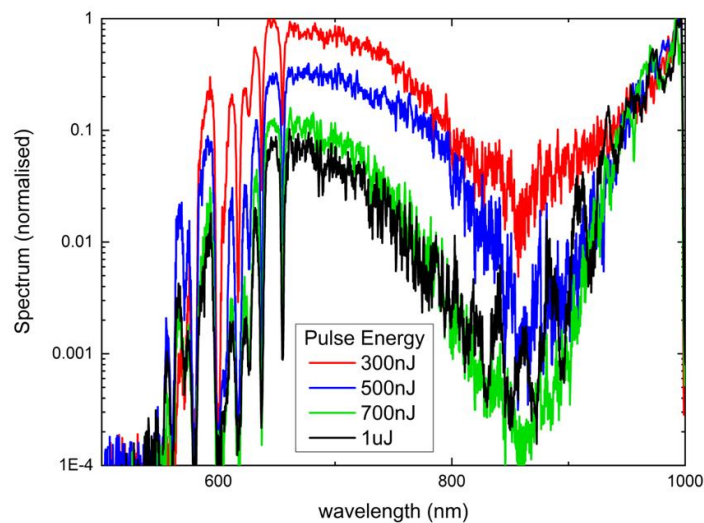
Figure 5-6: Supercontinuum spectrum in Y_2O_3 for different values of the input pulse energy.

The spectrum of the SC was still measured for different values of the pulse energy (figure 5-6). The repetition rate was lowered to 10kHz so that there was enough time to acquire spectra. The cutoff wavelength is around 570nm, worse than YAG (~500nm) but slightly better than for YVO$_4$. This matches theory as the main parameter for the extent of the SC is the bandgap (see table 5-1). The spectral energy density sharply drops around 850nm (~40 times less than at the peak around 700nm). This would also be a very bad feature for our application. There are several sharp gaps in the spectrum between 570 and 650nm. For 1μJ input pulse energy, we can observe interference fringes from 800 to 1000nm, indicating a second filament.

Yttria oxide cannot be used for our OPA because the damage occurs too fast. Even without the damage problem, Y$_2$O$_3$ would not be particularly suitable as the SC is too weak between 800nm and 900nm.

5.2.3.4 Potassium gadolinium tungstate

The crystal used in experiments was a 4mm long b-cut potassium gadolinium tungstate (KGW) crystal, so it was birefringent for a normal angle of incidence, unlike the other crystals we used. This means the two different polarisations need to be tested. The numerical aperture was 0.04. In the following, the polarisation giving the highest SC power will be called polarisation 1 and the other one polarisation 2. The threshold for SC generation was found at 220nJ for polarisation 1 and at 240nJ for polarisation 2. This is a little higher than YVO$_4$, but quite similar. The spectrum dependence on the input pulse energy is shown for both polarisations figure 5-7. There is a hole in the spectrum around 900nm, which is deeper for polarisation 2 (about 1/10th of the 700nm peak, compared to ~1/5th for polarisation 1. The cut-off wavelength gets shorter for increasing pulse energy when near the threshold and stabilizes around 570nm for 400nJ pulse energy or higher. This is broad enough for our application. There are interference patterns indicating the formation of a second filament from 400nJ already (particularly visible for polarisation 2). The spectrum is otherwise relatively smooth.
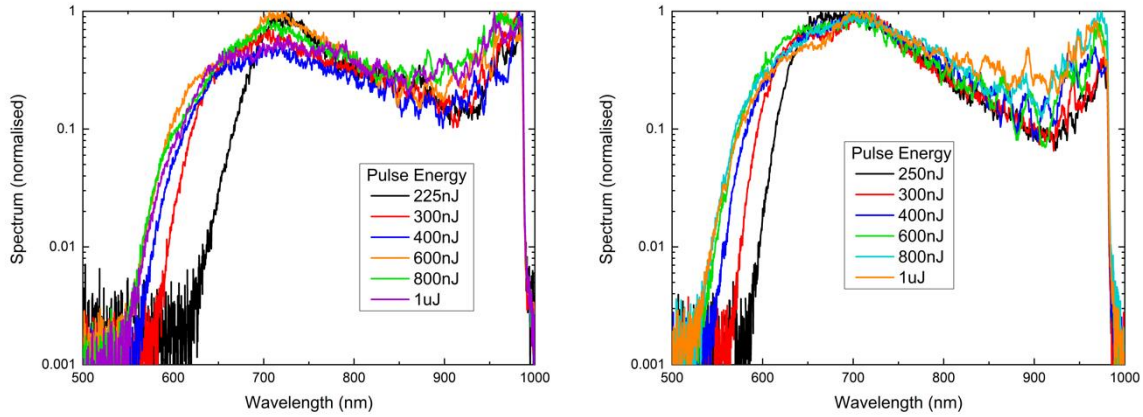
Figure 5-7: Spectrum of the supercontinuum for KGW for each of the 2 main polarisations (left and right) and for different input pulse energy

The short-term standard deviation was once again measured around 1% for the whole supercontinuum for 350nJ input pulse energy as well as around 700, 800 and 900nm with bandpass filters. No damage was observed over a 12h long measurement of the SC power with 400nJ pulse energy. Advantageously the SC pulse energy is 12nJ for 400nJ input pulse energy, to compare with ~8nJ for YVO_4 at the same input pulse energy. Finally, the beam quality of the SC after an iris was 1.2, which is quite good

5.2.3.5 Conclusions of Supercontinuum experiments

The two crystals that appear the most suited for providing an OPA seed via supercontinuum generation are YVO_4 and KGW. In both case the bandwidth of the supercontinuum is large enough to cover our whole tunability range, no damage to the crystal was observed over long periods of use and the required pulse energy for a stable Supercontinuum, between 300 and 400nJ, is not too high compared to our total pulse energy of about 3µJ. The SC produced with KGW is slightly more energetic, but the spectrum of the SC produced with YVO_4 has less variations so it could be more suitable. Both crystals were later used.

The supercontinuum produced with YAG was also stable and with a broad bandwidth, but threshold energy is higher. Yttria oxide appears unsuitable for SC generation due to damage. Diamond was also tested, but the threshold energy was found at 600nJ, which makes it less suitable.

5.2.4 Second harmonic generation

The principle of parametrical amplification is to amplify a weak seed pulse with a stronger pump pulse by difference frequency generation. This means the frequency of the pump pulse has to be higher than that of the seed. Thus, we cannot directly use our 1030nm to pump the OPA and we need to frequency double the laser. This is done in a nonlinear second order crystal, in that case BBO. The objective is to maximize the conversion efficiency while keeping good spatial and temporal properties of the SH. Indeed, the pump properties will influence the output of the OPA the most.
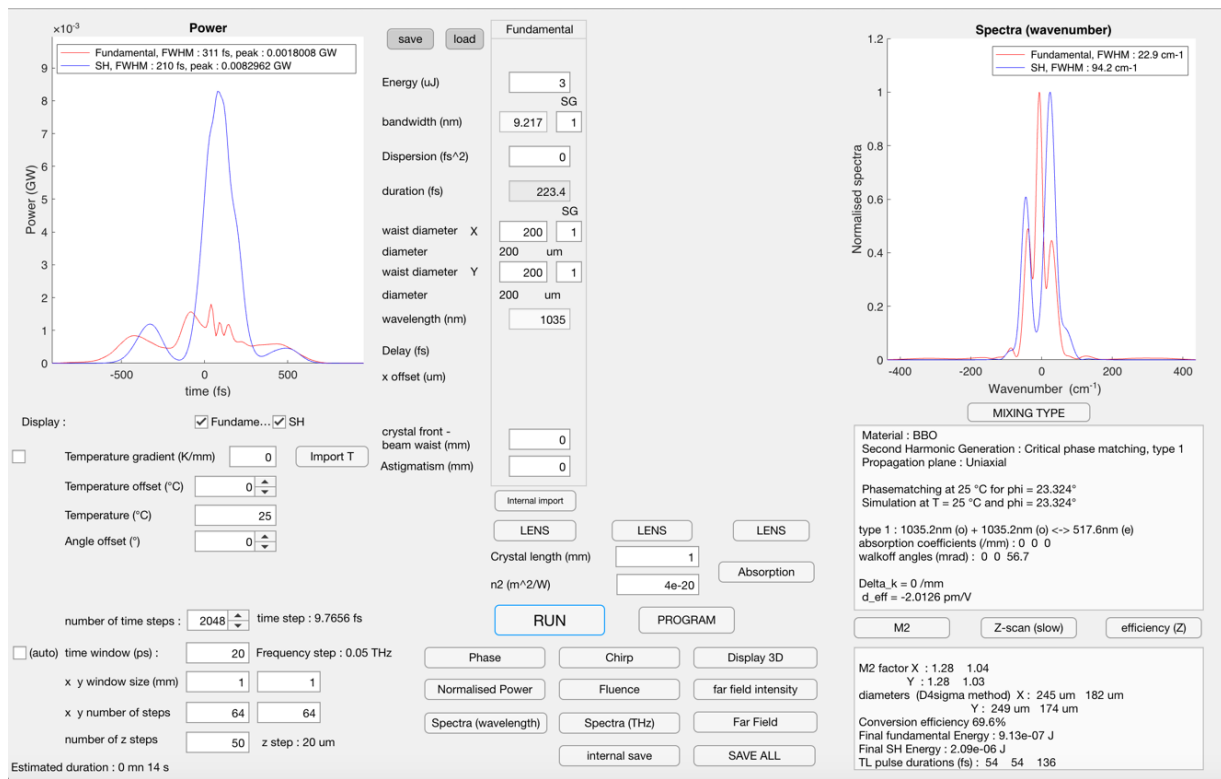
Figure 5-8: Simulation results for second harmonic generation in a 1mm BBO crystal, using the femtolux 3 pulse profile and phase retrieved with FROG. The beam quality of the SH is 1.04, the total conversion efficiency 69,6%

In order to find the right crystal length and beam diameter, the SHG process was simulated using the "Wavemixer" program we created. The pulse profile and phase of our laser was retrieved with FROG [183], and is the same as in chapter 3. The best SH conversion efficiency was obtained for a 1mm long BBO crystal cut for type I phase matching (θ=23.4° and ϕ=90°) and a 200µm beam diameter of the fundamental. The simulation results are shown figure 5-8. The predicted

conversion efficiency of ~70% is quite high, while the beam quality of the SH remains very good at 1.04. The SH spectra will display 2 strong peaks, but this should not affect the OPA much. The pulse has some side lobes, due to the third order dispersion inherited from the fundamental radiation. The SH pulse duration should be 210fs (full width at half maximum). Having too short a SH pulse can limit the bandwidth of the signal pulse out of the OPA, if the SC is dispersed. Indeed, the different wavelength of the SC will then be separated in time, which means the portion that overlaps the SH can have a much shorter bandwidth than the whole SC.
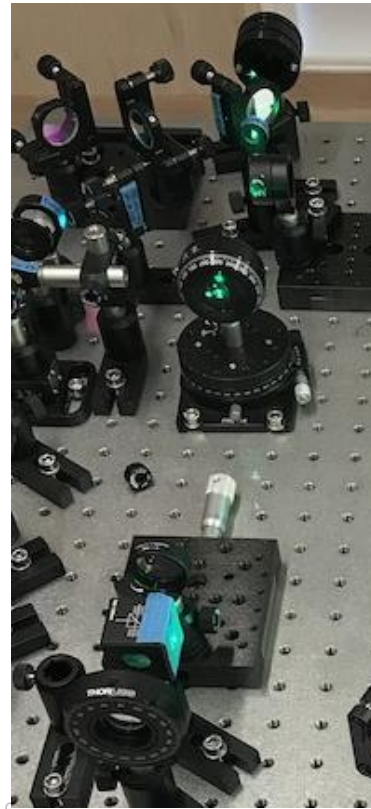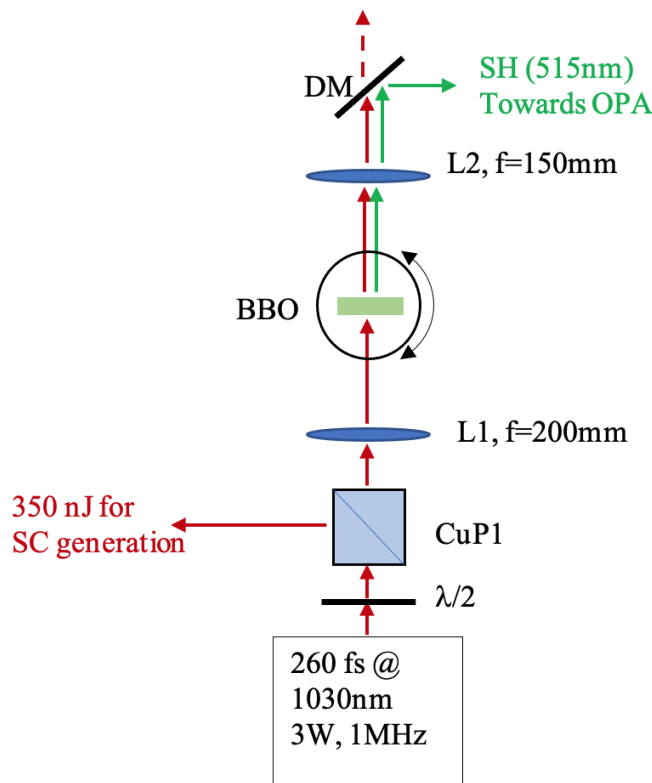
Figure 5-9: Optical scheme of the second harmonic generation setup (left) and photo of the SHG part of the final OPA (right).

The simulation results let us choose the appropriate focal length and crystal length for the experimental setup. The optical scheme of the experimental SH setup is shown figure 5-9 as well as an image of the mounted optics. The portion of the beam that will be used for SC generation is separated with a half waveplate and cube polarizer, and what remains is focused on the 1mm BBO crystal with a 200mm focal length lens. The orientation of the BBO crystal is adjusted with a rotation stage. The mount of the BBO crystal is also a rotation mount so that the polarisation of

the fundamental radiation can be aligned with the ordinary polarisation for the BBO crystal. The SH pulse will be emitted with the extraordinary polarisation. After collimating the SH beam, the remains of the fundamental are removed with a dichroic mirror and the SH can then be used for parametric amplification. With this setup we measured a maximum conversion efficiency of 61,4% with 2,7μJ of fundamental energy. Indeed, the output power of our source was 3W, instead of the 3.3W specified. This is quite close to the prediction from simulation. The slightly lower efficiency can be explained by the perfect conditions we assume in simulation are not met (non-Gaussian beam, slightly wrong angle…) and small differences between the retrieved pulse and phase and the real one. The beam quality parameter of the SH was measured by Z-scan to be 1.11 and 1.21 along the two axes of the beam. This is worse than in simulation, but the real fundamental beam also has M^2=1.1. It is still good for practical applications.

5.2.5 Parametric amplification

Crystal	type	d_{eff} (pm/V)	ρ (mrad)	n_2 ($10^{-20}m^2$/W)	Δn_g p-s / p-i
LBO [196]	I	0.84 [149]	7.1	2.6 [197]	0.010/0.015
BBO[245]	I	2.01 [149]	55.7	4 [197]	0.020/0.034
BiBO [246]	II	2.96 [151]	24.9 / 24.4 [*]	15 [247]	0.040/0.081

Table 5-2: Relevant properties of different crystals for DFG with a 515nm pump wavelength and 800nm signal wavelength (1446nm idler wavelength d_{eff} is the effective nonlinear coefficient, ρ the walk-off, n_2 the nonlinear refractive index and Δn_g the refractive index difference between signal and pump (s-p) and idler and pump (i-p). d_{eff} was calculated using the known D_{eff} matrix (references next to the d_{eff} values), the phasematching conditions and Miller's rule [5] to adjust for wavelength. The phasematching conditions, ρ and Δn_g are calculated from the Sellmeier equations for the crystal (reference next to the crystal name). [*] In BiBO the walk off is for the signal and idler, as they are along the extraordinary direction (type II phasematching)

The previous two steps let us generate a broadband seed that covers our whole tunability range and convert our 1030nm source laser to its 515nm second harmonic, thus having a strong beam with a shorter wavelength than what we wish to amplify. The first question is which nonlinear crystal to choose? Three bulk crystals are aften used for visible range OPA or SHG: BiBO

(Bismuth triborate), LBO (lithium triborate) and BBO (beta barium borate). The relevant properties for all 3 are shown table 5.2

The effective nonlinear coefficient might seem like the most important parameter for a nonlinear crystal as it will directly affect how strong the nonlinear interaction is. Indeed, the larger d_{eff}, the sooner we will reach a peak of conversion efficiency (before DFG stops and back conversion, meaning SFG in this case, starts). Therefore, the main question becomes what limits the crystal length we can use? Four effects can degrade the properties of the signal and idler radiation as well as reduce the DFG efficiency: Loss of spatial overlap due to walk-off, loss of temporal overlap due group index difference, insufficient phasematching bandwidth and Kerr effect (self and cross phase modulation). In a first order approximation the phasematching bandwidth is proportional to the signal-idler group index difference (which we can calculate from the other two). So, for each of these effects a figure of merit is the ratio of the relevant parameter to d_{eff}. For spatial overlap, BBO is the worst while LBO and BiBO are mostly equivalent). For Kerr effect, BBO is the best though LBO is quite similar, and BiBO the worst. BBO and LBO are very close for temporal overlap and the phasematching bandwidth, while BiBO is worse for both. Ideally the beam diameters for DFG need to be as small as possible, because a higher intensity means a higher rate of conversion and so a shorter crystal needed. The limitations are the damage to the threshold and Kerr effect, which is also intensity dependent. With a pulse energy of 1,66 µJ, and a beam diameter of 100 µm, a suitable crystal length for BBO is 1,5mm, meaning a spatial shift of about 80µm due to walk-off. Because the spatial shift is almost as large as the beam, this will strongly affect the DFG and the output beam quality. Indeed, simulations confirmed that BBO is the worst crystal in our case.

Wavelength (nm)	BiBO				LBO			
	Efficiency (%)	M^2	TL duration (fs) Signal	Idler	Efficiency (%)	M^2	TL duration (fs) Signal	Idler
900	21,9	1.5	21.3	24	26.4	1.4	21.1	22.8
850	20	1.4	24.2	28.7	25.1	1.3	22	24.3
800	17.5	1.25	28.8	36.2	23.4	1.2	23.4	26.8
700	6.2	1.05	35.9	58.2	22.3	1.1	23.3	27.7

Table 5-3: Main simulation results for DFG in a 1mm BiBO crystal and 3.2mm LBO crystal using the simulated SH pulse from figure 5-8, and an 80nm bandwidth seed with 1nJ of energy centred at 4 different wavelength, with a 100µm beam diameter for both the SH and seed, stretched with a GDD of 1000fs^2 (estimated GDD on the SC due to the different optics). Efficiency is the total energy converted to signal and idler compared to the initial pump energy.

The choice is now between LBO and BiBO. Table 5-3 contains the main results of simulations for both of those case. Here I didn't use the real spectrum of the SC, but a Super Gaussian spectrum with a large bandwidth (80nm), centred on different wavelength. Nevertheless, this lets us compare the two crystals for conditions close to our OPA. The crystal length was chosen to maximise conversion efficiency while maintaining a good beam quality at 850nm ($M^2 < 1.4$), and the same conditions were kept for all other wavelengths. Indeed, while we can modify the angle of the crystal and the delay between SH and SC, we cannot in practice change the beam diameter or crystal length for each wavelength. Generally, the conversion efficiency is lower with BiBO. In particular, it drops down massively at 700nm (only 6%). We also observe that the TL duration of the signal and idler increases at 700nm, meaning the phasematching bandwidth is too small. By comparison the conversion efficiency varies little in LBO (from 22.3% to 26.4%), and the TL duration also stays around 22fs, meaning the whole bandwidth is amplified. Beam quality is better at shorter wavelength, meaning a longer crystal might let us reach even higher conversion efficiency there, but then it would be too long for pulses centred on 900nm (and beam quality would worsen). A maximum overall conversion efficiency of 26% can seem quite low compared to the 70% reached (in simulation) for SHG. This is because type I SHG is a degenerate case with only 2 radiations to consider, versus 3 different waves for SFG and DFG. In DFG the pump wave will locally deplete much faster at the temporal and spatial peak, and then back conversion will

start locally, damaging the beam and the conversion efficiency. In SHG, when the fundamental is depleted there is nothing left for DFG (in that case back conversion) to start. It is possible to increase DFG conversion efficiency by using flat topped beams and/or pulses [105], [248], but not in our case, because good beam focusability is required for microscopy.

One of the most important results of the simulations is the effect of the GDD accumulated by the supercontinuum. For an 80nm bandwidth super Gaussian spectrum centred on 800nm, the pulse duration will be stretched to ~200fs, the same as the SH pulse duration (see figure 5.8). From simulations, the GDD is the main limiting factor controlling the bandwidth of the signal, as even a 5mm LBO crystal is short enough to have phasematching over more than 80nm. This means the GDD of the SC needs to be kept as low as possible. Thus, all mirrors on the SC path need to be coated to be low GDD (GDD<$5fs^2$), as otherwise a single dielectric mirror can add $500fs^2$ of GDD. In total the GDD added by all optical elements on the path of the SC is between $1000fs^2$ and $1500fs^2$ depending on the wavelength.

For DFG simulation showed the best choice for material was LBO. The refractive indexes of LBO are strongly temperature sensitive. We could use non-critical phase matching (meaning use temperature to insure phasematching at the desired wavelength for a crystal cut along one of the optical planes) and so doing remove walk-off completely. However, the required temperatures are between 150 and 200°C, requiring special coatings. The stability of such systems can also be a problem. Therefore, we chose to use critical phasematching, with a crystal cut of $\theta=90°$ and $\phi=10°$, while the temperature of the crystal is fixed around 40°C by a specially designed mount. If the incidence angle of the beams is 0 on the crystal face, the phasematching conditions are met around 750nm. By adjusting the orientation of the crystal, the phasematching conditions can be met for different wavelengths. At 980 nm phasematching is observed for $\phi=13°$, so the maximum incidence angle should be 4.8° (those are the angles inside the crystal, and we need to account for refraction). In the end a 3mm long and a 5mm long LBO crystals were ordered and tested.

Finally, the DFG was experimentally realised. This is a much more complex system than SHG because we need to ensure temporal and spatial overlap. The temporal overlap is controlled with the delay stage on the SC path (see figure 5.1) and the spatial overlap was obtained by adjusting

the angles of DM3 and M6. A camera was used to check the beam diameters and that they are centred on the same positions. Initially finding the right position of the delay stage is difficult as the SC pulse duration is about 2ps, meaning the translation stage ideal position will vary by less than 1mm. The optical path (including the optical indices of all the optical elements) was calculated for the SC and SH to place the translation stage as close as possible to the ideal position. After the LBO crystal is placed the angle of DM3 is adjusted to tune the overlap even more precisely and maximize efficiency. Once some signal amplification is observed, the process of tuning the OPA for a given wavelength is relatively complex:

1- Measure the spectrum of the signal with a spectrometer. The SH and idler have been removed with a dichroic mirror.

2- Adjust the delay to shift the central wavelength of the spectrum in the right direction

3- Adjust the angle of the LBO crystal (with a precision rotation stage) to maximise the spectral peak. This should also shift the central peak.

4- Repeat 2 and 3 until the spectrum is centred on the right wavelength

5- Replace the spectrometer with a powermeter and very slightly adjust the crystal angle to maximize power.

6- Adjust the spatial overlap (DM3) to maximize the signal power

7- Adjust the SC crystal position (with a translation stage) to maximize the signal power. This also helps gain some more signal power (up to 10%)

8- Check one last time with the spectrometer that the central wavelength is still the same

The different measured spectra of the signal are shown figure 5.10. The spectrum is relatively Gaussian for central wavelength above 850nm. For a central wavelength around 900nm, we have a particularly broad spectrum (dark blue or red curves), but also several peaks. This comes from the supercontinuum spectrum which has a dip around 950nm. This spectral region corresponds to much lower GDD accumulated by the supercontinuum (the 0 dispersion of the different materials on the SC path will be between 1.4 and 2μm, so the dispersion is smaller for longer wavelength), which is why the amplification bandwidth is much larger. The strange shape of the spectrum should not strongly affect multiphoton microscopy as long as the pulse is well compressed. This also means the transform limited duration of the signal can be much shorter. For a central wavelength around 970nm, there is a clear cut-off around 1000 nm. This is due to the short-pass filter used to

separate the SC from the pump. The bandwidth of the signal becomes smaller for shorter wavelength. However, a given bandwidth (in nm) at 700nm corresponds to a much shorter TL duration than the same bandwidth centred on 900nm. This is because the TL pulse duration is proportional to the bandwidth in frequency, not in wavelength. The relationship is given by:

$$\Delta\nu = \frac{c}{\lambda_0^2}\,\Delta\lambda \tag{5.2}$$

Where λ_0 is the central wavelength, c the speed of light, $\Delta\lambda$ the bandwidth in wavelength and $\Delta\nu$ the bandwidth in frequency. The amplified signal power also varies with the central wavelength (figure 5.11). There is a peak around 750nm with signal powers of almost 200mW (meaning 200μJ signal pulse energy as the repetition rate is 1MHz). The power then drops down to 140mW around 850nm. There is also a strong increase of signal power for a central wavelength of 970nm. This corresponds to the sharply cut-off spectrum (black curve) figure 5.10. This spectral region corresponds to the remaining spectrum of the pump laser that was used for SC generation. The initial spectrum was much narrower but was broadened by self-phase modulation in the YVO$_4$ crystal, and there is still some of this spectral peak beyond the cut-off wavelength of the short pass filter. It is more intense than the rest of the SC and so can be amplified more easily. However, the bandwidth is very narrow, so the TL duration would be more than 50fs.
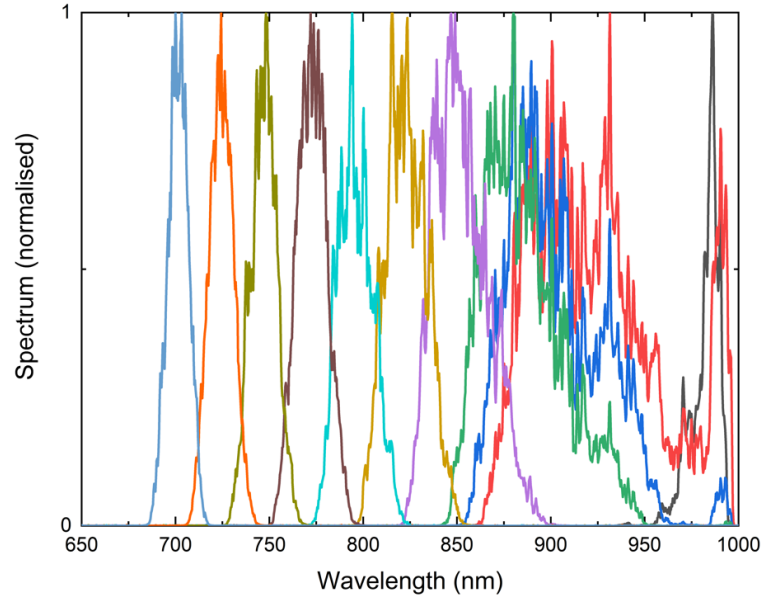
Figure 5-10: Spectra of the signal output of the OPA over the tunability range. Each spectrum corresponds to a specific delay between the SH and supercontinuum as well as a specific crystal angle.

The beam quality parameter M^2 was also measured by Z-scan for several central wavelength. While M^2 increases around 900nm, it remains quite good (the maximum is 1.22), so the focusability of the beam after the objective of the microscope should be good and the beam shape will be mostly Gaussian.
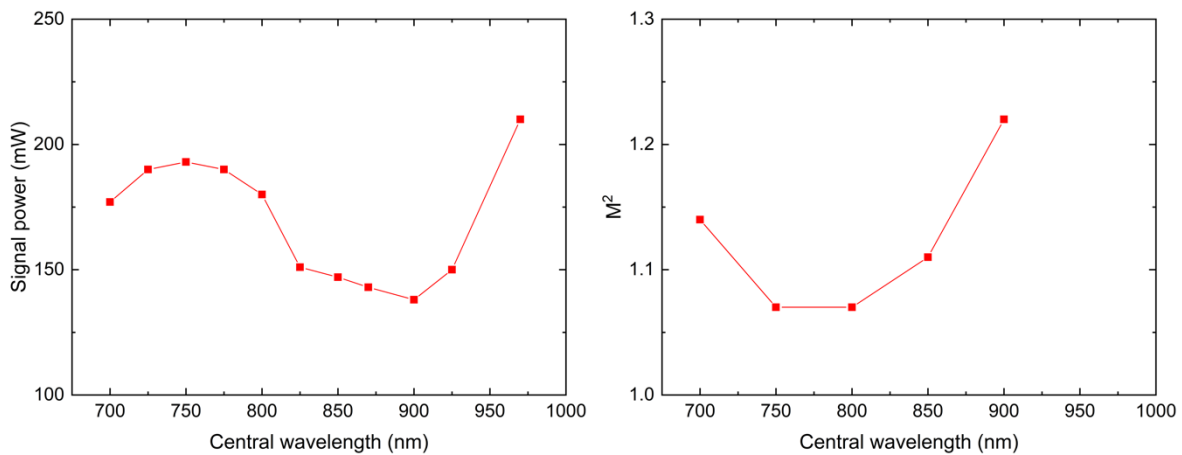
Figure 5-11: Left: OPA output (signal) power depending on the central wavelength. Right: beam quality parameter M^2 dependence on wavelength.

λ(nm) / Seed (mW)	Signal power (mW) / Beam quality parameter M^2					
	690 nm	750nm	800nm	850nm	900nm	970nm
0,1	40 / 1.07	28 / 1.07	15 / 1.08	5 / 1.16	4 / 1.2	9 / 1.11
0,2	67 / 1.08	50 / 1.07	27 / 1.08	10 / 1.16	7 / 1.2	18 / 1.11
0,5	137 / 1.08	100 / 1.08	59 / 1.09	23 / 1.16	17 / 1.2	38 / 1.11
1	198 / 1.11	150 / 1.1	97 / 1.1	41 / 1.16	31 / 1.2	64 / 1.12
2	259 / 1.16	203 / 1.15	145 / 1.12	72 / 1.17	55 / 1.2	98 / 1.14
5	323 / 1.27	266 / 1.26	211 / 1.2	129 / 1.2	105 / 1.22	148 / 1.22
10	357 / 1.39	306 / 1.37	258 / 1.29	179 / 1.25	153 / 1.25	188 / 1.32
20	379 / 1.53	342 / 1.51	303 / 1.42	231 / 1.34	204 / 1.32	228 / 1.45
50	403 / 1.73	402 / 1.69	370 / 1.6	305 / 1.51	277 / 1.45	289 / 1.63
Measured	177 / 1.14	193 /1.07	180 / 1.07	147 / 1.11	138 / 1.22	210 / −

Table 5-4: Simulated signal power and beam quality parameter M^2 for the OPA for different central wavelengths of the amplified signal, and different seed powers. The last line contains the measured values for the signal power and M^2. The simulations were performed using the simulated SH (figure 5.8) and the measured spectrum of the Supercontinuum, with both beam diameters of 180μm and a 5mm LBO crystal. I assume a GDD of 1500fs^2 on the supercontinuum.

Globally, the output of the OPA is satisfying. The tunability range is between 680 and 980nm and the bandwidth of the signal is broad enough to support pulse durations between 25 and 50fs. The power of the signal varies with the central wavelength but remains in a reasonable range (between 140 and 200mW). This is the lower end of the expected power range, and lower than we could expect from simulations. To better understand why, I performed a series of simulations using the actual supercontinuum spectrum, the SH pulse simulated using the FROG reconstructed laser pulse (figure 5.8) with the measure SH power (1.66W at 1MHz) and varied the SC power.

The main results of the simulation set are assembled table 5.4. Tis table is very rich in information. First, we can observe that for low values of the seed power (0.1 to 0.5mW) the final signal power depends mostly linearly on the seed power. This linear dependency can be predicted from the DFG

equations (see chapter 2) when the conversion efficiency is low. Second, the signal power varies significantly with wavelength for a given seed power. This might seem to contradict table 5.3. These simulations are quite different from those presented in figure 3, as I used the SC spectrum, meaning the seed power is no longer the same around each central wavelength (+/- 40nm). The shape of the Supercontinuum spectrum is reproduced, with a peak around 700nm and much lower spectral density around 900. However, the amplitude of the spectral variations lessens when the seed power increases, and we start to saturate (because we deplete the pump). For instance, at 0.1mW seed power, there is 10 times more signal at 690nm as there is at 900nm (which is about the difference in the SC spectrum as well), but at 50mW seed power there is only 1.5 times more signal power. It is also important of note that table 5.3 contains efficiency values, while here we have the signal power. The efficiency is the ratio of energy converted to signal and idler to the initial pump energy. The shorter the signal wavelength, the higher the share of energy that goes to the signal. Third, we surprisingly observe that the measured variations of signal power with the central wavelength are too low compared to simulations. For wavelength shorter than750nm, the signal power is lower than it should be for a 4mW seed (The SC power measured after the iris), but for longer wavelength the signal power is higher than in simulation, something which rarely happens. Here it is important to consider the steps we use for tuning the OPA: Step 7 is to change slightly the SC crystal position to maximize the output power. The SC spectrum depends on the position at which it is generated in the crystal, so in this step we are actually selecting the best SC spectrum for a given wavelength. The SC spectrum (from YVO_4) used in simulations has a particularly deep hole around 900nm (about 10 times less than the peak), but it is possible to have more energy at 900nm, but less in the SC overall. Also, we observe a peak at 750nm in measurements, when simulation predicts a higher power at 700nm. Here we need to remember that the M^2 for the SC was ~1.5 around 700nm, compared to ~1.1 elsewhere. Since the focusing lens for the OPA seed is the same for all wavelength, this means the SC diameter in the LBO crystal will be about 1.4 times greater at 700nm than at 800nm, so the intensity of the seed is halved, and the conversion efficiency is reduced.

The simulation results using the real SC spectrum and the same conditions as in the experimental setup let us understand why there is significant variation of the signal power when the central wavelength is tuned. It also shows that if the SC power was higher, it would be possible to reach

much higher conversion efficiency. This suggests that we could reach higher signal power by using a 2 stage OPA: A preamplification (with a 3mm LBO crystal for instance) using only part of the pump power, and a second (and final) amplification in a 5mm LBO crystal. While such a scheme can increase the output, it is also more complex than the setup figure 5.1, requiring a second delay stage, and a second spatial overlap of the signal beam with the SH beam, as well as more optics (which also adds some GDD).

The OPA scheme of figure 5.1 was tested as a source for the MPEM, with the properties measured so far. Indeed, it was better to test an already built setup (which worked fine even though the signal power is on the lower end of our expectations) and see later about improvements. This also let us keep the project on schedule. The main results presented further in this work are all for the 1 stage OPA with YVO_4 as the SC crystal. Later on, KGW was also tested as a replacement SC crystal (there was a small improvement) and a 2 stage OPA was assembled to see what the gain would be, and we began testing it.

5.2.6 Two stage parametrical amplification

Because the seed power in the second amplification is quite high (a few tens of mW), higher efficiency can be reached without affecting beam quality too much. Indeed, the limiting factor is that back conversion will start affecting the centre of the signal beam early in the crystal, while conversion is still ongoing on the beam sides, leading to the creation of a hole at the centre of the beam. The rate of conversion when the seed is weak is mostly governed by the squared SH intensity, so a Gaussian with a diameter of $d_{SH}/\sqrt{2}$, where d_{SH} is the SH diameter. When the seed is stronger the intensity of the seed also increases the conversion rate, which will affect the sides of the beam more than the centre, especially if the seed diameter is a little larger than the SH diameter.

Figure 5-12: Optical scheme of the 2 stage OPA. The SHG and SC generation are the same as in figure 5.1 and not shown again. The supercontinuum beam (SC) is shown just after the first delay stage (see figure 5.1), and the SH (at 515nm, in green) starts just after the collimation. Notations: L=lens; M=Mirror; DM= Dichroic mirror; $\lambda/2$= Half waveplate; LP= Long pass filter

The optical scheme for the 2 stage OPA is shown figure 5-12. The first part remains the same but the SH beam is split in 2 using a polariser and half waveplate. The weaker part is used to amplify a portion of the SC in a 5mm LBO crystal (same cut as before). The temporal overlap is obtained thanks to the delay stage on the SC path (not shown figure 5-12). After amplification the pump (515nm) and idler are removed with a dichroic mirror (DM2), and filters are used to remove any remains. Here a flippable mirror lets us collect the signal beam for testing its properties (spectrum

and power) or send it to the second stage of amplification. The largest part of the SH beams goes through a delay stage so that temporal overlap can be obtained in the second amplification crystal. This SH beam and the signal from the first stage of OPA are then focused (L4 and L5 respectively) and spatially overlapped (with dichroic mirror DM3) in the second OPA crystal (a 3mm LBO crystal with the same cut as previously). After the second and final amplification, the signal is separated from the pump and idler and can be sent in the prism compressor, which is not drawn again. The dichroic mirrors and the mirrors M4 and M5 need to be low GDD so that the signal is not too stretched in the second stage of amplification.

It is immediately apparent that adding a second stage of OPA makes the system much more complex. The tuning steps detailed in the previous section need to be performed for both stages, first to find the right wavelength and maximize efficiency in the stage 1 (Power and spectrum measured at "Test 1"), then maximizing the conversion efficiency of stage 2. The tuning of the second stage is a little easier because the spectrum should already be centred on the right wavelength. The important question is how much do we gain by adding a second stage of OPA?

The repartition of the SH energy and the crystal length of each LBO crystal was chosen with simulations in order to maximize the signal power. The main focus of the 2 stage OPA was to increase the signal power between 900 and 950nm, as this wavelength range produced an extremely broad spectrum but relatively low power (140mW) for a single stage OPA. Also, the camera used for the second harmonic microscope is particularly sensitive between 450 and 500nm, meaning it is better to use a central signal wavelength between 900 and 1000nm. Simulations showed that with 550mW of pump power (at 1MHz repetition rate) for the first stage the signal power should be between 30 and 50mW. This is lower than previously because the pump power is much lower. The second stage of amplification should then produce 370mW at the output of the second stage. This might seem quite high when compared to the signal power for 50mW seed power in table 5-4. However, in table 5-4 the power of the seed is spread over the whole supercontinuum bandwidth and most of it will be unamplified, while here the spectrum of the signal out of the first stage of amplification is mostly the same as the output of the second stage. The predicted bandwidth of the amplified signal is sufficient for a 27fs TL pulse, and the calculated beam quality is 1.13.

The output of the 2 stage OPA was only studied around 950nm central wavelength as this is the most advantageous for second harmonic microscopy in our case (as mentioned previously due to the spectral sensitivity of the camera). As expected, the addition of a second stage let us reach a significantly higher signal power, of 250mW (at 1MHz) compared to ~140mW with a single stage. Unfortunately, the spectral narrowing is significant, and the transform limited duration is around 60fs, compared to ~25fs for the single stage OPA. Overall, the SNR ratio of 2 photon microscopy images when the full power of the signal is used should still increase, because it quadratically depends on the pulse energy, but linearly depends on the duration. The real signal power is still significantly lower than predicted by simulations which is not surprising: The many optical elements can cause some losses even with the proper anti-reflection coating and the simulation makes some assumption that tend to improve efficiency (neglected TOD of the input SC, beam quality of the SC…) and is carried twice in a row. Also, the GDD added by the lenses and other elements was neglected at the time of simulations (because it was yet unknown), which explains the narrower bandwidth and some loss of conversion efficiency. Indeed, the pulse lengthening is likely due to the added GDD from the first LBO crystal (included in simulations) and all the new optical elements on the signal path (not included). Ideally, the signal could be partially recompressed before the second stage of OPA, but that adds a significant complexity.

The addition of a second stage of OPA is a late change to the system, and all testing was done with a single stage OPA. Improvement in the signal output of the microscope has been observed with the 2 stage OPA but the gain is marginal at best, considering the lengthening of the pulse. The rest of results are for the single stage OPA, unless specified otherwise.

5.2.7   Pulse compression

The output of the OPA has a large bandwidth, allowing for pulses shorter than 30fs at all the different wavelength considered. However, due to the accumulated GDD over the optical path of the SC, the pulses are significantly stretched. In fact, the simulations showed that the stretching of the SC making the SC pulse much longer than the pump pulse (with about 230fs pulse duration) is the main limiting factor for the signal bandwidth, which means the signal pulse will have

durations around 200fs. Therefore, the last element of the OPA scheme is a compressor for the signal.

Compression of an ultrashort pulse can be performed by different means. Inside the fibre laser the compression is achieved thanks to temperature tuning of a chirped fibre Bragg grating for instance [203]. For free space optics, the usual compressor schemes are a grating compressor [249] or a prism compressor. In both cases the different wavelengths are angularly separated and later recombined. Because each wavelength follows a different optical path, a certain amount of GDD can be added or subtracted, depending on the geometry. It is possible to compensate for higher orders of dispersion as well [214], [250] or to compensate for a particular spectral phase [213], but for ~30fs pulses it should not be necessary. Indeed, the effect of GDD is proportional to τ_{TL}^3 where τ_{TL} is the pulse TL duration, the effect of third order dispersion is proportional to τ_{TL}^3 and so on. The estimated TOD for the different elements in the SC path (and the signal path afterwards) is 1800fs^3 at 800nm, which would stretch a 25fs pulse with a Gaussian spectrum to 26.2fs.

The geometry of a prism compressor is shown figure 5-13. The incidence angle θ_0 is chosen at Brewster angle, which also determines the apex angle α. This means that for s polarised light there is no reflectance. The Brewster configuration is technically only verified for a specific wavelength. Several materials were considered for the prisms. The amount of GDD added or removed depends on the distance between prisms L (see figure 5-13) and the insertion of each prism, l_1 and l_2. Usually, l_1 is as small as possible, the limit being the beam diameter, as this minimizes the amount of material on the optical path (and so the GDD added by material dispersion). The distance L is chosen so that it is possible to compensate for GDD for all wavelength in the tunability range, and the insertion l_2 is how the compressor is tuned. A mirror is used to send back the spatially dispersed beam on the same path so that the different components are recombined. The path cannot be exactly the same otherwise the input and output would not be separated. In practice the beams are separated in the vertical direction
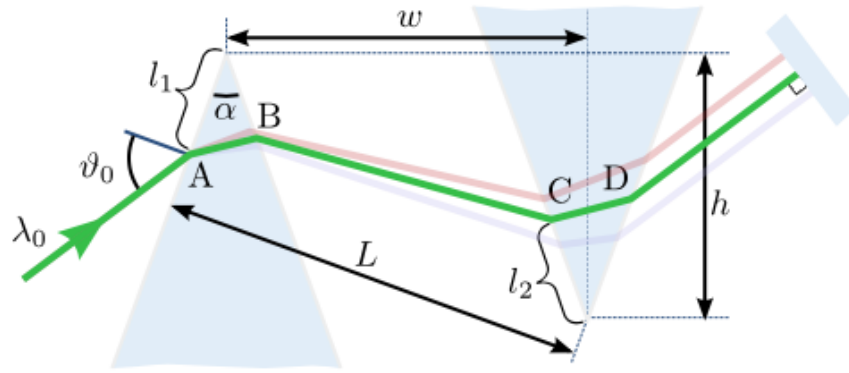
Figure 5-13: Geometry of a prism compressor [251]

The material of the prism determines the distance L and insertion l_2 that are necessary to compensate a given amount of dispersion. The material was chosen so that L is not too large (less than 20cm) and the insertion l_2 is between 1mm and 20mm (to stay within the prism and limit the amount of material on the path). The longer the wavelength, the shorter the insertion length. In the end, SF57 glass verified all those criteria.

Wavelength, nm	Pulse duration, fs	TL duration, fs
700	44	51
750	41	40
800	38	40
900	23	23
930	29	21

Table 5-5: Pulse duration measured by autocorrelation and TL duration of the pulse calculated from the signal spectrum.

Following the prism compressor, the pulse duration of the signal was measured by autocorrelation. Autocorrelation is not sufficient to retrieve the pulse shape or the phase of the pulse. However, the FWHM of the autocorrelation trace τ_{AC} provides a fast way to estimate the pulse FWHM duration τ, as for a Gaussian pulse the two are simply linked by $\tau_{AC} = \sqrt{2}\,\tau$. Here the pulse shape is not necessarily Gaussian but should be relatively similar if the pulse is nearly transform limited. More complex methods, such as FROG[183], SPIDER [92] or Dispersion scan[91] for instance, but

those require more complex optical schemes and would not be well adapted to the measurements of several pulses with different central wavelength. The phase of the signal pulse is also irrelevant to Multi-photon microscopy, as all second order interactions inside the sample are well within the low efficiency approximation. The measured pulse duration as well as the calculated TL pulse duration from the spectrum of the signal are listed table 5-5.

The pulse duration of the signal after compression is very close to the TL duration calculated from the spectrum. In fact, at 700nm and at 800nm the pulse duration seems to be shorter than the TL duration. This is not physically possible, but it is likely that the spectrum in both those cases during the autocorrelation measurement was slightly different from the measured spectrum (figure 5-10). The duration calculated by Autocorrelation can also be slightly different from the true FWHM pulse duration, as the formula is valid only for Gaussian pulses. The TL duration is also calculated by cutting the noise in the spectrum (which can reduce the TL duration significantly) and it is possible that very weak components of the spectrum are cut also.

The compressed duration of the pulse is below 50fs for all wavelength considered, which was the initial objective. For 900nm central wavelength the pulse duration is especially short due to the extremely large bandwidth. Indeed, the material dispersion is less for the longer wavelength, because the zero-dispersion wavelength of optical glasses and the crystals we used (LBO and YAG) are between 1 and 2µm. The prism compressor also removes a certain amount of TOD. At 900nm for a 17cm distance L between the prisms, I calculated that an insertion l_2 of about 20mm was necessary to compensate for the GDD, and the estimated TOD removed by the prism compressor is $6500fs^3$. However, there can be some variations as the final prism configuration is not exactly the same as in the model. This means the final TOD should be around $-5000fs^3$. This is not completely neglectable for such a large bandwidth, but the effect is not very large either from Table 5.5.

5.2.8 Comparison with the current MPM source

Properties	Current	OPA
Central wavelength λ (nm)	1030	980 to 700
Pulse duration τ (fs)	200	25 to 45
Repetition rate f (kHz)	200	1000
Maximum pulse energy E (nJ)	500*	150
Beam quality M^2	<1.2	<1.25

Table 5-6. Comparison between the OPA system described in this chapter and the femtosecond laser previously used as the source for our Multi-Photon Microscope [36]. *The maximum pulse energy is to prevent damage to the microscope objective.

The previous laser source was a 200fs laser [36], and its properties are listed table 5-6 along with the properties of the output of the OPA. The OPA provides tunability of the central wavelength between 980 and 700nm, with a pulse duration as short as 25fs at 900nm. The repetition rate can also be higher (though it can also be reduced easily by the pulse picker in the Femtolux-3 laser), and beam quality is comparable in both cases. The pulse energy is significantly lower, which can be a problem as the second harmonic signal depends quadratically on the pulse energy. If it is possible to use the maximum pulse energy and maximum repetition rate of both sources the theoretical second harmonic signal ratio (for the OPA output at 900nm) is:

$$\frac{S_{OPA}}{S_0} = \frac{E_{OPA}^2 \, f_{OPA} \, \tau_0}{E_0^2 \, f_0 \, \tau_{OPA}} = 3.6 \qquad (5.3)$$

Where 0 stands the original laser source, S is the signal from the microscope, E the pulse energy, f the repetition rate and τ is the pulse duration. If it is possible to use both system to the maximum settings the new source should therefore provide 3.6 times higher 2 photon signal for the same sample over the same integration time.

5.3 MULTIPHOTON MICROSCOPY WITH THE OPA SOURCE

5.3.1   Integration of the OPA source to the Microscope
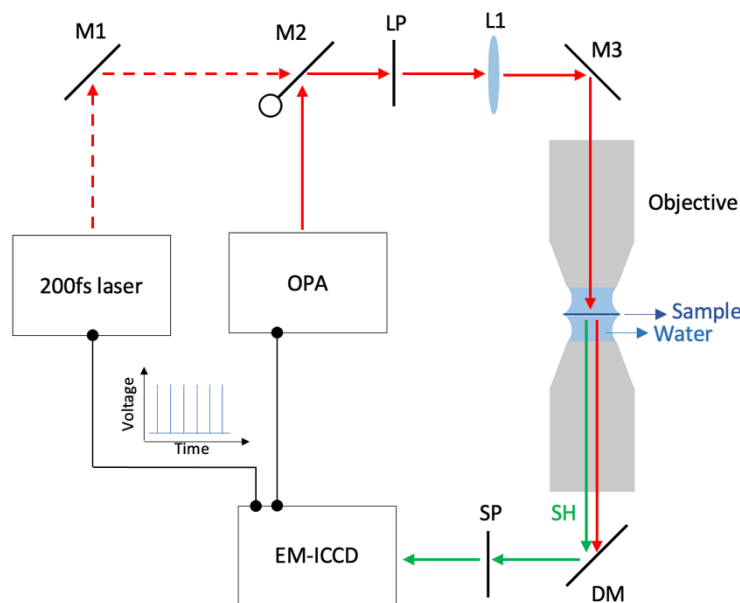
Figure 5-14: Simplified optical scheme of the multiphoton microscope and the two possible laser sources. LP = Long pass filter; SP = Short pass filter; M = Mirror; DM= Dichroic mirror.

The optical scheme of the microscope with the 2 possible sources is shown figure 5-14. The OPA or the previous system can be used alternatively thanks to a flipping mirror (M2). Unlike a confocal microscope, a lens is placed before the objective so that there is wide field illumination of the sample. Because the new system is much more sensitive to dispersion than the original source (which has a shorter bandwidth), the mirrors were replaced by low GDD versions. The different samples we used need to be in water. Depending on the type of sample, second harmonic or 2 photon fluorescence is generated. The laser source is filtered out with a dichroic mirror and a filter, before the signal is collected with an electron multiplying intensified CCD camera (EM-ICCD) [252]. One last important aspect is the acquisition window: it is beneficial to limit the acquisition time around a pulse to improve the signal to noise ratio (SNR). Indeed, with repetition rates of 200kHz or 1MHz and pulse duration of a few hundred fs or less, there should be no signal most of the time. The camera is synchronized with the laser source, with a delay adjusted to compensate for the optical path and the length of the electric cables. Thus, the electronic shutter can then isolate

the region around each pulse (gating within 500ps for this camera). Initially there were issues with the repletion rate of the OPA and we had to use it only at 330kHz repetition rate. Later on, this was fixed and the full repletion rate of 1MHz was used. Further, the repletion rate used is mentioned along with the images.

The intensifier of the camera is required so that very low second harmonic or 2 photon fluorescence signal can be detected. However, the quantum efficiency (QE) of the intensifier is wavelength dependent (figure 5-15). The peak of efficiency is around 460nm, meaning that the ideal source for second harmonic microscopy is 920nm. The efficiency remains high between 430 and 600nm, a window which includes the second harmonic of the original source central wavelength. In practice, it means we cannot use wavelength shorter than 850nm for second harmonic microscopy without a large loss of SNR. The tunability range between 700 and 850nm can still be used for 2 photon microscopy. In the following, the central wavelength is set around 950nm to maximize the QE of the intensifier. The slightly lower QE for the original source is accounted for in the comparisons.
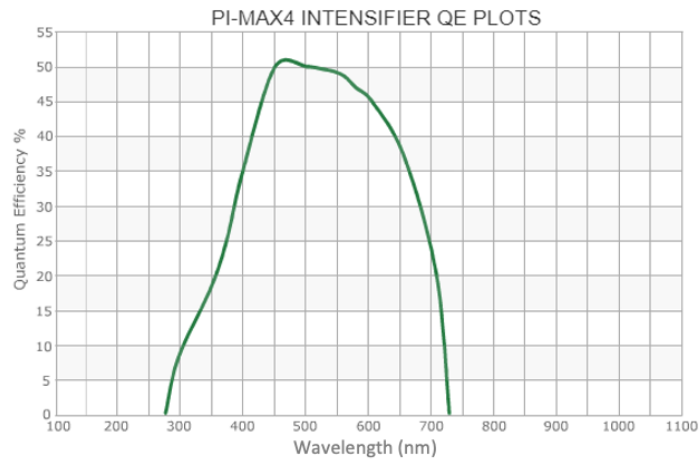
Figure 5-15: Quantum efficiency of the PI-Max4 intensifier used in experiments [252]

The dispersion introduced by the objective is significant, meaning that before and after the objective the pulse duration is much longer. One of limits of this microscope scheme is focusing inside the objective, which can generate white light and damage the optical glass. Since the peak intensity will be reduced for a longer pulse, the dispersion can play a positive role here and reduce damage. The dispersion out of the OPA can be adjusted simply by adjusting the prism compressor.

Here, it is not practical to measure the pulse autocorrelation after the objective. However, the output second harmonic (or two photon fluorescence) signal will be stronger for shorter pulses, so the prism compressor can be adjusted by maximizing the throughput.

5.3.2 Imaging with the OPA light source

5.3.2.1 Nanoparticles
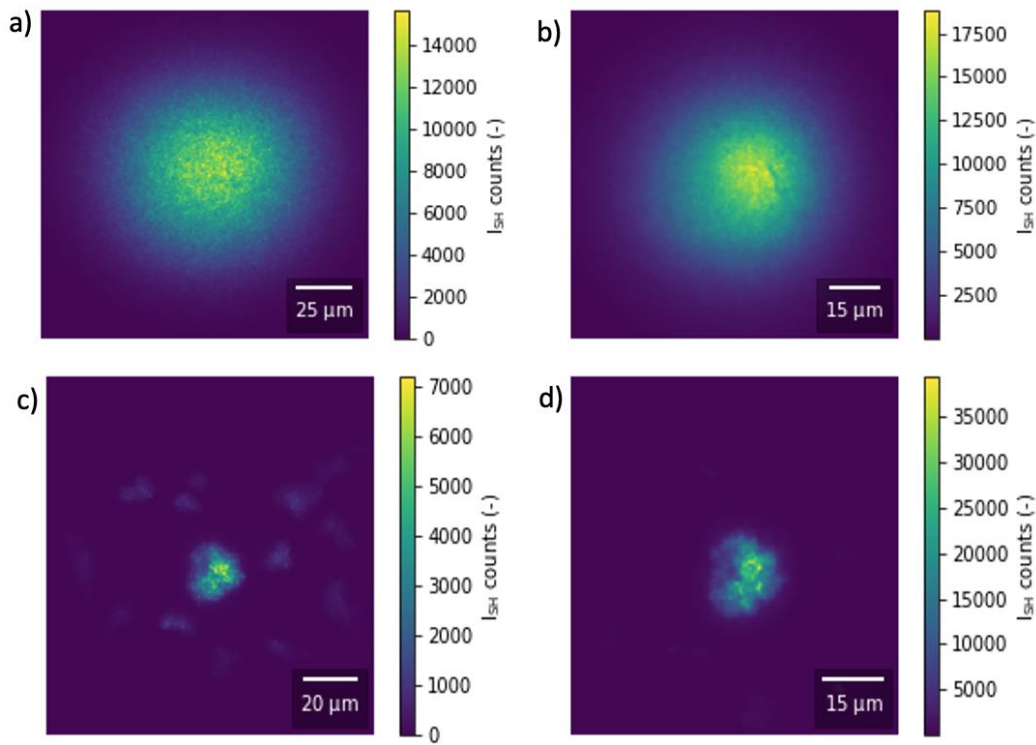
Figure 5-16: SH microscopy image of a suspension of $BaTiO_3$ nanoparticles, using the previous light source (a) and c)) or the OPA (b) and d)) laser source. For a) and b) there is a relatively homogenous distribution of nanoparticles, but the images are not centered on the same point. For c) and d), the field is centered on a specific cluster of nanoparticles. Acquisition time is 5ms, 330kHz repetition rate for the OPA (~150nJ pulse energy), and 200kHz for the original source (~500nJ pulse energy).

Second Harmonic microscopy is sensitive to non-centrosymmetric media and can be used to image specific biological tissues without markers such as collagen [11], [185], micro-tubules in neurons [13], [253], [254]… However, when the SH signal is too weak (for analysis of dynamic processes where a long acquisition time is not possible for instance) or if what we need to image is

centrosymmetric, markers can be used[19], [255], [256]. One such marker is $BaTiO_3$ nanoparticles [19]. Here we can use such nanoparticles to compare the SH signal from the 2 different laser sources.

The SH images for $BaTiO_3$ nanoparticles are shown figure 5-16. At first glance at images a) and b) we can see that the beam diameters are different. Comparing the two sources with different beam diameters would be unfair as this just depends on the collimating condition of each laser beam before the microscope. It would be possible to adjust the beam diameter out of the OPA with a telescope if we need a larger or smaller field in the focal plane. As can be expected we observe a Gaussian beam. Here the low conversion efficiency approximation is definitely valid: Depletion of the fundamental is neglectable. Therefore, the SH fluence depends quadratically on the fundamental fluence, and the beam waist diameter of the fundamental is $\sqrt{2}$ times that of the observed SH. The HRS images let us calculate the beam diameter of the SH, by fitting the data. In this case the beam radius at $1/e^2$ were 36µm and 50µm for the OPA and pre-existing sources respectively. For a fair comparison of the 2 sources, we will compensate for the beam diameter difference (using the low efficiency approximation).

Images a) and b) are not suitable to compare the throughput of second harmonic microscopy, because we do not know the exact concentration of nanoparticles in a specific zone, nor were the 2 beams (from the original source and the OPA) were centered on the same point. For this, we needed to illuminate a specific cluster of nanoparticles (images c) and d)). Here we can directly compare the SH signal in a small region around the center of the cluster.

5.3.2.2 Glass micro-pipette
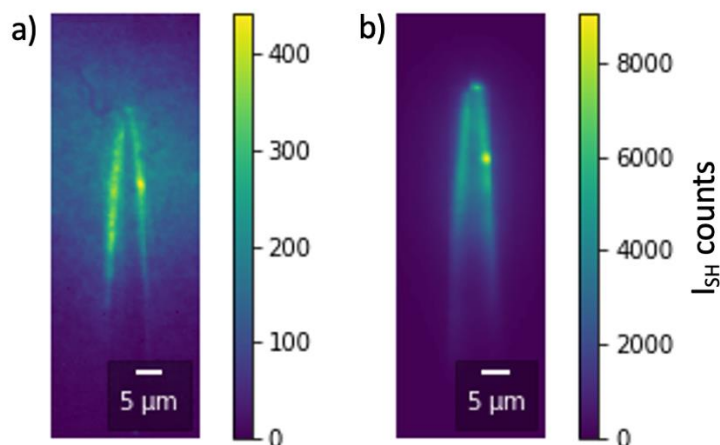
Figure 5-17: SH microscopy images of the tip of a glass micropipette with the original source (a) and with the OPA source (b). Image acquisition time 40ms, 330kHz repetition rate of OPA (~150nJ pulse energy), 200kHz for the original source (~290nJ pulse energy), single pulse peak fluence is the same in both cases.

SH microscopy is sensitive to interfaces because there is a break of centro-symmetry. Here we imaged a glass micropipette immerged in water. There will be SH signal at the interface and in the water close to it because the water molecules tend to orient themselves near the interface. Such a system can also be used to probe the effect of electric potential differences inside and outside the micropipette [36] for instance.

SH microscopy images of a glass micropipette are presented figure 5.17. Here the original source power was adjusted so that the peak fluence is the same. We can easily observe a very large increase in SH signal when using the OPA source. Part of this is due to the higher repletion rate, but mostly to the shorter pulses. By looking at the signal near the peak we can compare both sources. Other acquisitions were also made using the maximum power of the original source.

5.3.2.3 Giant Unilamellar Vesicles

One of the most prevalent interfaces in organic tissues is the cell membrane. Investigation of the cell membrane with second harmonic microscopy is thus particularly interesting, with for instance novel results on ion channels[257]. Giant Unilamellar Vesicles (GUVs) are defined as a vesicle

made of a lipid bilayer with a size of more than 1µm, making them very similar to a (simplified) cell membrane. GUVs are often investigated with 2 photon fluorescence [258]–[260] or even with SH markers [9], [261], but to our knowledge there is no published results on marker free SH microscopy images of GUVs, as the signal is extremely weak. Here we performed both 2 photon fluorescence imaging and label free SH imaging of GUVs.
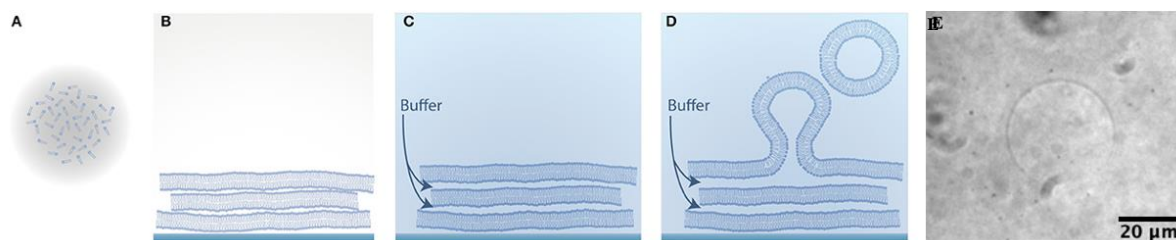
Figure 5-18: Schematic representation of vesicle forming (from A to D) [262] and white light image of a GUV in the focal plane of the multi-photon microscope (E). Initially lipds are in a suspension in a solvent (A). When it evaporates, lipid bilayers form (B), and when the bilayers are rehydrated (C), vesicles start swelling due (D) to osmotic pressure.

The process of GUVs formation is explained figure 5.18 [262]. At the start (A), a marker (Nile Red [263]) for 2 photon fluorescence can be introduced. The rehydration of the lipid bilayers (C) takes place in a sucrose solution. Later on, some of the sucrose solution containing GUVs was transferred in a glucose solution with $CaCl_2$. Because of the difference of density, the GUVs will fell at the bottom of the sample and we then imaged them (image E).
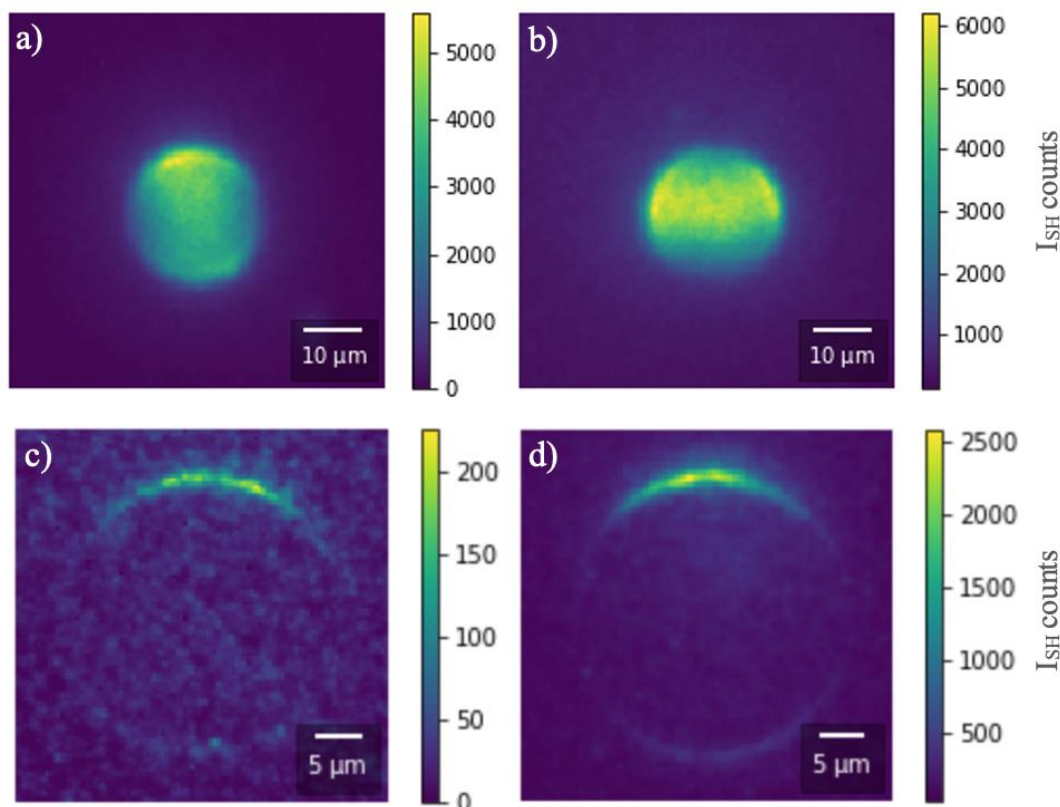
Figure 5-19: a) Image of a GUV with 2photon fluorescence, in SS polarization, with the original laser source (10ms acquisition, 200kHz repetition rate) b) 2PF image of the same GUV in PP polarization with the OPA source (10ms acquisition, 331kHz repetition rate) c) SH image (marker free) of a GUV with the original source, SS polarization (1s acquisition, 200kHz repetition rate) d) Same as c) but with the OPA source (1s acquisition, 331kHz repetition rate). The fluence was the same for both sources.

The GUVs were successfully imaged in 2PF and SH with each laser source. Figure 5.19 we observe that the 2PF images collect light from the whole GUV, whereas only the sides of the GUV are visible in SH images. This is because the propagation direction needs to be orthogonal to the surface for maximum SH conversion efficiency, whereas there is no such constraint for 2 photon fluorescence. The SH signal is enhanced by the presence of different ionic potentials inside and outside the GUVs (due to the $CaCl_2$ solution). Thanks to the marker, the signal is also much stronger for 2PF (acquisition time of only 10ms), whereas the SH images required a much longer acquisition time. The SH signal is also polarization sensitive: only the top and bottom of the GUV is visible in each image, where the polarization direction is orthogonal to the surface. It was possible to acquire marker free SH images of GUVs even with the original source, but the new source significantly improves the SNR, and it would be possible to acquire images much faster

(especially since here the repetition rate was only 331kHz, but we later found how to use the full 1MHz repetition rate).

5.3.3 Discussion

The tunable OPA was used as a light source in several multiphoton microscopy experiments and compared to the existing commercial solution. Because of the limitations of the camera the tunability range was not really used yet, though it might prove useful for some 2PF experiments. The main advantage of the OPA is providing an extremely short pulse (down to 25fs) compared to the 200fs pulse duration of the original laser source. This is not the first time sub 100 fs pulses have been used for Multi-photon microscopy[37], [264]–[266], with in some cases pulses as short as 10fs [265], [266]. One approach is to employ spatio-temporal focusing [37], [264], meaning use gratings to separate the different wavelength spatially and reconstruct the pulse only in the focal plane of the microscope. Spatiotemporal focusing can limit the photodamage and photobleaching out of the focal plane, but it is better adapted to confocal microscopy rather than wide field microscopy. Here there is no large spatial dispersion inside the microscope, but the pulse will be stretched by material dispersion before and after the sample, which also helps limit the damage. A pulse duration around 30fs is quite favorable, for the signal should be strongly enhanced at a given fluence, yet the complexity of the OPA remains reasonable. For sub 10fs pulses, the higher order dispersion terms are no longer neglectable and need to be compensated (meaning the prism compressor is no longer sufficient), and because those are few cycle pulses, carrier envelope phase becomes relevant [267], [268]. The OPA we designed is a good compromise between very complex (and pricey) solutions and commercial systems. Also, the bandwidth of ultrashort pulses can become larger than the excitation bandwidth of two photon fluorescence. Here the original source is better adapted for the Nile Red marker (central excitation wavelength ~500nm [263]), for instance. This is less of a problem for SH microscopy, where the $\chi^{(2)}$ elements only weakly depend on wavelength and phase-mismatch is neglectable because samples are thin.

A theoretical gain from using the OPA source versus the previous ultrashort laser source. Two situations are relevant: when fluence (per pulse) is the same in both cases, set at the maximum output of the OPA around 940nm central wavelength, and when we use both system at the

142

maximum possible output (500nJ pulse energy for the original system). In that case the beam diameters should be the same with both sources, so that the comparison is fair. Since this is not the case in practice, the ratio of beam diameters (measured in HRS or nanoparticles experiments) is used to compensate. The theoretical gain at the same fluence is:

$$G_{Fl} = \frac{f_{OPA}\,\tau_0}{f_0\,\tau_{OPA}} \approx 40 \tag{5.4}$$

Here f is the repetition rate for the OPA or original system (noted 0) and τ the pulse duration. If we consider that both beam diameters are the same, the gain at maximum operating parameters is:

$$G_{Max} = \frac{f_{OPA}\,\tau_0 E_{OPA}^2}{f_0\,\tau_{OPA}E_0^2} \approx 3.6 \tag{5.5}$$

Where E is the pulse energy for the OPA or original source respectively. In practice the gain is calculated by measuring the average SH intensity on a small area around the signal peak (in figures 5.15, 5.16, 5.17 and 5.19) when the fluence is the same for both pulses for G_{Fl} (calculated by using the pulse energy and the beam diameters measured experimentally). For G_{Max}, the same is done at maximum output but the square of the diameter ratio is used to compensate the difference in diameters. The calculated gains are listed in table 5.7. All gains were calculated for a 1MHz repetition rate of the Femtolux-3 laser, even though some of the data was acquired at a lower repetition rate. We tested that there was no damage when using the full 1MHz repetition rate. For each experimental situation, the gain is averaged on 4 or 5 separate images.

Experiment	Signal gain at maximum power, G_{Max}	Signal gain at the same fluence, G_{Fl}
Nanoparticles, Cluster 1	2.5	27.2
Nanoparticles, Cluster 2	2.3	25.5
Nanoparticles, Cluster 3	2.7	30
Glass-Water interface	3.1	34.4
GUVs SH	2.1	23.3
Theory	3.6	40

Table 5-7. Signal increase when using the OPA laser source when compared to the original laser source. Theoretical gain calculated for a 25fs pulse with 1MHz repetition rate and 150mW for the OPA (see table 5-6 for original source parameters)

There is a very large gain by using the OPA source at the same fluence as the 200fs laser source (more than 23 times in every experiment, and up to 34 times). Unfortunately, the pulse energy at the output of the OPA is significantly lower than what we can use with the original source, meaning the gain at maximum throughput is smaller, but still significant. Importantly, no photodamage to the objective or white light generation in water was observed with the OPA source, which is the main limit with using the original source. As white light generation is intensity related, and the mechanisms of damage for sub ps pulses also depend on the pulse duration [111], it is possible that there would be damage if we were able to use a pulse energy as high as the original source. The subject of photodamage with biological samples is even more complex [38], and also depends on the peak intensity (not only the fluence). Globally, the gain is close to what we can expect from theory, but a little smaller. This is likely due to high order dispersion and the pulse quality. Indeed, the different optical elements (especially the objective) add not only GDD (which is compensated by the prism compressor), but also third order dispersion (TOD) and higher order terms, which are not compensated. When there is TOD, some of the energy goes to smaller tailing or leading pulses (depending on the sign of the TOD), which will not generate much SH because their peaks are much lower. The pulse shape also becomes less Gaussian, meaning the SH conversion efficiency

decreases. Those effects are not completely neglectable, but only induce ~25% signal loss, from table 5.7 results. The OPA source performs as expected for the multi-photon microscope, leading to a significant signal to noise ratio gain.

5.4 CONCLUSION

We built an OPA system that provides wavelength tunability from 970 to 700nm, with pulse energy between 150 and 200nJ and 1MHz repetition rate and pulse duration between 25 and 50fs. The construction of the OPA involved several stages. First, for supercontinuum generation crystals, we selected YVO_4 and KGW as good candidates, as in both cases only about 300nJ pulse energy is required to achieve a stable supercontinuum, and the supercontinuum spectrum and spatial properties are appropriate to serve as seed for the OPA. Second, a SHG setup reaching 67% conversion efficiency was assembled. Third, the actual parametrical amplification was performed in a lithium tri-borate crystal, chosen according to simulations. Finally, the compression of the pulse was insured by a two prisms compressor. A second stage of OPA was also tested, and while it significantly increases the pulse energy (from 150 to 250nJ at 900nm), it comes at the expense of increasing the pulse duration. The main limiting factor for the signal duration (for 1 stage or 2 stage OPA) was determined to be the accumulated group delay dispersion on the supercontinuum path.

After testing the properties of the output of the OPA, it could finally be integrated with the microscope. The optical scheme was set so that we could easily switch between the OPA and the existing femtosecond laser source. Several samples, including pure water, glass-water interface around a micropipette, nanoparticles and giant unilamellar vesicles, were imaged using the two laser sources successively, and the throughput was ordered. To make the comparison fair, it accounts for the difference of beam diameters in the sample. The beam diameter was measured using a dense distribution of nanoparticles. Of particular interest was the markerless second harmonic imaging of giant unilamellar vesicles and the detection of hyper Rayleigh scattering, which is only made possible by the high peak power of the laser source and the high sensitivity of the camera. Importantly, no damage was observed even when using the maximum power available with the OPA.

Optical parametrical amplification of a few tens of femtosecond pulses was experimentally proven to make a very suitable laser source for two-photon microscopy. For second harmonic microscopy it provides a much shorter pulse duration than commercially available laser systems, meaning the throughput can be increased while keeping photodamage low. For two photon excitation fluorescence, the tunability is an asset as the wavelength can be centred on the two-photon excitation spectrum. However, because the laser spectrum is very broadband (between 20 and 80nm bandwidth, depending on the central wavelength), it might be broader than the excitation spectrum, which can limit the gain from using such short pulses. It is possible to use even shorter pulse duration (which would improve second harmonic throughput), but compared to few cycle laser systems, this OPA is a simpler alternative, which does not require compensation of high order dispersion or concerns over carrier envelope phase [268].

This system could be adapted relatively easily to a different wide filed multiphoton microscope. Here, the idler was simply removed, because the camera of the microscope cannot be used on the range of wavelength that it covers (1.1 to $2\mu m$). It could be compressed, and its duration should be similar to that of the signal, though the power will be lower (from 50 to 150nJ). The idler could be used for second harmonic microscopy, especially since a wavelength of $1.4\mu m$ would provide maximum penetration depth in tissues an still good second harmonic transmission [269]. For sum frequency generation microscopy, the signal and idler could be used together, or one of them could be used along with a portion of the original laser source. With a higher power laser source (Ekspla is currently developing a 30W version of the Femtolux laser), the output power would be higher. Alternatively, a second stage of OPA was proven to improve the total conversion efficiency, but if we want to maintain sub 50fs pulse duration, the pulse needs to be partially compressed between the two stages, or some of the optical elements would need to be changed so that there is less material dispersion on the signal path.

Summary and Outlook

Summary

In this thesis we used nonlinear crystals to generate new wavelengths from a source femtosecond laser. The parametrical amplification laser so created can then be used for multi-photon microscopy.

In chapter 2, we presented a novel simulation tool we created for second order interactions in nonlinear crystals. This tool, called "Wavemixer" can simulate second harmonic generation, sum frequency generation or parametrical amplification for a wide variety of crystals and configurations. It accounts for linear propagation in the crystal, second order interaction and self and cross phase modulation. The simulation results were often the basis of the work presented in the next chapters.

In chapter 3, we studied the effect of dispersion for efficient second harmonic generation in nonlinear crystal. We showed that dispersion of the fundamental pulse can cause back conversion early on in the crystal and so drastically reduce the conversion efficiency. The sensitivity of both the conversion efficiency and the beam spatial properties depends on the focusing conditions and the length of the crystal. The stretching of the pulse due to dispersion cannot on its own account for the second harmonic behaviour. The sensitivity can be reduced by using short crystals and tight focusing, but photodamage and Kerr effect limit the applicable range. A good knowledge of the fundamental spectral phase, even if the pulse is well-compressed, is important for the choice of physical parameters.

In chapter 4, we showed how a new transverse parameter, a temperature gradient in the crystal, can be used to improve the performance of second harmonic generation, in particular for chirped pulses as were studied in the previous chapter. A similar idea is applied for chirped periodically polarized crystals, but here the phase mismatch changes continuously instead of discretely. When a temperature gradient is applied in the propagation direction of the crystal, different wavelengths are phasematched in different positions in the crystal, and chirp temporally separates the different

spectral components of the fundamental. We demonstrate by simulations and by experiments that this can lead to higher conversion efficiency and better spatial properties of the second harmonic, but also impact the bandwidth and pulse duration.

In chapter 5, we explain the process of actually building a parametrical amplification setup for a femtosecond fibre laser and the testing of this new source on a multi-photon microscope. The parametrical amplification setup is made of several parts. First, supercontinuum generation in a bulk crystal lets us generate a large bandwidth in the near infrared and visible from part of the source laser power, but with very small (a few nanojoules) pulse energy. Second, the rest of the source laser is frequency doubled in a nonlinear crystal. Third, the supercontinuum and second harmonic are spatially and temporally overlapped in a second nonlinear crystal, leading to amplification of a specific wavelength range (depending on the angle of the crystal and the temporal overlap). Finally, the amplified signal is compressed in a prism compressor. Starting from a 260fs fibre laser with 3W average output power at 1MHz repetition rate, this process provides us with a tunability range from 980 to 700nm, with pulse energy between 150 and 200nJ and pulse duration between 25 and 50fs. This source was compared to an existing laser source with a multi-photon microscope. Several second harmonic images were acquired, and the throughput gain matches with what can be expected from theory. This shows that femtosecond fibre lasers combined with parametrical amplification are a suitable and cost-efficient source of illumination in wide-field multiphoton microscopy.

Outlook

The initial motivation of this project was the design of a new tunable femtosecond source for wide-field multi-photon microscopy. The planned source was indeed delivered and tested and performed within expectations. The proof of concept was thus realised. The parametrical amplification source we built can be considered an early prototype but is still quite far from a commercial system. For this, miniaturisation and further study of the stability would be required. Also, the tuning of the current system is relatively complex and would likely need to be automated. Yet this is not the only result of this project: The simulation tool which was created to better design and optimize the parametric amplification is very flexible and was already used for several other projects. It also lets us investigate the effect of different parameters as we did for chapter 3 and 4. The use of temperature gradients already produced interesting results when applied to second harmonic generation and could likely be extended to sum frequency generation or parametrical amplification, in particular for optical parametrical chirped pulse amplification.

The increase in throughput from the wide field multiphoton microscope should also lead to improvement in image quality and the increase in repetition rate, which we showed did not cause any photodamage so far, is useful for imaging dynamic processes. For two photon excitation fluorescence microscopy, the tunability should be more relevant but the advantage of a shorter pulse duration might be somewhat negated if the excitation bandwidth of the fluorescent markers is too narrow.

List of publications

The present thesis is based on the following publications/manuscripts:

Chapter 3:

P.-M. Dansette, R. Burokas, L. Veselis, A. Zaukevičius, A. Michailovas, and N. Rusteika, "Peculiarities of Second Harmonic Generation with Chirped Femtosecond Pulses at High Conversion Efficiency," *Opt. Commun.*, vol. 455, 2020.

Chapter 4:

P.-M. Dansette, M. Eremchev, and A. Michailovas, "Continuous compensation of the phase mismatch by using temperature gradients for second harmonic generation," *Opt. Commun.*, vol. 484, p. 126687, 2021.

Chapter 5 :

K. Madeikis, P.-M. Dansette, T. Bartulevicius, L. Veselis, R. Jutas, M. Eremchev, R. Danilevicius, V. Girdauskas, A. Michailovas, "Investigation of materials for supercontinuum generation for nonlinear amplification at 1MHz repetition rate", *submitted to Results in Optics* (17/12/2020)

Bibliography

[1]   R. Hellwarth and P. Christensen, "Nonlinear Optical Microscope Using Second Harmonic Generation," *Appl. Opt.*, 1975, doi: 10.1364/ao.14.000247.

[2]   W. Denk, J. H. Strickler, and W. W. Webb, "Two-photon laser scanning fluorescence microscopy," *Science (80-.).*, 1990, doi: 10.1126/science.2321027.

[3]   Y. Barad, H. Eisenberg, M. Horowitz, and Y. Silberberg, "Nonlinear scanning laser microscopy by third harmonic generation," *Appl. Phys. Lett.*, 1997, doi: 10.1063/1.118442.

[4]   M. J. Farrar, F. W. Wise, J. R. Fetcho, and C. B. Schaffer, "In vivo imaging of myelin in the vertebrate central nervous system using third harmonic generation microscopy," *Biophys. J.*, 2011, doi: 10.1016/j.bpj.2011.01.031.

[5]   R. W. Boyd, "Nonlinear Optics," in *Nonlinear Optics*, 3rd ed., 2008, pp. 1–65.

[6]   K. A. Cimatu and S. Baldelli, "Chemical microscopy of surfaces by sum frequency generation imaging," *J. Phys. Chem. C*, 2009, doi: 10.1021/jp904015s.

[7]   Y. Fu, H. Wang, R. Shi, and J. X. Cheng, "Second harmonic and sum frequency generation imaging of fibrous astroglial filaments in ex vivo spinal tissues," *Biophys. J.*, 2007, doi: 10.1529/biophysj.106.089011.

[8]   V. Raghunathan, Y. Han, O. Korth, N.-H. Ge, and E. O. Potma, "Rapid vibrational imaging with sum frequency generation microscopy," *Opt. Lett.*, 2011, doi: 10.1364/ol.36.003891.

[9]   L. Moreaux, O. Sandre, and J. Mertz, "Membrane imaging by second-harmonic generation microscopy," *J. Opt. Soc. Am. B*, 2000, doi: 10.1364/JOSAB.17.001685.

[10]   O. B. Tarun, M. Y. Eremchev, and S. Roke, "Interaction of Oil and Lipids in Freestanding Lipid Bilayer Membranes Studied with Label-Free High-Throughput Wide-Field Second-Harmonic Microscopy," *Langmuir*, 2018, doi: 10.1021/acs.langmuir.8b01790.

[11]   E. Brown *et al.*, "Dynamic imaging of collagen and its modulation in tumors in vivo using second-harmonic generation," *Nat. Med.*, 2003, doi: 10.1038/nm879.

[12]   S. Roth and I. Freund, "Second harmonic generation in collagen," *J. Chem. Phys.*, 1979,

doi: 10.1063/1.437677.

[13]   D. A. Dombeck, K. A. Kasischke, H. D. Vishwasrao, M. Ingelsson, B. T. Hyman, and W. W. Webb, "Uniform polarity microtubule assemblies imaged in native brain tissue by second-harmonic generation microscopy," *Proc. Natl. Acad. Sci. U. S. A.*, 2003, doi: 10.1073/pnas.0731953100.

[14]   L. Sacconi, D. A. Dombeck, and W. W. Webb, "Overcoming photodamage in second-harmonic generation microscopy: Real-time optical recording of neuronal action potentials," *Proc. Natl. Acad. Sci.*, 2006, doi: 10.1073/pnas.0511338103.

[15]   D. A. Dombeck, M. Blanchard-Desce, and W. W. Webb, "Optical Recording of Action Potentials with Second-Harmonic Generation Microscopy," *J. Neurosci.*, 2004, doi: 10.1523/JNEUROSCI.4840-03.2004.

[16]   A. Lahiani, E. Klaiman, and O. Grimm, "Enabling histopathological annotations on immunofluorescent images through virtualization of hematoxylin and eosin," *J. Pathol. Inform.*, 2018, doi: 10.4103/jpi.jpi_61_17.

[17]   W. R. Zipfel, R. M. Williams, R. Christiet, A. Y. Nikitin, B. T. Hyman, and W. W. Webb, "Live tissue intrinsic emission microscopy using multiphoton-excited native fluorescence and second harmonic generation," *Proc. Natl. Acad. Sci. U. S. A.*, 2003, doi: 10.1073/pnas.0832308100.

[18]   M. J. Huttunen *et al.*, "Automated classification of multiphoton microscopy images of ovarian tissue using deep learning," *J. Biomed. Opt.*, 2018, doi: 10.1117/1.jbo.23.6.066002.

[19]   C. Macias-Romero *et al.*, "Probing rotational and translational diffusion of nanodoublers in living cells on microsecond time scales," *Nano Lett.*, 2014, doi: 10.1021/nl500356u.

[20]   A. M. Smith, M. C. Mancini, and S. Nie, "Bioimaging: Second window for in vivo imaging," *Nature Nanotechnology*. 2009, doi: 10.1038/nnano.2009.326.

[21]   A. T. Yeh, N. Nassif, A. Zoumi, and B. J. Tromberg, "Selective corneal imaging using combined second-harmonic generation and two-photon excited fluorescence," *Opt. Lett.*, 2002, doi: 10.1364/ol.27.002082.

[22]   S. Mulligan and B. MacVicar, "Two-photon fluorescence microscopy: basic principles,

advantages and risks," *Mod. Res. Educ. Top. Microsc.*, 2007.

[23]   ThermoFisher, "Fluorophore Selection."

https://www.thermofisher.com/lt/en/home/life-science/cell-analysis/fluorophores.html

(accessed Dec. 20, 2020).

[24]   G. H. Patterson and D. W. Piston, "Photobleaching in two-photon excitation microscopy,"

Biophys. J., 2000, doi: 10.1016/S0006-3495(00)76762-2.

[25]   E. Gratton, "Fluorescence lifetime imaging for the two-photon microscope: time-domain

and frequency-domain methods," *J. Biomed. Opt.*, 2003, doi: 10.1117/1.1586704.

[26]   R. Yasuda, C. D. Harvey, H. Zhong, A. Sobczyk, L. Van Aelst, and K. Svoboda,

"Supersensitive Ras activation in dendrites and spines revealed by two-photon

fluorescence lifetime imaging," *Nat. Neurosci.*, 2006, doi: 10.1038/nn1635.

[27]   K. M. Hanson, M. J. Behne, N. P. Barry, T. M. Mauro, E. Gratton, and R. M. Clegg, "Two-

photon fluorescence lifetime imaging of the skin stratum corneum pH gradient," *Biophys.

J.*, 2002, doi: 10.1016/S0006-3495(02)73936-2.

[28]   J. B. Ding, K. T. Takasaki, and B. L. Sabatini, "Supraresolution Imaging in Brain Slices using

Stimulated-Emission Depletion Two-Photon Laser Scanning Microscopy," *Neuron*, 2009,

doi: 10.1016/j.neuron.2009.07.011.

[29]   P. Bianchini, B. Harke, S. Galiani, G. Vicidomini, and A. Diaspro, "Single-wavelength two-

photon excitation-stimulated emission depletion (SW2PE-STED) superresolution

imaging," *Proc. Natl. Acad. Sci. U. S. A.*, 2012, doi: 10.1073/pnas.1119129109.

[30]   Q. Li, S. S. H. Wu, and K. C. Chou, "Subdiffraction-limit two-photon fluorescence

microscopy for GFP-tagged cell imaging," *Biophys. J.*, 2009, doi:

10.1016/j.bpj.2009.09.038.

[31]   Q. Yu and A. A. Heikal, "Two-photon autofluorescence dynamics imaging reveals

sensitivity of intracellular NADH concentration and conformation to cell physiology at the

single-cell level," *J. Photochem. Photobiol. B Biol.*, 2009, doi:

10.1016/j.jphotobiol.2008.12.010.

[32]   W. Müller and J. A. Connor, "Dendritic spines as individual neuronal compartments for

synaptic Ca2+ responses," *Nature*, 1991, doi: 10.1038/354073a0.

[33] K. Ohki, S. Chung, Y. H. Ch'ng, P. Kara, and R. C. Reid, "Functional imaging with cellular resolution reveals precise microarchitecture in visual cortex," *Nature*. 2005, doi: 10.1038/nature03274.

[34] M. Minsky, "Microscopy Apparatus," *US Pat. 3013467*, 1957.

[35] C. Macias-Romero *et al.*, "High throughput second harmonic imaging for label-free biological applications," *Opt. Express*, vol. 22, no. 25, pp. 31102–31112, Dec. 2014, doi: 10.1364/oe.22.031102.

[36] C. Macias-Romero, I. Nahalka, H. I. Okur, and S. Roke, "Optical imaging of surface chemistry and dynamics in confinement," *Science (80-.).*, 2017, doi: 10.1126/science.aal4346.

[37] L.-C. Cheng *et al.*, "Spatiotemporal focusing-based widefield multiphoton microscopy for fast optical sectioning," *Opt. Express*, 2012, doi: 10.1364/oe.20.008939.

[38] C. Macias-Romero, V. Zubkovs, S. Wang, and S. Roke, "Wide-field medium-repetition-rate multiphoton microscopy reduces photodamage of living cells," *Biomed. Opt. Express*, 2016, doi: 10.1364/boe.7.001458.

[39] O. D. Therrien, B. Aubé, S. Pagès, P. De Koninck, and D. Côté, "Wide-field multiphoton imaging of cellular dynamics in thick tissue by temporal focusing and patterned illumination," *Biomed. Opt. Express*, 2011, doi: 10.1364/boe.2.000696.

[40] S. Bancelin *et al.*, "Fast interferometric second harmonic generation microscopy," *Biomed. Opt. Express*, 2016, doi: 10.1364/boe.7.000399.

[41] S. Yazdanfar, L. H. Laiho, and P. T. C. So, "Interferometric second harmonic generation microscopy," *Opt. Express*, 2004, doi: 10.1364/opex.12.002739.

[42] M. Rivard *et al.*, "Imaging the noncentrosymmetric structural organization of tendon with Interferometric Second Harmonic Generation microscopy," *J. Biophotonics*, 2014, doi: 10.1002/jbio.201300036.

[43] E. Y. S. Yew, H. Choi, D. Kim, and P. T. C. So, "Wide-field two-photon microscopy with temporal focusing and HiLo background rejection," in *Multiphoton Microscopy in the Biomedical Sciences XI*, 2011, doi: 10.1117/12.876068.

[44] T. H. Maiman, "Stimulated optical radiation in Ruby," *Nature*, 1960, doi:

10.1038/187493a0.

[45]   A. Einstein, "Zur Quantentheorie der Strahlung," *Phys. Z.*, vol. 18, pp. 121–128, 1917.

[46]   C. A. Wang and S. H. Groves, "New Materials for Diode Laser Pumping of Solid-State Lasers," *IEEE J. Quantum Electron.*, 1992, doi: 10.1109/3.135213.

[47]   D. Findlay and R. A. Clay, "The measurement of internal losses in 4-level lasers," *Phys. Lett.*, 1966, doi: 10.1016/0031-9163(66)90363-5.

[48]   M. B. Camargo, M. Kokta, R. D. Stultz, and M. Birnbaum, "Co^2+:YSGG saturable absorber Q switch for infrared erbium lasers," *Opt. Lett.*, 1995, doi: 10.1364/ol.20.000339.

[49]   M. C. Marconi, O. E. Martinez, and F. P. Diodati, "Q switching by self-focusing," *Opt. Lett.*, 1985, doi: 10.1364/ol.10.000402.

[50]   S. Schnell, V. G. Ostroumov, J. Breguet, W. A. R. Lüthy, H. P. Weber, and I. A. Shcherbakov, "Acoustooptic Q Switching of Erbium Lasers," *IEEE J. Quantum Electron.*, 1990, doi: 10.1109/3.108107.

[51]   J. Breguet, W. A. R. Luthy, H. P. Weber, A. F. Umyskov, and I. A. Shcherbakov, "Electrooptically Q-Switched 2.79 µm YSGG:Cr:Er Laser with an Intracavity Polarizer," *IEEE J. Quantum Electron.*, 1991, doi: 10.1109/3.78230.

[52]   W. E. Lamb, "Theory of an optical maser," *Phys. Rev.*, 1964, doi: 10.1103/PhysRev.134.A1429.

[53]   J. Kim, J. Koo, and J. H. Lee, "All-fiber acousto-optic modulator based on a cladding-etched optical fiber for active mode-locking," *Photonics Res.*, 2017, doi: 10.1364/prj.5.000391.

[54]   B. Pelz, M. K. Schott, and M. H. Niemz, "Electro-optic mode locking of an erbium:YAG laser with a rf resonance transformer," *Appl. Opt.*, 1994, doi: 10.1364/ao.33.000364.

[55]   T. J. Carrig, G. J. Wagner, A. Sennaroglu, J. Y. Jeong, and C. R. Pollock, "Mode-locked Cr^2+:ZnSe laser," *Opt. Lett.*, 2000, doi: 10.1364/ol.25.000168.

[56]   K. Yvind *et al.*, "Low-jitter and high-power 40-GHz all-active mode-locked lasers," *IEEE Photonics Technol. Lett.*, 2004, doi: 10.1109/LPT.2004.824634.

[57]   D. J. Kuizenga and A. E. Siegman, "FM and AM Mode Locking of the Homogeneous

Laser—Part I: Theory," *IEEE J. Quantum Electron.*, 1970, doi: 10.1109/JQE.1970.1076343.

[58] T. Matniyaz, "Free-space NPR mode locked erbium doped fiber laser based frequency comb for optical frequency measurement," 2018.

[59] U. Morgner *et al.*, "Sub-two-cycle pulses from a Kerr-lens mode-locked Ti:sapphire laser," *Opt. Lett.*, 1999, doi: 10.1364/ol.24.000411.

[60] S. V. Marchese *et al.*, "Femtosecond thin disk laser oscillator with pulse energy beyond the 10-microjoule level," *Opt. Express*, 2008, doi: 10.1364/oe.16.006397.

[61] R. Paschotta and U. Keller, "Passive mode locking with slow saturable absorbers," *Appl. Phys. B Lasers Opt.*, 2001, doi: 10.1007/s003400100726.

[62] F. Krausz, T. Brabec, and C. Spielmann, "Self-starting passive mode locking," *Opt. Lett.*, 1991, doi: 10.1364/ol.16.000235.

[63] C.-J. Chen, P. K. A. Wai, and C. R. Menyuk, "Self-starting of passively mode-locked lasers with fast saturable absorbers," *Opt. Lett.*, 1995, doi: 10.1364/ol.20.000350.

[64] M. F. Becker, D. J. Kuizenga, and A. E. Siegman, "Harmonic Mode Locking of the Nd:YAG Laser," *IEEE J. Quantum Electron.*, 1972, doi: 10.1109/JQE.1972.1077271.

[65] J. E. Murray and W. H. Lowdermilk, "ND : YAG regenerative amplifier," *J. Appl. Phys.*, 1980, doi: 10.1063/1.328194.

[66] J. N. Eckstein, A. I. Ferguson, and T. W. Hänsch, "High-resolution two-photon spectroscopy with picosecond light pulses," *Phys. Rev. Lett.*, 1978, doi: 10.1103/PhysRevLett.40.847.

[67] T. Udem, J. Reichert, R. Holzwarth, and T. W. Hänsch, "Absolute optical frequency measurement of the cesium D1 line with a mode-locked laser," *Phys. Rev. Lett.*, 1999, doi: 10.1103/PhysRevLett.82.3568.

[68] R. Holzwarth, T. Udem, T. W. Hänsch, J. C. Knight, W. J. Wadsworth, and P. S. J. Russell, "Optical frequency synthesizer for precision spectroscopy," *Phys. Rev. Lett.*, 2000, doi: 10.1103/PhysRevLett.85.2264.

[69] H. R. Telle, G. Steinmeyer, A. E. Dunlop, J. Stenger, D. H. Sutter, and U. Keller, "Carrier-envelope offset phase control: A novel concept for absolute optical frequency measurement and ultrashort pulse generation," *Appl. Phys. B Lasers Opt.*, 1999, doi:

10.1007/s003400050813.

[70] F. W. Helbing, G. Steinmeyer, and U. Keller, "Carrier-Envelope Offset Phase-Locking with Attosecond Timing Jitter," *IEEE J. Sel. Top. Quantum Electron.*, 2003, doi: 10.1109/JSTQE.2003.819104.

[71] C. Vozzi *et al.*, "High-energy, few-optical-cycle pulses at 1.5 μm with passive carrier-envelope phase stabilization," *Opt. Express*, 2006, doi: 10.1364/oe.14.010109.

[72] E. Moon, H. Wang, S. Gilbertson, H. Mashiko, M. Chini, and Z. Chang, "Advances in carrier-envelope phase stabilization of grating-based chirped-pulse amplifiers," *Laser Photonics Rev.*, 2010, doi: 10.1002/lpor.200810060.

[73] Z. Chang and P. Corkum, "Attosecond photon sources: the first decade and beyond [Invited]," *J. Opt. Soc. Am. B*, 2010, doi: 10.1364/josab.27.0000b9.

[74] D. Strickland and G. Mourou, "Compression of amplified chirped optical pulses," *Opt. Commun.*, 1985, doi: 10.1016/0030-4018(85)90120-8.

[75] C. Sauteret *et al.*, "Generation of 20-TW pulses of picosecond duration using chirped-pulse amplification in a Nd:glass power chain," *Opt. Lett.*, 1991, doi: 10.1364/ol.16.000238.

[76] F. Tavella, Y. Nomura, L. Veisz, V. Pervak, A. Marcinkevičius, and F. Krausz, "Dispersion management for a sub-10-fs, 10 TW optical parametric chirped-pulse amplifier," *Opt. Lett.*, 2007, doi: 10.1364/ol.32.002227.

[77] Z. Wang, C. Liu, Z. Shen, Q. Zhang, H. Teng, and Z. Wei, "High-contrast 116 PW Ti:sapphire laser system combined with a doubled chirped-pulse amplification scheme and a femtosecond optical-parametric amplifier," *Opt. Lett.*, 2011, doi: 10.1364/ol.36.003194.

[78] M. D. Perry *et al.*, "Petawatt laser pulses," *Opt. Lett.*, 1999, doi: 10.1364/ol.24.000160.

[79] W. Li *et al.*, "339 J high-energy Ti:sapphire chirped-pulse amplifier for 10 PW laser facility," *Opt. Lett.*, 2018, doi: 10.1364/ol.43.005681.

[80] E. Desurvire, J. R. Simpson, and P. C. Becker, "High-gain erbium-doped traveling-wave fiber amplifier," *Opt. Lett.*, 1987, doi: 10.1364/ol.12.000888.

[81] M. E. Fermann and I. Hartl, "Ultrafast fibre lasers," *Nature Photonics*. 2013, doi:

10.1038/nphoton.2013.280.

[82]   V. Cautaerts, D. J. Richardson, R. Paschotta, and D. C. Hanna, "Stretched pulse Yb^3+:silica fiber laser," *Opt. Lett.*, 1997, doi: 10.1364/ol.22.000316.

[83]   Q. Wang, J. Geng, Z. Jiang, T. Luo, and S. Jiang, "Mode-locked Tm-Ho-codoped fiber laser at 2.06 µm," *IEEE Photonics Technol. Lett.*, 2011, doi: 10.1109/LPT.2011.2123880.

[84]   X. Zhu and R. Jain, "Watt-level 100-nm Tunable 3-µM Fiber Laser," *IEEE Photonics Technol. Lett.*, 2008, doi: 10.1109/LPT.2007.912495.

[85]   V. I. Kruglov, B. C. Thomsen, J. M. Dudley, and J. D. Harvey, "Self-similar propagation and amplification of parabolic pulses in optical fibers," *Phys. Rev. Lett.*, 2000, doi: 10.1103/PhysRevLett.84.6010.

[86]   V. I. Kruglov and J. D. Harvey, "Asymptotically exact parabolic solutions of the generalized nonlinear Schrödinger equation with varying parameters," *J. Opt. Soc. Am. B*, 2006, doi: 10.1364/josab.23.002541.

[87]   J. A. Armstrong, "Measurement of picosecond laser pulse widths," *Appl. Phys. Lett.*, 1967, doi: 10.1063/1.1754787.

[88]   J. Etchepare, G. Grillon, and A. Orszag, "Third Order Autocorrelation Study of Amplified Subpicosecond Laser Pulses," *IEEE J. Quantum Electron.*, 1983, doi: 10.1109/JQE.1983.1071941.

[89]   D. A. Bender, M. P. Hasselbeck, and M. Sheik-Bahae, "Sensitive ultrashort pulse chirp measurement," *Opt. Lett.*, 2006, doi: 10.1364/ol.31.000122.

[90]   D. J. Kane and R. Trebino, "Characterization of Arbitrary Femtosecond Pulses Using Frequency-Resolved Optical Gating," *IEEE J. Quantum Electron.*, 1993, doi: 10.1109/3.199311.

[91]   M. Miranda *et al.*, "Ultrashort laser pulse characterization from dispersion scans: A comparison with SPIDER," in *2013 Conference on Lasers and Electro-Optics, CLEO 2013*, 2013, doi: 10.1364/cleo_qels.2013.jth2a.31.

[92]   C. Iaconis and I. A. Walmsley, "Spectral phase interferometry for direct electric-field reconstruction of ultrashort optical pulses," *Opt. Lett.*, 1998, doi: 10.1364/ol.23.000792.

[93]   J. A. Giordmaine and R. C. Miller, "Tunable coherent parametric oscillation in LiNbO3 at

optical frequencies," *Phys. Rev. Lett.*, 1965, doi: 10.1103/PhysRevLett.14.973.

[94]   T. Gottschall, J. Limpert, and A. Tünnermann, "Ultra-short pulse fiber optical parametric oscillator," *Opt. Lett.*, 2017, doi: 10.1364/ol.42.003423.

[95]   G. Cerullo and S. De Silvestri, "Ultrafast optical parametric amplifiers," *Rev. Sci. Instrum.*, 2003, doi: 10.1063/1.1523642.

[96]   K. R. Wilson and V. V. Yakovlev, "Ultrafast rainbow: tunable ultrashort pulses from a solid-state kilohertz system," *J. Opt. Soc. Am. B*, 1997, doi: 10.1364/josab.14.000444.

[97]   Z. Guo, Q. Hao, K. Yang, and H. Zeng, "A two-stage optical parametric amplifier for femtosecond fiber laser generation at 920 nm," *Opt. Commun.*, 2018, doi: 10.1016/j.optcom.2018.04.040.

[98]   N. Ishii *et al.*, "Multimillijoule chirped parametric amplification of few-cycle pulses," *Opt. Lett.*, 2005, doi: 10.1364/ol.30.000567.

[99]   A. Dubietis, R. Butkus, and A. P. Piskarskas, "Trends in chirped pulse optical parametric amplification," *IEEE J. Sel. Top. Quantum Electron.*, 2006, doi: 10.1109/JSTQE.2006.871962.

[100]   A. Kummrow, M. Wittmann, F. Tschirschwitz, G. Korn, and E. T. J. Nibbering, "Femtosecond ultraviolet pulses generated using noncollinear optical parametric amplification and sum frequency mixing," *Appl. Phys. B Lasers Opt.*, 2000, doi: 10.1007/s003400000483.

[101]   F. Seifert, V. Petrov, and M. Woerner, "Solid-state laser system for the generation of midinfrared femtosecond pulses tunable from 33 to 10 µm," *Opt. Lett.*, 1994, doi: 10.1364/ol.19.002009.

[102]   R. Danielius, A. Piskarskas, R. Righini, G. P. Banfi, P. Di Trapani, and I. Sa'nta, "Tunable femtosecond pulses close to the transform limit from traveling-wave parametric conversion," *Opt. Lett.*, 1993, doi: 10.1364/ol.18.001547.

[103]   A. Dubietis, G. Tamošauskas, R. Šuminas, V. Jukna, and A. Couairon, "Ultrafast supercontinuum generation in bulk condensed media," *Lith. J. Phys.*, 2017, doi: 10.3952/physics.v57i3.3541.

[104]   V. V. Yakovlev, B. Kohler, and K. R. Wilson, "Broadly tunable 30-fs pulses produced by

optical parametric amplification," *Opt. Lett.*, 1994, doi: 10.1364/ol.19.002000.

[105] L. J. Waxer, V. Bagnoud, I. A. Begishev, M. J. Guardalben, J. Puth, and J. D. Zuegel, "High-conversion-efficiency optical parametric chirped-pulse amplification system using spatiotemporally shaped pump pulses," *Opt. Lett.*, 2003, doi: 10.1364/ol.28.001245.

[106] A. Dubietis, G. Jonušauskas, and A. Piskarskas, "Powerful femtosecond pulse generation by chirped and stretched pulse parametric amplification in BBO crystal," *Opt. Commun.*, 1992, doi: 10.1016/0030-4018(92)90070-8.

[107] I. N. Ross, P. Matousek, M. Towrie, A. J. Langley, and J. L. Collier, "The prospects for ultrashort pulse duration and ultrahigh intensity using optical parametric chirped pulse amplifiers," *Opt. Commun.*, 1997, doi: 10.1016/S0030-4018(97)00399-4.

[108] A. Vaupel, N. Bodnar, B. Webb, L. Shah, and M. Richardson, "Concepts, performance review, and prospects of table-top, few-cycle optical parametric chirped-pulse amplification," *Opt. Eng.*, 2013, doi: 10.1117/1.oe.53.5.051507.

[109] J. Ma *et al.*, "Broadband, efficient, and robust quasi-parametric chirped-pulse amplification," *Opt. Express*, 2017, doi: 10.1364/oe.25.025149.

[110] J. Ma *et al.*, "Quasi-parametric amplification of chirped pulses based on a Sm^3+-doped yttrium calcium oxyborate crystal," *Optica*, 2015, doi: 10.1364/optica.2.001006.

[111] A.-C. Tien, S. Backus, H. Kapteyn, M. Murnane, and G. Mourou, "Short-Pulse Laser Damage in Transparent Materials as a Function of Pulse Duration," *Phys. Rev. Lett. - PHYS REV LETT*, vol. 82, pp. 3883–3886, May 1999, doi: 10.1103/PhysRevLett.82.3883.

[112] R. Paschotta, "Non Critical Phase Matching." https://www.rp-photonics.com/noncritical_phase_matching.html (accessed Dec. 13, 2020).

[113] B. Wu, F. Xie, and C. Chen, "Type-I and type-II noncritical phase matching of LiB3O 5 crystal," *J. Appl. Phys.*, 1993, doi: 10.1063/1.352379.

[114] A. Smith, "Crystal nonlinear optics : with SNLO examples," 1st ed., Albuquerque: AS-Photonics, 2015, pp. 255–305.

[115] F. König and F. N. C. Wong, "Extended phase matching of second-harmonic generation in periodically poled KTiOPO4 with zero group-velocity mismatch," *Appl. Phys. Lett.*, 2004, doi: 10.1063/1.1668320.

[116] B. Trophème, B. Boulanger, and G. Mennerat, "Phase-matching loci and angular acceptance of non-collinear optical parametric amplification," *Opt. Express*, 2012, doi: 10.1364/oe.20.026176.

[117] O. Isaienko and E. Borguet, "Generation of ultra-broadband pulses in the near-IR by non-collinear optical parametric amplification in potassium titanyl phosphate," *Opt. Express*, 2008, doi: 10.1364/oe.16.003949.

[118] A. Shirakawa and T. Kobayashi, "Noncollinearly phase-matched femtosecond optical parametric amplification with a 2000cm-1 bandwidth," *Appl. Phys. Lett.*, 1998, doi: 10.1063/1.120670.

[119] G. Cerullo, M. Nisoli, and S. De Silvestri, "Generation of 11 fs pulses tunable across the visible by optical parametric amplification," *Appl. Phys. Lett.*, 1997, doi: 10.1063/1.120458.

[120] T. Skauli *et al.*, "Improved dispersion relations for GaAs and applications to nonlinear optics," *J. Appl. Phys.*, 2003, doi: 10.1063/1.1621740.

[121] I. Shoji, T. Kondo, A. Kitamoto, M. Shirane, and R. Ito, "Absolute scale of second-order nonlinear-optical coefficients," *J. Opt. Soc. Am. B*, 1997, doi: 10.1364/josab.14.002268.

[122] G. Imeshev, M. A. Arbore, M. M. Fejer, A. Galvanauskas, M. Fermann, and D. Harter, "Ultrashort-pulse second-harmonic generation with longitudinally nonuniform quasi-phase-matching gratings: pulse compression and shaping," *J. Opt. Soc. Am. B*, vol. 17, no. 2, pp. 304–318, 2000, doi: 10.1364/JOSAB.17.000304.

[123] M. A. Arbore, O. Marco, and M. M. Fejer, "Pulse compression during second-harmonic generation in aperiodic quasi-phase-matching gratings," *Opt. Lett.*, 1997, doi: 10.1364/OL.22.000865.

[124] H. Sato, K. Yamamoto, and M. Kato, "Broadening of the Phase-Matching Bandwidth in Quasi-Phase-Matched Second-Harmonic Generation," *IEEE J. Quantum Electron.*, 1994, doi: 10.1109/3.299491.

[125] A. Galvanauskas, D. Harter, M. A. Arbore, M. H. Chou, and M. M. Fejer, "Chirped-pulse-amplification circuits for fiber amplifiers, based on chirped-period quasi-phase-matching gratings," *Opt. Lett.*, 1998, doi: 10.1364/ol.23.001695.

[126] C. R. Phillips, B. W. Mayer, L. Gallmann, M. M. Fejer, and U. Keller, "Design constraints of optical parametric chirped pulse amplification based on chirped quasi-phase-matching gratings," *Opt. Express*, 2014, doi: 10.1364/oe.22.009627.

[127] N. Fujioka, S. Ashihara, H. Ono, T. Shimura, and K. Kuroda, "Group-velocity-matched noncollinear second-harmonic generation in quasi-phase matching," *J. Opt. Soc. Am. B*, 2005, doi: 10.1364/josab.22.001283.

[128] M. Yamada, N. Nada, M. Saitoh, and K. Watanabe, "First-order quasi-phase matched LiNbO3 waveguide periodically poled by applying an external field for efficient blue second-harmonic generation," *Appl. Phys. Lett.*, 1993, doi: 10.1063/1.108925.

[129] R. G. Batchko, V. Y. Shur, M. M. Fejer, and R. L. Byer, "Backswitch poling in lithium niobate for high-fidelity domain patterning and efficient blue light generation," *Appl. Phys. Lett.*, 1999, doi: 10.1063/1.124787.

[130] K. Nakamura, J. Kurz, K. Parameswaran, and M. M. Fejer, "Periodic poling of magnesium-oxide-doped lithium niobate," *J. Appl. Phys.*, 2002, doi: 10.1063/1.1456965.

[131] L. A. Eyres *et al.*, "All-epitaxial fabrication of thick, orientation-patterned GaAs films for nonlinear optical frequency conversion," *Appl. Phys. Lett.*, 2001, doi: 10.1063/1.1389326.

[132] F. Raoult *et al.*, "Efficient generation of narrow-bandwidth picosecond pulses by frequency doubling of femtosecond chirped pulses," *Opt. Lett.*, vol. 23, no. 14, pp. 1117–1119, Jul. 1998, doi: 10.1364/OL.23.001117.

[133] A. Marcinkevičius, R. Tommasini, G. D. Tsakiris, K. J. Witte, E. Gaižauskas, and U. Teubner, "Frequency doubling of multi-terawatt femtosecond pulses," *Appl. Phys. B*, vol. 79, no. 5, pp. 547–554, 2004, doi: 10.1007/s00340-004-1612-5.

[134] S. Yu and A. M. Weiner, "Phase-matching temperature shifts in blue generation by frequency doubling of femtosecond pulses in KNbO3," *J. Opt. Soc. Am. B*, vol. 16, no. 8, pp. 1300–1304, Aug. 1999, doi: 10.1364/JOSAB.16.001300.

[135] A. Major, D. Sandkuijl, and V. Barzda, "Efficient frequency doubling of a femtosecond Yb:KGW laser in a BiB_3O_6 crystal," *Opt. Express*, 2009, doi: 10.1364/oe.17.012039.

[136] L. E. Nelson, S. B. Fleischer, G. Lenz, and E. P. Ippen, "Efficient frequency doubling of a femtosecond fiber laser," *Opt. Lett.*, 1996, doi: 10.1364/ol.21.001759.

[137] T. Yajima and N. Takeuchi, "Far-lnfrared Difference-Frequency Generation by Picosecond Laser Pulses," *Jpn. J. Appl. Phys.*, 1970, doi: 10.1143/JJAP.9.1361.

[138] C. Fischer and M. W. Sigrist, "Mid-IR Difference Frequency Generation," in *Solid-State Mid-Infrared Laser Sources*, 2007.

[139] I. A. Begishev *et al.*, "Highly efficient parametric amplification of optical beams. II. Parametric interaction of waves with conformal profiles," *Sov. J. Quantum Electron.*, 1990, doi: 10.1070/qe1990v020n09abeh007414.

[140] S. Witte and K. S. E. Eikema, "Ultrafast Optical Parametric Chirped-Pulse Amplification," *IEEE J. Sel. Top. Quantum Electron.*, vol. 18, no. 1, pp. 296–307, 2012, doi: 10.1109/JSTQE.2011.2118370.

[141] A. Borsutzky, R. Brünger, C. Huang, and R. Wallenstein, "Harmonic and sum-frequency generation of pulsed laser radiation in BBO, LBO, and KD*P," *Appl. Phys. B Photophysics Laser Chem.*, 1991, doi: 10.1007/BF00405687.

[142] J. C. Bienfang, C. A. Denman, B. W. Grime, P. D. Hillman, G. T. Moore, and J. M. Telle, "20W of continuous-wave sodium D_2 resonance radiation from sum-frequency generation with injection-locked lasers," *Opt. Lett.*, 2003, doi: 10.1364/ol.28.002219.

[143] M. Hacker, T. Feurer, R. Sauerbrey, T. Lucza, and G. Szabo, "Programmable femtosecond laser pulses in the ultraviolet," *J. Opt. Soc. Am. B*, 2001, doi: 10.1364/josab.18.000866.

[144] G. Arisholm, "General numerical methods for simulating second-order nonlinear interactions in birefringent media," *J. Opt. Soc. Am. B*, vol. 14, no. 10, pp. 2543–2549, Oct. 1997, doi: 10.1364/JOSAB.14.002543.

[145] L. Gordon *et al.*, "Diffusion-bonded stacked GaAs for quasiphase-matched second-harmonic generation of a carbon dioxide laser," *Electron. Lett.*, 1993, doi: 10.1049/el:19931293.

[146] L. Gallmann, G. Steinmeyer, U. Keller, G. Imeshev, M. M. Fejer, and J.-P. Meyn, "Generation of sub-6-fs blue pulses by frequency doubling with quasi-phase-matching gratings," *Opt. Lett.*, vol. 26, no. 9, pp. 614–616, 2001, doi: 10.1364/OL.26.000614.

[147] M. J. Angell *et al.*, "Growth of alternating 〈100〉/〈111〉-oriented II-VI regions for quasi-phase-matched nonlinear optical devices on GaAs substrates," *Appl. Phys. Lett.*,

1994, doi: 10.1063/1.111362.

[148] AS-Photonics, "SNLO," 2019. http://www.as-photonics.com/snlo (accessed Jun. 30, 2019).

[149] D. A. Roberts, "Simplified characterization of uniaxial and biaxial nonlinear optical crystals: a plea for standardization of nomenclature and conventions," *IEEE J. Quantum Electron.*, vol. 28, no. 10, pp. 2057–2074, 1992, doi: 10.1109/3.159516.

[150] M. V. Pack, D. J. Armstrong, and A. V. Smith, "Measurement of the χ(2) tensors of KTiOPO4, KTiOAsO4, RbTiOPO4, and RbTiOAsO4 crystals," *Appl. Opt.*, 2004, doi: 10.1364/AO.43.003319.

[151] H. Hellwig, J. Liebertz, and L. Bohatý, "Exceptional large nonlinear optical coefficients in the monoclinic bismuth borate BiB3O6 (BIBO)," *Solid State Commun.*, 1998, doi: 10.1016/S0038-1098(98)00538-9.

[152] R. Paschotta, "optical intensity," *RP Photonics Encyclopedia*. https://www.rp-photonics.com/optical_intensity.html?s=ak (accessed Apr. 01, 2020).

[153] A. Smith, "Crystal nonlinear optics : with SNLO examples," 1st ed., Albuquerque: AS-Photonics, 2015, pp. 220–221.

[154] M. Nisoli *et al.*, "Highly efficient parametric conversion of femtosecond Ti:sapphire laser pulses at 1 kHz," *Opt. Lett.*, 1994, doi: 10.1364/ol.19.001973.

[155] W. Joosen, J. P. Chambaret, A. Antonetti, P. Agostini, and G. Petite, "Broadband femtosecond infrared parametric amplification in β-BaB_2O_4," *Opt. Lett.*, 1992, doi: 10.1364/ol.17.000133.

[156] A. Zaukevičius, "The use of angular angular dispersion for formation of high peak power and ultrashort pulsed light beams in nonlinear interactions," 2012, pp. 15–16.

[157] P.-M. Dansette, R. Burokas, L. Veselis, A. Zaukevičius, A. Michailovas, and N. Rusteika, "Peculiarities of Second Harmonic Generation with Chirped Femtosecond Pulses at High Conversion Efficiency," *Opt. Commun.*, vol. 455, 2020, doi: 10.1016/j.optcom.2019.124462.

[158] G. H. Kim *et al.*, "Efficient generation of the second and third harmonics of high-power femtosecond Yb:KGW-laser radiation in nonlinear-optical BBO crystals," *J. Opt. Technol.*,

vol. 83, pp. 463–467, Aug. 2016, [Online]. Available: https://doi.org/10.1364/JOT.83.000463.

[159] P. Liu, J. Heng, and Z. Zhang, "Chirped-pulse generation from optical parametric oscillators with an aperiodic quasi-phase-matching crystal," *Opt. Lett.*, 2020, doi: 10.1364/ol.391175.

[160] R. W. Boyd, "The intensity dependent refractive index," in *Nonlinear Optics*, 3rd ed., 2008, pp. 207–252.

[161] R. Paschotta, "B integral," *RP Photonics Encyclopedia*, 2008. https://www.rp-photonics.com/b_integral.html (accessed Apr. 17, 2019).

[162] F. Shimizu, "Frequency broadening in liquids by a short light pulse," *Phys. Rev. Lett.*, 1967, doi: 10.1103/PhysRevLett.19.1097.

[163] R. H. Stolen and C. Lin, "Self-phase-modulation in silica optical fibers," *Phys. Rev. A*, 1978, doi: 10.1103/PhysRevA.17.1448.

[164] G. P. Agrawal and N. A. Olsson, "Self-Phase Modulation and Spectral Broadening of Optical Pulses in Semiconductor Laser Amplifiers," *IEEE J. Quantum Electron.*, 1989, doi: 10.1109/3.42059.

[165] P. L. Kelley, "Self-focusing of optical beams," *Phys. Rev. Lett.*, 1965, doi: 10.1103/PhysRevLett.15.1005.

[166] P. Whalen, J. V. Moloney, and M. Kolesik, "Self-focusing collapse distance in ultrashort pulses and measurement of nonlinear index," *Opt. Lett.*, 2011, doi: 10.1364/ol.36.002542.

[167] F. DeMartini, C. H. Townes, T. K. Gustafson, and P. L. Kelley, "Self-steepening of light pulses," *Phys. Rev.*, 1967, doi: 10.1103/PhysRev.164.312.

[168] J. Moses, B. A. Malomed, and F. W. Wise, "Self-steepening of ultrashort optical pulses without self-phase-modulation," *Phys. Rev. A - At. Mol. Opt. Phys.*, 2007, doi: 10.1103/PhysRevA.76.021802.

[169] L. Zhang *et al.*, "On-chip two-octave supercontinuum generation by enhancing self-steepening of optical pulses," *Opt. Express*, 2011, doi: 10.1364/oe.19.011584.

[170] B. Barviau, B. Kibler, and A. Picozzi, "Wave-turbulence approach of supercontinuum

generation: Influence of self-steepening and higher-order dispersion," *Phys. Rev. A - At. Mol. Opt. Phys.*, 2009, doi: 10.1103/PhysRevA.79.063840.

[171] J. Moses and F. W. Wise, "Soliton compression in quadratic media: high-energy few-cycle pulses with a frequency-doubling crystal," *Opt. Lett.*, 2006, doi: 10.1364/ol.31.001881.

[172] C. P. Hauri, P. Schlup, G. Arisholm, J. Biegert, and U. Keller, "Phase-preserving chirped-pulse optical parametric amplification to 173 fs directly from a Ti:sapphire oscillator," *Opt. Lett.*, 2004, doi: 10.1364/ol.29.001369.

[173] I. N. Ross *et al.*, "Generation of terawatt pulses by use of optical parametric chirped pulse amplification," *Appl. Opt.*, 2000, doi: 10.1364/ao.39.002422.

[174] R. Piessens, "Hankel transform," in *Transforms and Applications Handbook, Third Edition*, 2010.

[175] M. Guizar-Sicairos and J. C. Gutiérrez-Vega, "Computation of quasi-discrete Hankel transforms of integer order for propagating optical wave fields," *J. Opt. Soc. Am. A*, 2004, doi: 10.1364/josaa.21.000053.

[176] L. Yu, M. Huang, M. Chen, W. Chen, W. Huang, and Z. Zhu, "Quasi-discrete Hankel transform," *Opt. Lett.*, 1998, doi: 10.1364/ol.23.000409.

[177] J. C. Butcher, "Coefficients for the study of Runge-Kutta integration processes," *J. Aust. Math. Soc.*, vol. 3, no. 2, pp. 185–201, 1963, doi: 10.1017/S1446788700027932.

[178] E. W. Van Stryland, M. A. Woodall, H. Vanherzeele, and M. J. Soileau, "Energy band-gap dependence of two-photon absorption," *Opt. Lett.*, 1985, doi: 10.1364/ol.10.000490.

[179] C. Van Loan, *Computational Frameworks for the Fast Fourier Transform*. 1992.

[180] A. E. Siegman, "Defining the effective radius of curvature for a nonideal optical beam," *Quantum Electron. IEEE J.*, vol. 27, pp. 1146–1148, Jun. 1991, doi: 10.1109/3.83370.

[181] R. Paschotta, "'Hermite-Gauss modes,'" *RP Photonics Encyclopedia*. .

[182] S. Mokhov, L. Glebov, and B. Zeldovich, "Quality deterioration of self-phase modulated Gaussian beams," *Laser Phys. Lett.*, vol. 12, p. 15004, Nov. 2015, [Online]. Available: http://dx.doi.org/10.1088/1612-2011/12/1/015004.

[183] R. Trebino, R. Trebino, and E. Zeek, "Ultrashort Laser Pulses," in *Frequency-Resolved Optical Gating: The Measurement of Ultrashort Laser Pulses*, 2000.

[184] S. A. Diddams, L. Hollberg, and V. Mbele, "Molecular fingerprinting with the resolved modes of a femtosecond laser frequency comb," *Nature*, vol. 445, pp. 627 EP-, 2007, [Online]. Available: http://dx.doi.org/10.1038/nature05524.

[185] J. Chen, S. Zhuo, T. Luo, X. Jiang, and J. Zhao, "Spectral characteristics of autofluorescence and second harmonic generation from ex vivo human skin induced by femtosecond laser and visible lasers," *Scanning*, vol. 28, pp. 319–326, Feb. 2019, doi: 10.1002/sca.4950280604.

[186] R. R. Gattass and E. Mazur, "Femtosecond laser micromachining in transparent materials," *Nat. Photonics*, vol. 2, pp. 219 EP-, 2008, [Online]. Available: http://dx.doi.org/10.1038/nphoton.2008.47.

[187] B. E. Schmidt *et al.*, "Frequency domain optical parametric amplification," *Nat. Commun.*, vol. 5, pp. 3643 EP-, 2014, [Online]. Available: http://dx.doi.org/10.1038/ncomms4643.

[188] D. Träutlein, F. Adler, K. Moutzouris, A. Jeromin, A. Leitenstorfer, and E. Ferrando-May, "Highly versatile confocal microscopy system based on a tunable femtosecond Er:fiber source," *J. Biophotonics*, vol. 1, no. 1, pp. 53–61, 2008, doi: 10.1002/jbio.200710019.

[189] K. Wang, T.-M. Liu, J. Wu, N. G. Horton, C. P. Lin, and C. Xu, "Three-color femtosecond source for simultaneous excitation of three fluorescent proteins in two-photon fluorescence microscopy," *Biomed. Opt. Express*, vol. 3, no. 9, pp. 1972–1977, Sep. 2012, doi: 10.1364/BOE.3.001972.

[190] L. V Doronina-Amitonova, I. V Fedotov, A. B. Fedotov, K. V Anokhin, and A. M. Zheltikov, "Neurophotonics: optical methods to study and control the brain," *Physics-Uspekhi*, vol. 58, no. 4, p. 345, 2015, [Online]. Available: http://stacks.iop.org/1063-7869/58/i=4/a=345.

[191] E. Sidick, A. Dienes, and A. Knoesen, "Ultrashort-pulse second-harmonic generation. II. Non-transform-limited fundamental pulses," *J. Opt. Soc. Am. B*, vol. 12, pp. 1713–1722, Sep. 1995, [Online]. Available: https://doi.org/10.1364/JOSAB.12.001713.

[192] J. Zhang, J. Y. Huang, H. Wang, K. S. Wong, and G. K. Wong, "Second-harmonic generation from regeneratively amplified femtosecond laser pulses in BBO and LBO crystals," *J. Opt. Soc. Am. B*, vol. 15, pp. 200–209, Jan. 1998, [Online]. Available:

https://doi.org/10.1364/JOSAB.15.000200.

[193]   H. Teng and C. Guo, "Chirp effects in femtosecond laser-induced surface second-harmonic generation from metals," *Appl. Phys. Lett.*, vol. 85, no. 7, pp. 1110–1112, 2004, doi: 10.1063/1.1781358.

[194]   V. Thakur and N. Kant, "Resonant second harmonic generation of chirped pulse laser in plasma," *Optik (Stuttg).*, vol. 129, pp. 239–247, Jan. 2017, doi: 10.1016/j.ijleo.2016.10.068.

[195]   J. A. Au *et al.*, "16.2-W average power from a diode-pumped femtosecond Yb:YAG thin disk laser," *Opt. Lett.*, vol. 25, pp. 859–861, Jun. 2000, [Online]. Available: https://doi.org/10.1364/OL.25.000859.

[196]   K. Kato, "Temperature-tuned 90° phase-matching properties of LiB/sub 3/O/sub 5/," *IEEE J. Quantum Electron.*, vol. 30, no. 12, pp. 2950–2952, 1994, doi: 10.1109/3.362711.

[197]   H. P. Li, C. H. Kam, Y. L. Lam, and W. Ji, "Femtosecond Z-scan measurements of nonlinear refraction in nonlinear optical crystals," *Opt. Mater. (Amst).*, vol. 15, no. 4, pp. 237–242, 2001, doi: https://doi.org/10.1016/S0925-3467(00)00038-0.

[198]   R. Paschotta, "Beam Radius," *RP Photonics Encyclopedia*. 2008, Accessed: Jul. 31, 2019. [Online]. Available: https://www.rp-photonics.com/beam_radius.html.

[199]   H. Zhu, T. Wang, W. Zheng, P. Yuan, L. Qian, and D. Fan, "Efficient second harmonic generation of femtosecond laser at 1 μm," *Opt. Express*, vol. 12, pp. 2150–2155, May 2004, doi: 10.1364/OPEX.12.002150.

[200]   C. Chen *et al.*, "New nonlinear-optical crystal: LiB3O5," *J. Opt. Soc. Am. B*, vol. 6, pp. 616–621, Apr. 1989, [Online]. Available: http://josab.osa.org/abstract.cfm?URI=josab-6-4-616.

[201]   B. C. Stuart, M. Feit, S. Herman, A. Rubenchik, B. Shore, and M. Perry, "Nanosecond-to-femtosecond laser-induced breakdown in dielectrics," *Phys. Rev. B. Condens. Matter*, vol. 53, pp. 1749–1761, Feb. 1996, doi: 10.1103/PhysRevB.53.1749.

[202]   M. Ghotbi, M. Ebrahim-Zadeh, A. Majchrowski, E. Michalski, and I. V. Kityk, "High-average-power femtosecond pulse generation in the blue using BiB_3O_6," *Opt. Lett.*, vol. 29, no. 21, p. 2530, Nov. 2004, doi: 10.1364/OL.29.002530.

[203]   J. Želudevičius, R. Danilevičius, and K. Regelskis, "Optimization of pulse compression in a

fiber chirped pulse amplification system by adjusting dispersion parameters of a temperature-tuned chirped fiber Bragg grating stretcher," *J. Opt. Soc. Am. B*, vol. 32, no. 5, pp. 812–817, 2015, doi: 10.1364/JOSAB.32.000812.

[204] C. Saraceno, O. Heckl, C. R. E. Baer, T. Südmeyer, and U. Keller, "Pulse compression of a high-power thin disk laser using rod-type fiber amplifiers," *Opt. Express*, vol. 19, pp. 1395–1407, Jan. 2011, doi: 10.1364/OE.19.001395.

[205] I. Martial, D. Papadopoulos, M. Hanna, F. Druon, and P. Georges, "Nonlinear compression in a rod-type fiber for high energy ultrashort pulse generation," *Opt. Express*, vol. 17, pp. 11155–11160, Jun. 2009, doi: 10.1364/OE.17.011155.

[206] J. Capmany, D. Pastor, S. Sales, and M. A. Muriel, "Pulse distortion in optical fibers and waveguides with arbitrary chromatic dispersion," *J. Opt. Soc. Am. B*, vol. 20, pp. 2523–2533, Dec. 2003, doi: 10.1364/JOSAB.20.002523.

[207] O. E. Martinez, J. P. Gordon, and R. L. Fork, "Negative group-velocity dispersion using refraction," *J. Opt. Soc. Am. A*, 1984, doi: 10.1364/josaa.1.001003.

[208] M. A. Arbore, A. Galvanauskas, D. Harter, M. H. Chou, and M. M. Fejer, "Engineerable compression of ultrashort pulses by use of second-harmonic generation in chirped-period-poled lithium niobate," *Opt. Lett.*, 1997, doi: 10.1364/ol.22.001341.

[209] T. Suhara and H. Nishihara, "Theoretical Analysis of Waveguide Second-Harmonic Generation Phase Matched with Uniform and Chirped Gratings," *IEEE J. Quantum Electron.*, 1990, doi: 10.1109/3.59667.

[210] B. Zhang *et al.*, "Relation between temperature tuning value and grating period deviation of periodically poled crystal for SHG," in *Advanced Materials and Devices for Sensing and Imaging*, 2002, doi: 10.1117/12.471894.

[211] T. Bartulevicius, L. Veselis, K. Madeikis, A. Michailovas, and N. Rusteika, "Compact femtosecond 10 μJ pulse energy fiber laser with a CFBG stretcher and CVBG compressor," *Opt. Fiber Technol.*, 2018, doi: 10.1016/j.yofte.2018.06.006.

[212] E. L. Ginzton, "Defining, measuring, and optimizing laser beam quality," *Proc. SPIE*, 1993.

[213] D. Yelin, D. Meshulach, and Y. Silberberg, "Adaptive femtosecond pulse compression," *Opt. Lett.*, 1997, doi: 10.1364/ol.22.001793.

[214] Z. Li *et al.*, "Fourth-order dispersion compensation for ultra-high power femtosecond lasers," *Opt. Commun.*, 2015, doi: 10.1016/j.optcom.2015.08.047.

[215] K. Regelskis, J. Želudevičius, N. Gavrilin, and G. Račiukaitis, "Efficient second-harmonic generation of a broadband radiation by control of the temperature distribution along a nonlinear crystal," *Opt. Express*, 2012, doi: 10.1364/oe.20.028544.

[216] Ekspla Ltd, "Femtolux 3." https://ekspla.com/product/microjoule-class-industrial-grade-femtosecond-fiber-laser-femtolux3/ (accessed Oct. 01, 2020).

[217] H. Schroeder and S. L. Chin, "Visualization of the evolution of multiple filaments in methanol," *Opt. Commun.*, 2004, doi: 10.1016/j.optcom.2004.02.041.

[218] A. Brodeur and S. L. Chin, "Ultrafast white-light continuum generation and self-focusing in transparent condensed media," *J. Opt. Soc. Am. B*, 1999, doi: 10.1364/josab.16.000637.

[219] D. Kartashov *et al.*, "White light generation over three octaves by femtosecond filament at 39 μm in argon," *Opt. Lett.*, 2012, doi: 10.1364/ol.37.003456.

[220] A. V. Mitrofanov *et al.*, "Mid-infrared-to-mid-ultraviolet supercontinuum enhanced by third-to-fifteenth odd harmonics," *Opt. Lett.*, 2015, doi: 10.1364/ol.40.002068.

[221] V. Andresen, S. Alexander, W. M. Heupel, M. Hirschberg, R. M. Hoffman, and P. Friedl, "Infrared multiphoton microscopy: subcellular-resolved deep tissue imaging," *Current Opinion in Biotechnology*. 2009, doi: 10.1016/j.copbio.2009.02.008.

[222] S.-Y. Chen, H.-C. Yu, I.-J. Wang, and C.-K. Sun, "Infrared-based third and second harmonic generation imaging of cornea," *J. Biomed. Opt.*, 2009, doi: 10.1117/1.3183805.

[223] K. Guesmi *et al.*, "Dual-color deep-tissue three-photon microscopy with a multiband infrared laser," *Light Sci. Appl.*, 2018, doi: 10.1038/s41377-018-0012-2.

[224] A. Couairon and A. Mysyrowicz, "Femtosecond filamentation in transparent media," *Physics Reports*. 2007, doi: 10.1016/j.physrep.2006.12.005.

[225] M. Sheik-Bahae, D. J. Hagan, and E. W. Van Stryland, "Dispersion and band-gap scaling of the electronic Kerr effect in solids associated with two-photon absorption," *Phys. Rev. Lett.*, 1990, doi: 10.1103/PhysRevLett.65.96.

[226] J. M. Dudley, G. Genty, and S. Coen, "Supercontinuum generation in photonic crystal

fiber," *Rev. Mod. Phys.*, 2006, doi: 10.1103/RevModPhys.78.1135.

[227] H. Li, L. Wei, X. Zhang, and Y. Song, "Supercontinuum generation in tapered fibers," in *2009 Asia Communications and Photonics Conference and Exhibition, ACP 2009*, 2009, doi: 10.1364/ol.25.001415.

[228] A. V. Husakou and J. Herrmann, "Supercontinuum generation of higher-order solitons by fission in photonic crystal fibers," *Phys. Rev. Lett.*, 2001, doi: 10.1103/PhysRevLett.87.203901.

[229] J. M. Dudley and S. Coen, "Coherence properties of supercontinuum spectra generated in tapered and photonic crystal fibers," in *Pacific Rim Conference on Lasers and Electro-Optics, CLEO - Technical Digest*, 2002, doi: 10.1109/cleo.2002.1033414.

[230] C. Agger *et al.*, "Supercontinuum generation in ZBLAN fibers—detailed comparison between measurement and simulation," *J. Opt. Soc. Am. B*, 2012, doi: 10.1364/josab.29.000635.

[231] J. M. Dudley and S. Coen, "Numerical simulations and coherence properties of supercontinuum generation in photonic crystal and tapered optical fibers," *IEEE J. Sel. Top. Quantum Electron.*, 2002, doi: 10.1109/JSTQE.2002.1016369.

[232] D. E. Zelmon, D. L. Small, and R. Page, "Refractive-index measurements of undoped yttrium aluminum garnet from 04 to 50 μm," *Appl. Opt.*, 1998, doi: 10.1364/ao.37.004933.

[233] "Handbook of optical materials," *Choice Rev. Online*, 2003, doi: 10.5860/choice.40-4668.

[234] Y. Xu and W. Y. Ching, "Electronic structure of yttrium aluminum garnet (formula presented)," *Phys. Rev. B - Condens. Matter Mater. Phys.*, 1999, doi: 10.1103/PhysRevB.59.10530.

[235] T. S. Lomheim and L. G. DeShazer, "Optical-absorption intensities of trivalent neodymium in the uniaxial crystal yttrium orthovanadate," *J. Appl. Phys.*, 1978, doi: 10.1063/1.324471.

[236] A. G. Selivanov, I. A. Denisov, N. V. Kuleshov, and K. V. Yumashev, "Nonlinear refractive properties of Yb3+-doped KY(WO 4)2 and YVO4 laser crystals," *Appl. Phys. B Lasers Opt.*, 2006, doi: 10.1007/s00340-005-2098-5.

[237] M. R. Dolgos, A. M. Paraskos, M. W. Stoltzfus, S. C. Yarnell, and P. M. Woodward, "The electronic structures of vanadate salts: Cation substitution as a tool for band gap manipulation," *J. Solid State Chem.*, 2009, doi: 10.1016/j.jssc.2009.04.032.

[238] Y. Nigara, "Measurement of the Optical Constants of Yttrium Oxide," *Jpn. J. Appl. Phys.*, 1968, doi: 10.1143/jjap.7.404.

[239] Y. Senatsky *et al.*, "Nonlinear refractive index of ceramic laser media and perspectives of their usage in a high-power laser-driver," *Laser Phys. Lett.*, 2004, doi: 10.1002/lapl.200410108.

[240] V. H. Mudavakkat, V. V. Atuchin, V. N. Kruchinin, A. Kayani, and C. V. Ramana, "Structure, morphology and optical properties of nanocrystalline yttrium oxide (Y2O3) thin films," *Opt. Mater. (Amst).*, 2012, doi: 10.1016/j.optmat.2011.11.027.

[241] M. C. Pujol *et al.*, "Crystalline structure and optical spectroscopy of Er3+-doped KGd(WO4)2 single crystals," *Appl. Phys. B Lasers Opt.*, 1999, doi: 10.1007/s003400050605.

[242] R. Paschotta, "article on 'photodiodes' in the RP Photonics encyclopedia." .

[243] P. Mackonis, A. Petrulenas, V. Girdauskas, and A. M. Rodin, "Stable 1100-2400 nm supercontinuum in YAG with picosecond pumping for simplified OPCPA," in *2019 Conference on Lasers and Electro-Optics Europe and European Quantum Electronics Conference, CLEO/Europe-EQEC 2019*, 2019, doi: 10.1109/CLEOE-EQEC.2019.8872623.

[244] R. Riedel *et al.*, "Power scaling of supercontinuum seeded megahertz-repetition rate optical parametric chirped pulse amplifiers," *Opt. Lett.*, 2014, doi: 10.1364/ol.39.001422.

[245] D. Zhang, Y. Kong, and J. Y. Zhang, "Optical parametric properties of 532-nm-pumped beta-barium-borate near the infrared absorption edge," *Opt. Commun.*, 2000, doi: 10.1016/S0030-4018(00)00968-8.

[246] N. Umemura, K. Miyata, and K. Kato, "New data on the optical properties of BiB3O6," *Opt. Mater. (Amst).*, 2007, doi: 10.1016/j.optmat.2006.12.014.

[247] S. Miller, F. Noack, V. Panyutin, V. Petrov, F. Rotermund, and G. Xu, "Nonlinear refractive index of BiB3O6," in *Optics InfoBase Conference Papers*, 2008.

[248] I. A. Begishev *et al.*, "Highly efficient parametric amplification of optical beams. I.

Optimization of the profiles of interacting waves in parametric amplification," *Sov. J. Quantum Electron.*, 1990, doi: 10.1070/qe1990v020n09abeh007413.

[249] E. B. Treacy, "Optical Pulse Compression with Diffraction Gratings," *IEEE J. Quantum Electron.*, 1969, doi: 10.1109/JQE.1969.1076303.

[250] A. Zeytunyan, G. Yesayan, and L. Mouradian, "Pulse compression to 14 fs by third-order dispersion control in a hybrid grating-prism compressor," *Appl. Opt.*, 2013, doi: 10.1364/AO.52.007755.

[251] Optics toolbox, "Two prism compressor." http://toolbox.lightcon.com/tools/prismpair/ (accessed Nov. 01, 2020).

[252] Teledyne Princeton Instruments, "PI MAX4." https://www.princetoninstruments.com/products/pi-max-family/pi-max (accessed Dec. 05, 2020).

[253] H. Lim and J. Danias, "Effect of axonal micro-tubules on the morphology of retinal nerve fibers studied by second-harmonic generation," *J. Biomed. Opt.*, 2012, doi: 10.1117/1.jbo.17.11.110502.

[254] P. J. Campagnola, A. C. Millard, M. Terasaki, P. E. Hoppe, C. J. Malone, and W. A. Mohler, "Three-dimensional high-resolution second-harmonic generation imaging of endogenous structural proteins in biological tissues," *Biophys. J.*, 2002, doi: 10.1016/S0006-3495(02)75414-3.

[255] C. J. Murphy *et al.*, "Biological responses to engineered nanomaterials: Needs for the next decade," *ACS Cent. Sci.*, 2015, doi: 10.1021/acscentsci.5b00182.

[256] F. Timpu, A. Sergeyev, N. R. Hendricks, and R. Grange, "Second-harmonic enhancement with mie resonances in perovskite nanoparticles," *ACS Photonics*, 2017, doi: 10.1021/acsphotonics.6b00570.

[257] O. B. Tarun, M. Y. Eremchev, A. Radenovic, and S. Roke, "Spatiotemporal Imaging of Water in Operating Voltage-Gated Ion Channels Reveals the Slow Motion of Interfacial Ions," *Nano Lett.*, 2019, doi: 10.1021/acs.nanolett.9b02024.

[258] L. A. Bagatolli and E. Gratton, "Two photon fluorescence microscopy of coexisting lipid domains in giant unilamellar vesicles of binary phospholipid mixtures," *Biophys. J.*, 2000,

doi: 10.1016/S0006-3495(00)76592-1.

[259] L. A. Bagatolli, T. Parasassi, and E. Gratton, "Giant phospholipid vesicles: Comparison among the whole lipid sample characteristics using different preparation methods - A two photon fluorescence microscopy study," *Chem. Phys. Lipids*, 2000, doi: 10.1016/S0009-3084(00)00118-3.

[260] M. Fidorra, A. Garcia, J. H. Ipsen, S. Härtel, and L. A. Bagatolli, "Lipid domains in giant unilamellar vesicles and their correspondence with equilibrium thermodynamic phases: A quantitative fluorescence microscopy imaging approach," *Biochim. Biophys. Acta - Biomembr.*, 2009, doi: 10.1016/j.bbamem.2009.08.006.

[261] T. Pons, L. Moreaux, O. Mongin, M. Blanchard-Desce, and J. Mertz, "Mechanisms of membrane potential sensing with second-harmonic generation microscopy," *J. Biomed. Opt.*, 2003, doi: 10.1117/1.1581871.

[262] H. Stein, S. Spindler, N. Bonakdar, C. Wang, and V. Sandoghdar, "Production of isolated giant unilamellar vesicles under high salt concentrations," *Front. Physiol.*, 2017, doi: 10.3389/fphys.2017.00063.

[263] ThermoFisher, "Nile Red." https://www.thermofisher.com/order/catalog/product/N1142#/N1142 (accessed Dec. 08, 2020).

[264] M. E. Durst, G. Zhu, and C. Xu, "Simultaneous spatial and temporal focusing for axial scanning," *Opt. Express*, 2006, doi: 10.1364/oe.14.012243.

[265] P. Xi, Y. Andegeko, D. Pestov, V. V. Lovozoy, and M. Dantus, "Two-photon imaging using adaptive phase compensated ultrashort laser pulses," *J. Biomed. Opt.*, 2009, doi: 10.1117/1.3059629.

[266] S. Tang, T. B. Krasieva, Z. Chen, and B. J. Tromberg, "Combined multiphoton microscopy and optical coherence tomography using a 12-fs broadband source," *J. Biomed. Opt.*, 2006, doi: 10.1117/1.2193428.

[267] V. Roudnev and B. D. Esry, "General theory of carrier-envelope phase effects," *Phys. Rev. Lett.*, 2007, doi: 10.1103/PhysRevLett.99.220406.

[268] A. Baltuška, T. Fuji, and T. Kobayashi, "Controlling the Carrier-Envelope Phase of

Ultrashort Light Pulses with Optical Parametric Amplifiers," *Phys. Rev. Lett.*, 2002, doi: 10.1103/PhysRevLett.88.133901.

[269] D. C. Sordillo, L. A. Sordillo, P. P. Sordillo, L. Shi, and R. R. Alfano, "Short wavelength infrared optical windows for evaluation of benign and malignant tissues," *J. Biomed. Opt.*, 2017, doi: 10.1117/1.jbo.22.4.045002.